Taking Steps Towards Superfluid-like Spin Transport in Metallic Ferromagnets

David Acoya Smith

Dissertation submitted to the Faculty of the
Virginia Polytechnic Institute and State University
in partial fulfillment of the requirements for the degree of

Doctor of Philosophy
in
Physics

Satoru Emori, Chair
Jean J. Heremans
Edwin F. Barnes
Vinh Nguyen

April 25, 2022
Blacksburg, Virginia

Keywords: spintronics, spin superfluidity, ferromagnets, damping
Copyright 2022, David Acoya Smith

Taking Steps Towards Superfluid-like Spin Transport in Metallic Ferromagnets

David Acoya Smith

(ABSTRACT)

Conventional electronics rely on the transport of electrons through a circuit to carry information. This comes with ever-present Joule heating as a result of the resistive scattering of electrons. Recent works in the field of spintronics have focused on using magnetic excitations (e.g., spin waves) instead of electrons as a means of information transport without Joule heating. However, realizing long distance information transport using conventional spin waves has proven difficult owing to their diffusive nature and the exponential decay of spin current. Theoretical studies have proposed a new form of magnetization dynamics, referred to as superfluid-like spin transport, as a way to overcome this shortfall. Instead of decaying exponentially with distance, the spin current associated with superfluid-like spin transport decays linearly with distance, potentially allowing for information transport beyond the micron-scale. In this dissertation, I discuss the work that I have done towards realizing this novel phenomenon in a metallic, ferromagnetic system. Results on a reduced damping and reduced magnetic moment Fe-based alloy, micromagnetic simulations that use established domain wall physics to explain superfluid-like spin transport, and an investigation of spin torques found in a current-in-plane spin valve structure with broken in-plane symmetry for excitation of superfluid-like spin transport dynamics are discussed. I conclude by discussing what steps remain before superfluid-like spin transport can be measured in an experimental system as well as the impacts this work could have on the wider spintronics field.
This work was supported in part by National Science Foundation, Grant No. DMR-2003914.

Taking Steps Towards Superfluid-like Spin Transport in Metallic Ferromagnets

David Acoya Smith

(GENERAL AUDIENCE ABSTRACT)

All of the electronics devices we use every day depend on tiny, charged particles called electrons moving through a wire. These particles bounce off of and collide with defects within that wire and cause the wire to heat up, dissipating their energy to the surrounding environment. If this could be avoided, the overall power needed to operate our devices could be lowered. To alleviate this problem, scientists take advantage of another property of the electron, its spin (which gives rise to magnetism), to send signals. Since the electron spin can interact with the spin of nearby electrons, information can be transported this way without actually moving the electrons themselves. These magnetic signals can be thought of as the electron spin wiggling a small amount about its axis, somewhat akin to a precessing top. The downside to these magnetic signals is that they decay away very quickly, typically much quicker than electron currents. In this dissertation, I focus on using a different form of magnetic signals, one that can be thought of like a fluid flowing through a pipe, to send information much further than before without significant energy losses. This phenomenon, which I call "superfluid-like spin transport," has the potential to dramatically alter the future development path of next-generation devices. In the first experiment, I discuss the work done to choose a suitable material platform that can host superfluid-like spin transport. Starting with the common magnet iron, we show that by mixing it with the correct non-magnetic material, it is possible to improve the magnetic properties in a way that is beneficial to superfluid-like spin transport. In the next experiment, computer simulations were used to understand how superfluid-like spin transport might behave in a future device. We find that the fluid-like behavior found in this phenomenon can actually be understood by imagining a train of rigid particle-like entities being packed closely together. In the final experiment, I investigate whether a new and potentially simpler device geometry can be used to start the flow of superfluid-like spin transport. It turns out that the mechanism needed to start the flow is surprisingly weak in the material system studied. While this work does not achieve superfluid-like spin transport, it has taken essential steps towards understanding how one might do so in the future using common materials in an easy-to-make manner. I conclude by offering my thoughts of what the next steps would be as well as impacts this work might have on future next-generation energy-efficient devices.

Acknowledgments

The journey towards completing my PhD has been a long and difficult one. One that would not have been possible without the help from so many people along the way.

First, I have to thank my adviser, Prof. Satoru Emori, for everything he has done. Satoru and I started at Virginia Tech in the same semester (albeit at completely different points in our careers!). I recall speaking to him for the first time and the enthusiasm and ideas he had to get his lab started, alongside the various opportunities that would be there for equally excited graduate students. On multiple occasions, Satoru has gone above and beyond what would be expected for an adviser. In particular, I remember the months after my first qualifying exam attempt that stick out the most where Satoru and I would meet once or twice a week to practice physics problems and presentation skills. I have learned so much from Satoru, not only how to become a better researcher but a better person as well. I hope that, going forward, I can still rely on Satoru for his wisdom, his insight, and advice on how best to approach the many obstacles we face in life.

I would like to thank my committee members, Prof. Vinh Nguyen, Prof. Ed Barnes, and Prof. Jean Heremans, for their feedback and input throughout my various presentations and during my whole graduate career. In particular, I am thankful to have had the opportunity to collaborator with Prof. Heremans on photolithography projects and work with him as a teaching assistant. The valuable insight into instrumentation uses, approaches to experiment design and troubleshooting, and the great stories have been a thoroughly enjoyable time.

I am extremely grateful to have had the opportunity to work with many different lab mates and collaborators over the years. Dr. Behrouz Khodadadi, Dr. Shuang Wu, Youngmin Lim, and Rachel Maizel in particular I would like to thank for their help, their insight, and their feedback on various ideas during our lab work. I would also like to thank all of the collaborators I have worked with these last five years, from other universities to private companies, to shared user facilities both here at Virginia Tech and beyond.

Getting through a PhD would not have been possible without the great friends I've made in Blacksburg. From the very beginning, working in the shared office space during my first year of coursework, to the weekly escapades to downtown Blacksburg and beyond, my friends have always been there to provide support or as a means for distraction from work. I hope that the end of our graduate careers does not mean the end of our friendships, and I hope to see many of them in the years to come.

Finally, the person I have to thank the most is my loving wife, Tonya. She has been there

through the good and the bad, the great and ugly. While we may have both been completing our graduate degrees, gone through a global pandemic, and some tough life events, never has her support for me dwindled. She has been my biggest supporter through all of my graduate career and getting to the end would not have been possible without her. I am looking forward to spending the rest of our lives together as we continue to support and love each other for the rest of our lives.

Contents

List of Figures ix

List of Tables xv

1 Introduction 1

1.1 Information Transport in Spintronics . . . 2
1.2 Magnetization Dynamics . . . 3
1.3 Spin Torques . . . 5
1.4 Diffusive Spin Waves . . . 6
1.5 Spin Superfluidity . . . 8
1.5.1 Superfluid-*like* Spin Transport . . . 10
1.5.2 Practical Considerations . . . 11
1.6 Dissertation Outline . . . 12

2 Experimental Methods 14

2.1 Magnetron Sputtering . . . 15
2.2 Ferromagnetic Resonance . . . 17
2.2.1 Broadband Ferromagnetic Resonance . . . 17
2.2.2 Spin Torque Ferromagnetic Resonance . . . 20
2.3 Vibrating Sample Magnetometry . . . 22
2.4 Electrical Transport . . . 24
2.5 X-Ray Techniques . . . 26
2.5.1 X-Ray Diffraction . . . 26
2.5.2 X-Ray Reflectivity . . . 27
2.6 Ion Milling . . . 29
2.7 Photolithography . . . 30

3 Developing a Low Damping Metallic Ferromagnet **32**

3.1 Introduction . . . 33

3.2 Film Deposition . . . 35

3.3 Structural Properties . . . 35

3.4 Magnetic Relaxation . . . 35

3.4.1 In-Plane Ferromagnetic Resonance . . . 35

3.4.2 Out-of-Plane Ferromagnetic Resonance . . . 39

3.4.3 Magnetic Relaxation: Practical Considerations . . . 42

3.5 Spectroscopic Parameters . . . 42

3.6 Discussion . . . 45

3.7 Summary . . . 46

4 Superfluid-like Spin Transport as a Train of Domain Walls **49**

4.1 Introduction . . . 50

4.2 Simulation Details . . . 52

4.3 Experimental Determination of Material Parameters . . . 54

4.4 Easy-plane Precession Dynamics in Single Layer Systems . . . 55

4.5 Results and Discussion . . . 56

4.5.1 Excitation of Diffusive Spin Waves . . . 56

4.5.2 Diffusive Motion of an Isolated Domain Wall . . . 57

4.5.3 Weakly Interacting Domain Wall Train . . . 59

4.5.4 Moderately Interacting Domain Wall Train . . . 61

4.5.5 Strongly Interacting Domain Wall Train . . . 61

4.5.6 Consequences for Practical Applications . . . 64

4.6 Conclusion . . . 66

5 Unconventional Spin Torques in Exchange-Biased Spin Valves **67**

5.1 Introduction . . . 68

5.2 Experimental Methods . . . 69

5.3 Results . . . 71
5.3.1 Static Magnetic Properties . . . 71
5.3.2 Electrical Resistance Measurements . . . 72
5.3.3 Angular Dependence of ST-FMR Signal . . . 73
5.3.4 DC Bias Dependence of ST-FMR Signal . . . 76
5.4 Discussion . . . 79
5.5 Conclusion . . . 80

6 Conclusions and Future Outlook **82**
6.1 Closing Remarks . . . 83
6.2 Future Work . . . 84

7 Additional Publications **88**

Bibliography **93**

Appendices **105**

Appendix A Micromagnetics Using Mumax **106**
A.1 Running Simulations Using Mumax3 . . . 107
A.2 Simulating Superfluid-like Spin Transport . . . 107
A.3 Data Analysis . . . 110

List of Figures

1.1 (a) Depiction of a conventional charge current and the resistive scattering of electrons that results in Joule heating. (b) The transfer of spin angular momentum using spin waves as a means to avoid Joule heating losses. 2

1.2 Visualization of the torques involved in the LLG equation that governs how a magnetic moment behaves in an effective field. The precessional and damping torques are labelled. 4

1.3 Temperature dependence of the intrinsic Gilbert damping parameter for (a) Fe deposited on a $MgAl_2O_4$ (MAO) substrate and (b) Fe deposited on a MgO substrate. Figure is taken from Ref. [1]. These two systems have different degrees of crystallinity and were used as a case to distinguish the role film microstructure plays in Gilbert damping. The two dashed lines show the conductivity-like (σ) and resistivity-like (ρ) contributions to the total intrinsic damping (solid line). 5

1.4 (a) Side and top view of a spin wave. Note how the phase of the precession changes from one local magnetic moment to the next, leading to a wave pattern after enough local moments. (b) Visualization of diffusive spin waves dynamics in a magnetically ordered material where the dynamics propagate down the length of the strip. (c) The associated exponential decay of spin current. 7

1.5 Visualization of the two terms found in Eq. 1.2: (a) the exchange interaction, which favors a parallel configuration of spins, and (b) easy-plane anisotropy, which prefers the magnetization to lie within the xy plane of the film. (c) The definition of the variables used to parameterize the magnetization. . . . 9

1.6 (a) Spin superfluid dynamics where the magnetization vector precesses within the plane of the film. The out-of-plane component of the magnetization m_z is constant with position and the magnetization makes an angle ϕ with the $\hat{x}$ axis. The spin flow is defined to be along the direction of the phase gradient. (b) Once Gilbert damping is considered, the spin current exhibits a linear decay with distance. 10

1.7 Detected spin current J_s as a function of driving voltage V_{in}. In the absence of in-plane anisotropy, the detected spin current will have a linear relation with driving voltage and no threshold, as shown by the dashed line. In-plane anisotropies and Gilbert damping introduce a threshold energy V_{th} that must be overcome to excite dynamics (solid line). 11

2.1 Picture of the AJA dual chamber sputtering system. The two chambers are nearly identical, with the exception of the right-hand-side chamber containing a DC ion source for ion milling. 16

2.2 Detailed schematic of the various instruments used in broadband ferromagnetic resonance (BB-FMR) setup. 18

2.3 BB-FMR setup with various components labelled. 19

2.4 The ST-FMR setup used in the lab with various important components labelled. The Kepco power supplies are located below the optical table and are not shown. 21

2.5 Detailed schematic example of the ST-FMR setup. The bias tee is located in the center and connects the sourcemeters, lock-in amplifier, and RF source to the sample via a ground-signal-ground probe. 22

2.6 Microsense EZ-9 VSM system used for measuring hysteresis loops. The electromagnet and vibrator assembly is shown on the left and the instrument tower with computer monitor is shown on the right. 23

2.7 Example of a hysteresis loop obtained using the Microsense EZ-9 VSM for 20 nm of Fe at room temperature. 24

2.8 DC probe station with the Helmholtz coils used for measuring giant magnetoresistance. The smaller white coils are used for measuring the planar Hall effect. 25

2.9 (a) XRD geometry showing how the angles ω and θ are defined. (b) Example symmetric $2\theta - \omega$ scan for 25 nm of $Fe_{90}V_{10}$ deposited on a $MgAl_2O_4$ (MAO) substrate. (c) Example rocking curve (ω) scans centered about the peak maximum ω_c for the film peak and substrate peaks. 27

2.10 (a) Raw XRR signal captured for a single layer film of W deposited on a Si/SiO_2 substrate. (b) Peak position squared (square markers) as a function of peak number squared. The solid line is a fit according to Eq. (2.10) from which the film thickness can be estimated. (c) XRR spectra fit according to a model using the GenX open-source package with extracted film thickness and interfacial roughness. 28

2.11 Visualization of each step involved in the photolithography process. 31

3.1 2θ-ω X-ray diffraction scans showing (002) and (004) substrate and (002) film peaks for (a) bcc Fe, (b) $Fe_{80}V_{20}$, and (c) $Fe_{80}Al_{20}$. 36

3.2 FMR spectra at $f = 20$ GHz with the magnetic field H applied in the film plane, fitted using a Lorentzian derivative (solid curve) for Fe, $Fe_{80}V_{20}$, and $Fe_{80}Al_{20}$. 37

3.3 FMR linewidths versus microwave frequency for the magnetic field applied within the plane of the film for three distinct alloys. The solid lines are linear fits, described by Eq. (3.1), from which the effective damping parameter and zero frequency linewidth are determined. The dashed line represents the result for $Fe_{73}V_{27}$ from Scheck *et al.* [2] 38

3.4 The effective damping parameter α_{eff}^{IP} for (a) $Fe_{100-x}V_x$ and (b) $Fe_{100-x}Al_x$ and zero frequency linewidth $\mu_0\Delta H_0^{IP}$ for (c) $Fe_{100-x}V_x$ and (d) $Fe_{100-x}Al_x$, obtained from in-plane FMR. The solid symbols in (a) and (c) represent results reported by Scheck *et al.* [2] 39

3.5 FMR linewidths versus applied microwave frequency for the magnetic field applied perpendicular to the plane of the film for three distinct alloys. The line is a linear fit, described by Eq. (3.5), from which the intrinsic Gilbert damping parameter and zero frequency linewidth are determined. 40

3.6 The intrinsic Gilbert damping parameter α_{int} for (a) $Fe_{100-x}V_x$ and (b) $Fe_{100-x}Al_x$ and zero frequency linewidth $\mu_0\Delta H_0^{OP}$ for (c) $Fe_{100-x}V_x$ and (d) $Fe_{100-x}Al_x$ obtained from out-of-plane FMR. In (a), the dashed curve shows the predicted intrinsic damping parameter computed by Mankovsky *et al.* [3] 41

3.7 FMR resonance field vs frequency for $Fe_{75}V_{25}$ with the magnetic field applied along the film [100] (red circles) and [110] (blue squares) axes. The solid lines are fits according to Eq. (3.7). 43

3.8 (a) Effective magnetization, (b) magnitude of in-plane cubic anisotropy field, and (c) g-factor versus V and Al concentration. The solid (open) markers represent data from in-plane (out-of-plane) measurements. 44

3.9 The six unique atomic configurations from the supercell program for mimicking the $Fe_{81.25}V_{18.75}$ or $Fe_{81.25}Al_{18.75}$ solid solution. 46

3.10 Calculated spin-up (positive) and spin-down (negative) density of states for (a) Fe, (b) $Fe_{81.25}V_{18.75}$, and (c) $Fe_{81.25}Al_{18.75}$. Results from the 6 distinct atomic configurations are show in (b,c); the average density of states at E_F for $Fe_{81.25}V_{18.75}$ and $Fe_{81.25}Al_{18.75}$ are shown in Table 1. 47

4.1 (a) Illustration of small angle precession constituting diffusive spin waves and exponential decay of spin flow. (b) Easy-plane precession constituting superfluid-like spin transport and associated linear decay of spin flow. 51

4.2 (a) Micromagnetic simulation setup of the synthetic antiferromagnet nanostrip. (b) The resulting torque generated by the out-of-plane spin-polarized electric current J_c, lifting the magnetization out of the plane in the injector region. (c) The out-of-plane component of the magnetization creates a demagnetizing field, generating a precessional torque that drives easy-plane precession. 53

4.3 FMR resonance field as a function of microwave frequency. The solid line is a fit according to Eq. 4.1. 55

4.4 FMR linewidth as a function of microwave frequency. The solid line is a fit according to Eq. 4.2. 56

4.5 Micromagnetic snapshots of vortex formation in single layer (a) perfect and (b) notched nanostrips. 56

4.6 In-plane deviation of the magnetization from the $\hat{x}$-axis as a function of x position, related to the spin current carried by diffusive spin waves. The red line is an exponential decay fit from which the characteristic length scale is extracted. 57

4.7 Micromagnetic snapshots of an isolated DW, taken every 0.5 ns from the start of the simulation in the (a) perfect and (b) notched nanostrips. The associated DW velocity as a function of simulation time is shown for the (c) perfect and (d) notched nanostrips. The inset in (c) shows the DW velocity on a logarithmic scale. 58

4.8 Micromagnetic snapshots of a weakly interacting DW train in the (a) perfect nanostrip and (b) notched nanostrip. In the notched nanostrip, note the momentary pinning of the first DW and the subsequent pinning of the DW train. The average DW velocity as a function of simulation time for the (c) perfect nanostrip and (d) the second DW in the train in the notched nanostrip. The inset in (c) shows the average DW velocity on a logarithmic scale. . . . 60

4.9 Micromagnetic snapshots of a weakly interacting DW train in the (a) perfect nanostrip and (b) notched nanostrip with the DW interactions are strong enough to overcome the pinning potential. The associated average DW velocity is shown for the (c) perfect and (d) notched nanostrips. 62

4.10 (a), (b) Micromagnetic snapshots of the densely packed DW train that resembles superfluid-like spin transport. (c), (d) The average DW velocity as a function of simulation time for the (c) perfect and (d) notched nanostrips. (e), (f) Time-averaged superfluid velocity and equivalent DW velocity, computed via Eq. (4.4), as a function of DW position for the (e) perfect and (f) notched nanostrips. 63

4.11 (a) Time-averaged superfluid velocity at $x = 1500$ nm as a function of driving current density J_c for the perfect (black squares) and notched (red circles) nanostrips. The error bars indicate the standard deviation. (b) Precessional frequency of the magnetization. (c) Equivalent DW velocity computed using Eq. 4.4 at $x = 1500$ nm 65

5.1 (a) Easy-axis precession of the magnetization as a result of the spin Hall effect. (b) Easy-plane precession that could arise from out-of-plane spin polarization. 69

5.2 (a) Stack structure showing the IrMn/CoFe/Cu/NiFe portion with thickness and relative direction of the antiferromagnetic ordering in IrMn and magnetization in CoFe and NiFe. (b) Orientation of the magnetization fixed layer in CoFe with respect to the NiFe magnetization. The angle between these two magnetization vectors is defined as ϕ. We assume that the NiFe magnetization is perfectly aligned with the external magnetic field when the applied field is greater than the NiFe coercivity and the CoFe layer does not deviated from the exchange bias direction. 70

5.3 Hysteresis loop showing the strength of the exchange bias and individual switching of the two magnetic layers. The magnitude of the exchange bias field is determined by estimating the center of the shifted minor loop. The applied field is parallel with the magnetic exchange bias direction. 71

5.4 (a) Sample resistance as a function of external field for various field angles. (b) DC resistance, extracted from (a) at ~ 20 mT, as a function of applied magnetic field angle. The black line is a fit according to Eq. 5.2 and the red (blue) line shows the GMR (AMR) contribution to the total resistance. . . . 73

5.5 ST-FMR signal fit according to Eq. 2.5 and decomposed into the symmetric V_{sym} and antisymmetric V_{asym} Lorentzians. 74

5.6 Antisymmetric amplitude V_{asym} as a function of applied field angle ϕ. The solid line is a fit to Eq. 5.7. In (a) τ_z is a free parameter and R_{AMR} is fixed to the value determined from Fig. 5.4. In (b) τ_z is fixed to zero and R_{AMR} is fixed to the same value as in (a). In (c) both τ_z and R_{AMR} are allowed to be free parameters. In (d) R_{AMR} is a free parameter and τ_z is fixed to zero. The quality of the fit significantly increases from (a) to (c) and marginally changes between (c) and (d). 75

5.7 (a) FMR resonance field and (b) FMR linewidth as functions of DC bias current at $\phi = -100°$. The solid line is a linear fit from which the slope is extracted for each plot. 77

5.8 (a) Angular dependence of the FMR resonance field modulation efficiency. The solid line is a sinusoidal fit. (b) Modulation efficiency of the FMR linewidth as a function of field angle. The scatter in data points in both (a) and (b) at small field angles is likely a result of the signal amplitude being very small and difficulties in accurately fitting the data. 78

5.9 Visualization of reduced interfacial spin-orbit field not rotating the spins enough out-of-plane to have a noticeable effect on the precessing NiFe magnetization. 80

6.1 (a) Nanostrip with grains of average size 10 nm. The magnetization is uniform within each grain but randomly oriented. (b) Same as (a) but squares of various sizes have been removed from the edges at multiple points to simulate edge roughness. (c) Same as (b) with thermal fluctuations to simulate an equivalent temperature of $T = 300$ K and an externally applied magnetic field of $\mu_0 H_{ext} = 10$ mT along the $\hat{x}$ direction. The snapshot is taken after $t = 1$ ns of simulation time. 85

6.2 Two potential device geometries that could be used for a future experiment to measure superfluid-like spin transport. (a) Current-perpendicular-to-plane geometry with nanopillars. The excitation nanopillar contains a perpendicularly magnetized reference layer used to spin polarize the charge current. (b) Current-in-plane geometry where the excitation line could contain an in-plane magnetized layer that would generate out-of-plane spin polarized spin currents when an in-plane charge current is applied. 86

A.1 Visualization of how the data is organized within an OMF file for a $4 \times 4 \times 2$ sample. Each numbered cell will correspond to a row within the OMF file. . 112

List of Tables

3.1 Number of spin-up and spin-down states at E_F. For $Fe_{81.25}V_{18.75}$ and $Fe_{81.25}Al_{18.75}$, the average and standard deviation of values for the 6 distinct atomic configurations (cf. Fig. 3.9) are shown. 48

5.1 Summary of fit parameters from Eq. 5.7 for the angular dependence of the antisymmetric component V_{asym} for the various scenarios presented in Fig. 5.6. Numbers without uncertainties represent fixed values. 76

Chapter 1

Introduction

1.1 Information Transport in Spintronics

Electronic devices play an essential role in our everyday lives. Whenever one of these devices is used, electrons move throughout a metallic circuit. The moving electrons collide with defects, edges, and phonons, changing their path and dissipating energy (see Fig. 1.1a). This dissipation of energy results in Joule heating in the conductor. While this is great for creating devices such as heating elements, it results in large amounts of energy losses when powering microelectronic devices, reducing their energy efficiency.

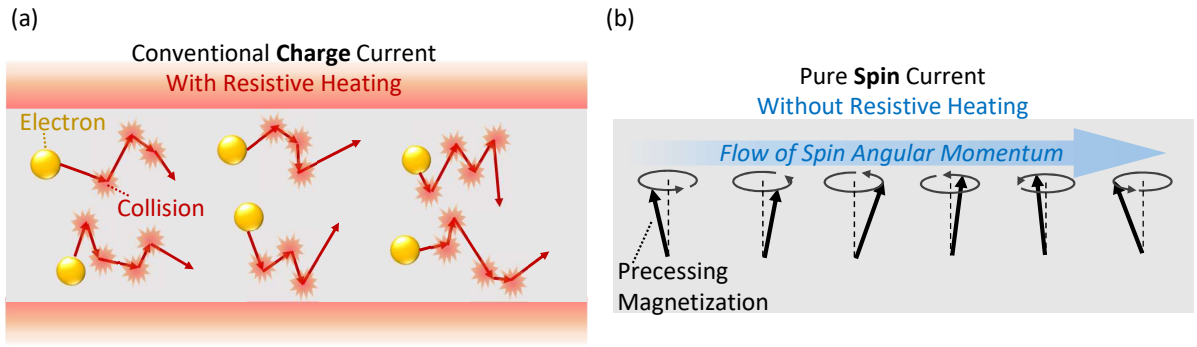


Figure 1.1: (a) Depiction of a conventional charge current and the resistive scattering of electrons that results in Joule heating. (b) The transfer of spin angular momentum using spin waves as a means to avoid Joule heating losses.

With the global energy consumption increasing year after year [4, 5], problems to address the energy inefficiency of electronic devices have gained popularity in recent years. One of the potential solutions to create more energy efficient devices comes from the field of spintronics [6, 7, 8, 9, 10]. Spintronics aims to use another inherent property of the electron, its spin, as a means of encoding and transporting information. Since electron spin gives rise to magnetism, magnetic excitations in the form of spin waves have emerged as the primary means of information transport in spintronics.

Spin waves [11], also called magnons, transport information via a net flow of spin angular momentum. Any time there is a net flow of spin angular momentum, we call this a spin current. When a charge current is flowing through a magnetic material there is a net im-

balance between spin-majority and spin-minority carriers (owing to the spin split density of states), resulting in a net transport of both charge and spin. This is known as an impure spin current. An example of a spin wave and the associated pure spin current, in which there is no charge flow, is shown in Fig. 1.1b. Since these magnetic excitations do not require conduction electrons, not only are they possible in both conducting and insulating magnetic materials which opens up the availability of material platforms, they are free of the problems associated with Joule heating. While spin waves might be a promising means to avoid Joule heating, they are not a perfect solution. However, before we can discuss the challenges that come with using spin waves, we first need to discuss the idea of magnetization dynamics.

1.2 Magnetization Dynamics

The time evolution of a magnetic moment $\vec{m}$ (normal vector, normalized by the saturation magnetization M_{sat}) in a magnetic field $\vec{H}_{eff}$ is governed by the Landau-Lifshitz-Gilbert (LLG) equation [12]

$$\frac{d\vec{m}}{dt} = -\gamma\mu_0\vec{m} \times \vec{H}_{eff} + \alpha\left(\vec{m} \times \frac{d\vec{m}}{dt}\right). \tag{1.1}$$

Here γ is the gyromagnetic ratio, μ_0 is the permeability of free space, α is the dimensionless Gilbert damping parameter, and $\vec{H}_{eff}$ is a sum of all magnetic fields (external, exchange interaction, dipolar interactions, anisotropies, etc.). The LLG equation can be described by two distinct torques acting on the magnetization. The first torque, termed the precessional torque, is described by the first term on the right hand side of Eq. 1.1 and given by the blue arrow in Fig. 1.2. This term will cause the magnetization to precess about the effective field and trace out a path indicated by the dashed circle. The second term on the right hand side of Eq. 1.1 is termed the damping torque and points towards the effective field at all times. As the magnetization precesses, in the absence of external excitation (e.g., microwave field, spin torque, etc.), the cone angle (angle between $\vec{m}$ and $\vec{H}_{eff}$) decreases and the magnetization spirals in towards the effective field, eventually relaxing along it. The rate at which this occurs is governed by the Gilbert damping parameter α.

The Gilbert damping parameter α serves as a catchall term and can have many different relaxation mechanisms contributing to it. When discussing Gilbert damping, typically one is concerned with the intrinsic damping present within a material. This can be attributed to the angular momentum of the precessing magnetization being dissipated to the surrounding lattice, e.g., via spin-orbit coupling. In metals, Gilbert damping can be further broken up into two distinct mechanisms: a resistivity-like (or interband) contribution that scales with electronic scattering rate, and a conductivity-like (or intraband) term that increases with decreasing electronic scattering rate [13, 14, 15]. The electronic scattering rate in a metal scales with temperature. An example of how the resistivity-like and conductivity-like

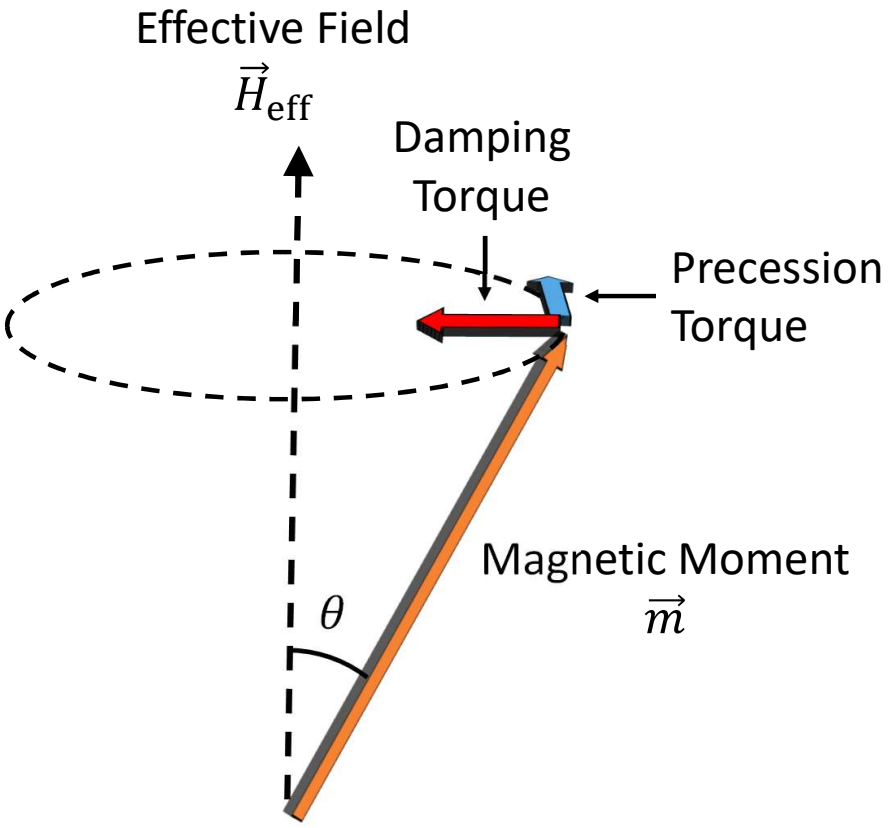


Figure 1.2: Visualization of the torques involved in the LLG equation that governs how a magnetic moment behaves in an effective field. The precessional and damping torques are labelled.

contributions come together to explain the temperature dependence of Gilbert damping in epitaxial Fe films of differing crystalline quality can be found in Fig. 1.3.

If the conductivity-like contribution dominates the resistivity-like contribution, then it is possible to correlate the density of states at the Fermi level with the magnitude of Gilbert damping, as a few studies have been able to demonstrate [15, 16, 17]. When the resistivity-like contribution dominates, no simple relationship exists that can correlate trends in material parameters to the temperature dependence and magnitude of Gilbert damping [15].

Predicting the value of the damping parameter in a material is difficult as many key factors can contribute to it. In addition to the intrinsic mechanisms mentioned above, it is possible for extrinsic mechanisms to contribute. One of the most well-known extrinsic mechanism is two-magnon scattering [18, 19, 20, 21], a process by which the uniformly precessing magne-

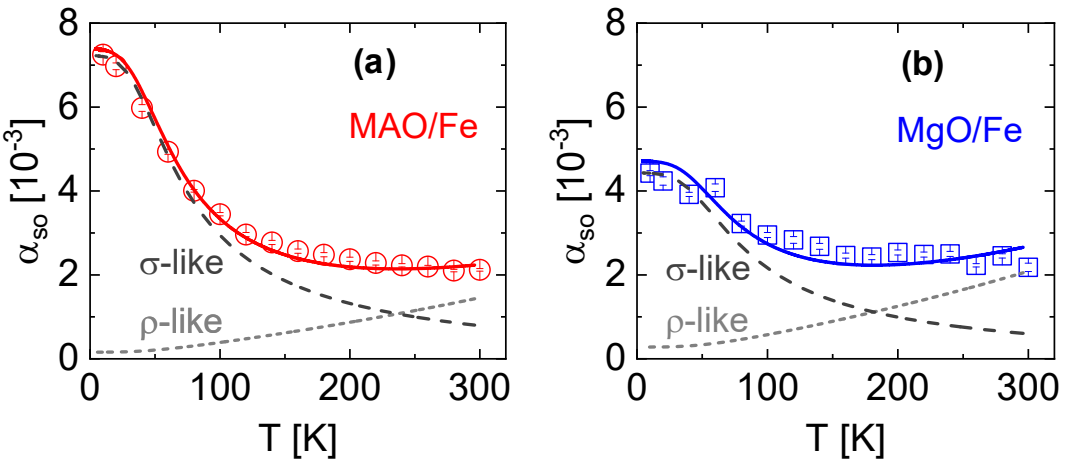


Figure 1.3: Temperature dependence of the intrinsic Gilbert damping parameter for (a) Fe deposited on a $MgAl_2O_4$ (MAO) substrate and (b) Fe deposited on a MgO substrate. Figure is taken from Ref. [1]. These two systems have different degrees of crystallinity and were used as a case to distinguish the role film microstructure plays in Gilbert damping. The two dashed lines show the conductivity-like (σ) and resistivity-like (ρ) contributions to the total intrinsic damping (solid line).

tization scatters into a degenerate non-uniform precession mode. Understanding the origins of two-magnon scattering can be difficult and many studies have been dedicated to understanding how the microstructure of films impacts the magnitude of two-magnon scattering [22, 23, 24, 25].

1.3 Spin Torques

When spin currents interact with magnetic materials, they can transfer their spin angular momentum to the magnetization and exert torques on the magnetization. These spin transfer torques (STTs) [26, 27] have been used to drive the magnetization into precession [28, 29, 30, 31] or switch the magnetization state [32, 33]. Early on this was achieved by passing a charge current through a ferromagnetic layer which resulted in the charge current becoming spin polarized. This is the principle that early magnetic tunnel junctions were based on

where current-perpendicular-to-film-plane was the primary geometry used [28].

More recently, studies have focused on generating spin currents using a current-in-plane geometry. The spin Hall effect [34, 35] is possibly the most well-known charge-to-spin conversion mechanism. Charge current passing through a heavy metal layer experiences a spin-dependent force that deflects spins perpendicular to the direction of charge flow, resulting in a spin current. This spin current has polarization that is perpendicular to both the original charge current and resulting spin current. When the heavy metal layer is interfaced with a ferromagnet, the resulting spin current from the spin Hall effect can exert a torque of the form [27] $\tau_{ST} \propto \vec{m} \times (\vec{s} \times \vec{m})$ where $\vec{m}$ is the magnetization and $\vec{s}$ is the polarization of the spin current. This damping-like torque (named after its similarity to the damping term in Eq. 1.1) can be used to drive easy-axis precession and enable switching of in-plane magnetization. Depending on the sign of $\vec{s}$ it is possible for this torque to effectively enhance the damping torque or reduce it (referred to as a damping-like or antidamping-like torque depending on the orientation, see Fig. 1.2). The spin Hall effect and other mechanisms that give rise to spin-orbit torques (SOTs) [36, 37] have emerged as a promising avenue for controlling the magnetization using conventional electrical means.

Spin-orbit effects in conventional material systems, particularly spin Hall effects in nonmagnetic metals, result in the spin current having an in-plane polarization owing to the strict symmetries that must be adhered to. Recently, interest has been shown in using effects in materials with reduced symmetry (e.g., via magnetic order, specific crystal structures, or structural gradients) to generate spin currents [38, 39, 40] that can have an out-of-plane component to the spin polarization. This has been achieved by breaking the in-plane symmetry along the direction of the charge current, using various different methods [41, 41, 42, 43, 44]. This would allow for perpendicularly magnetized materials, found in high density storage media, to be switched without the need for an external field, which is advantageous for miniaturization of spintronic devices. Work has been ongoing to understand the precise origins and strengths of these effects [44, 45, 46].

1.4 Diffusive Spin Waves

The use of spin waves for carrying spin angular momentum has been a key focus of spintronics. Spin wave dynamics, similar to that depicted in Fig. 1.4a, occur when the local magnetic moments precess with a different phase relative to their neighbors. The small cone angle precession propagates out in all directions and dissipates in magnitude when not driven by an external field. Inherently spin waves undergo diffusive transport, meaning that their amplitude decays exponentially with distance. This exponential decay, shown in Fig. 1.4, occurs on a material dependent length scale. It can range from tens or hundreds of nanometers in metallic ferromagnets [47], to hundreds of microns in high-quality insulating ferrimagnets [48, 49].

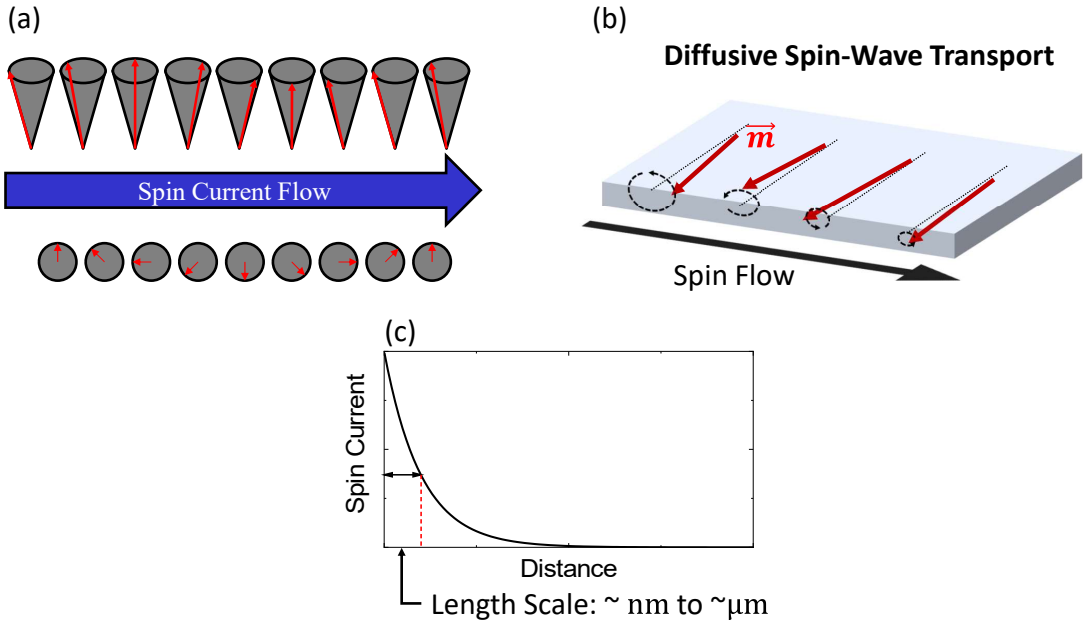


Figure 1.4: (a) Side and top view of a spin wave. Note how the phase of the precession changes from one local magnetic moment to the next, leading to a wave pattern after enough local moments. (b) Visualization of diffusive spin waves dynamics in a magnetically ordered material where the dynamics propagate down the length of the strip. (c) The associated exponential decay of spin current.

If spin waves are to emerge as a viable means of information transport, they need to be able to propagate beyond micron-scale distances without significant losses. Additionally, if this idea is to be adopted by companies, the material platform of choice needs to be easily integratable into existing semiconductor fabrication processes. Unfortunately this rules out the ultra-low damping insulating ferrimagnets [50, 51] as the processing temperatures (e.g., >700°C) and fine control of deposition parameters make film growth both expensive and difficult to reproduce. Metallic ferromagnets can be easily grown at processing temperatures near room temperature and have demonstrated very low damping parameters [52, 53, 54].

There is an outstanding challenge of realizing efficient spin transport in metallic ferromagnet systems. The diffusive nature of spin waves prevents propagation distances extending beyond the micron-scale. Beyond fine tuning of material parameters, an alternative form to the small cone angle magnetization dynamics provides a promising avenue for establishing spintronics as a viable replacement for electronic charge currents.

1.5 Spin Superfluidity

Spin superfluidity is a phenomenon that has been proposed as a means of achieving long-distance information transport in magnetically ordered materials without significant losses [55, 56, 57, 58, 59, 60, 61, 62, 63]. It can be thought of as a magnetic analogue of superconductivity [64] or mass superfluidity [65] and takes its name from the underlying theoretical framework being similar to that of the two aforementioned phenomena and similarity to hydrodynamics [66].

One feature that makes spin superfluidity unique from conventional diffusive spin waves is the largely easy-plane precession of the magnetization, as opposed to the magnetization undergoing precession with a relatively small cone angle about the equilibrium axis. We can understand spin superfluidity by using a simple Hamiltonian that describes the two key contributors at play. The simplest Hamiltonian that can describe an easy-plane ferromagnet is given as

$$H = \frac{A}{2}(\nabla \vec{m})^2 + \frac{K_z}{2}(m_z)^2, \tag{1.2}$$

where A is the strength of exchange coupling, $\nabla \vec{m}$ is the gradient of the magnetization, $K_z > 0$ is the strength of the easy-plane anisotropy, and m_z is the out-of-plane component of the magnetization. The lowest energy state corresponds to the magnetization lying fully within the film plane and all magnetic moments collinear with one another. It is possible to parameterize the magnetization in terms of the out-of-plane magnetization m_z and an in-plane azimuthal angle ϕ defined with respect to the x axis, such that the Hamiltonian can be rewritten as

$$H = \frac{A}{2}(\nabla \phi)^2 + \frac{K_z}{2}(m_z)^2. \tag{1.3}$$

The two energy terms, exchange and easy-plane anisotropy, as well as the parameterization of $\vec{m}$, can be visualized using Fig. 1.5a-c, respectively. From here, one can determine the Hamilton's equations for ϕ and m_z. These are

$$\dot{\phi} = K_z m_z \tag{1.4}$$

and

$$\dot{m}_z + \nabla \cdot J_s = 0, \tag{1.5}$$

where $\dot{\phi}$ ($\dot{m}_z$) indicates a derivative of ϕ (m_z) with respect to time. In Eq. 1.5 J_s is the spin current, defined as [55]

$$J_s = -A \nabla \phi, \tag{1.6}$$

where $\nabla \phi$ represents the spatial gradient of ϕ. Eqs. 1.4 and 1.5 closely resemble those of hydrodynamics [66] and serve as the inspiration for the name spin superfluidity. With the picture described above, it is possible to derive a wave equation for ϕ using Eqs. 1.4 and 1.5.

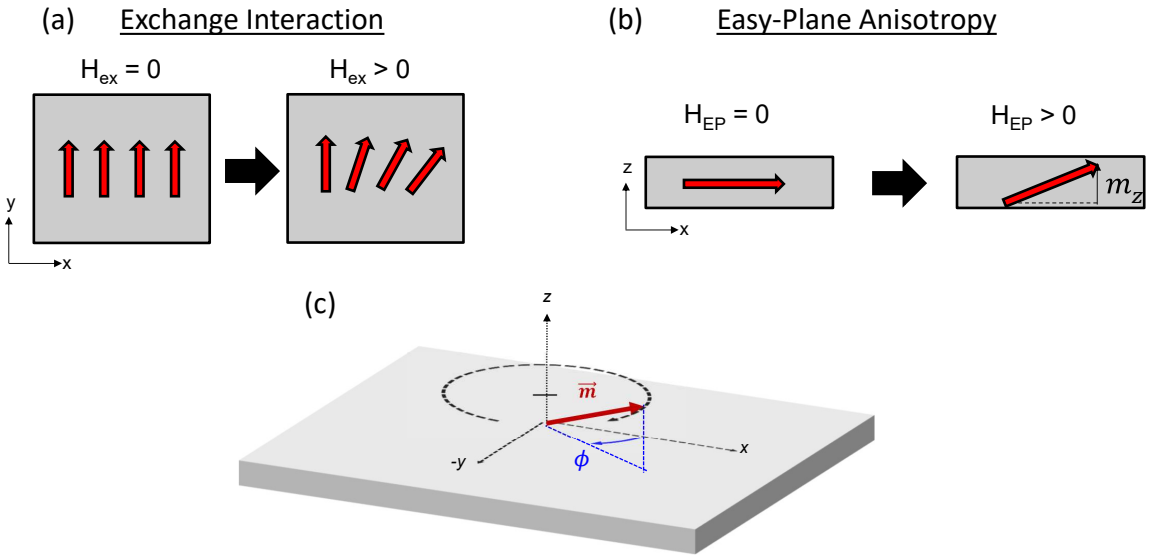


Figure 1.5: Visualization of the two terms found in Eq. 1.2: (a) the exchange interaction, which favors a parallel configuration of spins, and (b) easy-plane anisotropy, which prefers the magnetization to lie within the xy plane of the film. (c) The definition of the variables used to parameterize the magnetization.

Solving that we find that ϕ evolves at a uniform rate over time and m_z remains constant throughout the strip. This means that the magnetization has a small and constant out-of-plane component while it precesses with a cone angle $\sim 90°$ with respect to $\hat{z}$ at a constant rate, as shown in Fig. 1.6a.

A better way to understand what is happening here is to think about it in a step-by-step manner using the idea of torques. First the magnetization is lifted out of the plane of the film at one end of a magnetic strip, e.g. via spin transfer torque [26]. The resulting demagnetizing field attempts to pull the magnetization back into the plane of the film and thereby exerts a precessional torque, driving the easy-plane precession. This precession then propagates along the length of the strip due to exchange coupling with a uniform out-of-plane magnetization component m_z and constant phase gradient $\nabla\phi$. These dynamics suggest a constant spin current would be flowing through the strip. However, an important factor – i.e., dissipation that is invariably present in all magnetic media – has been ignored in this analysis thus far; we elaborate on this factor in the following subsection.

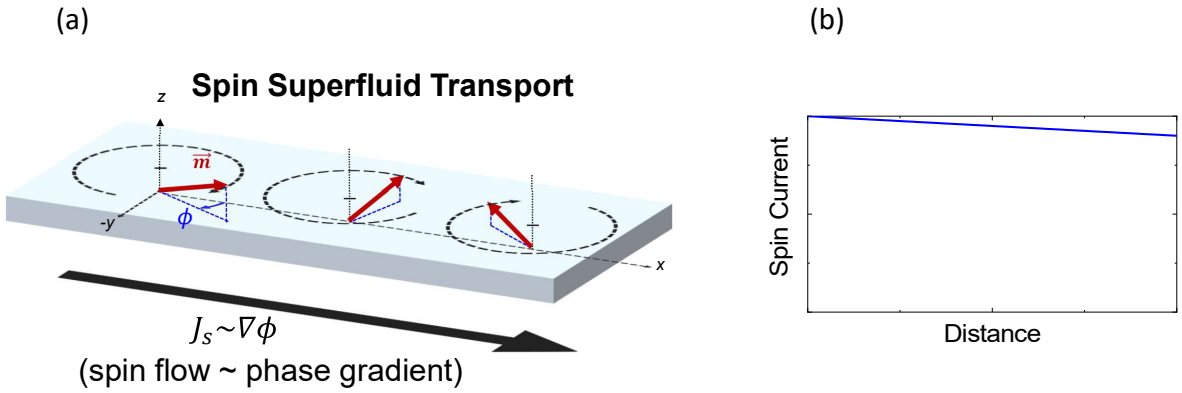


Figure 1.6: (a) Spin superfluid dynamics where the magnetization vector precesses within the plane of the film. The out-of-plane component of the magnetization m_z is constant with position and the magnetization makes an angle ϕ with the $\hat{x}$ axis. The spin flow is defined to be along the direction of the phase gradient. (b) Once Gilbert damping is considered, the spin current exhibits a linear decay with distance.

1.5.1 Superfluid-*like* Spin Transport

In the perfect regime in which Gilbert damping can be ignored, we have seen that J_s is conserved throughout the strip. However, Gilbert damping can never be ignored and is an ever-present dissipation mechanism. Because of this, the term "spin superfluidity" is a misnomer as true superfluidity (i.e. dissipationless transport) is not possible in magnetic materials. Once Gilbert damping is considered, the easy-plane precession no longer precesses at a uniform rate as it propagates down the strip, with the spatial wavelength of the magnetization spiral pattern increasing with distance. This results in the spin current J_s exhibiting a linear decay with distance [55, 61, 62], similar to that shown in Fig. 1.6b. Because of this, we refer to this phenomenon as "superfluid-like spin transport" (SLST) to avoid confusion with true superfluidity. Even though dissipation is present in SLST, the linear decay with distance offers substantial improvement over the exponential decay found with the diffusive spin waves discussed in Sec. 1.4.

In addition to Gilbert damping, there are other effects that alter the perfect nature of spin superfluidity. Two major factors are in-plane magnetic anisotropies and long-range dipolar interactions. Magnetic anisotropies, while crucial for SLST as easy-*plane* anisotropy is required, can have an adverse effect on the dynamics when they create an easy-*axis* within

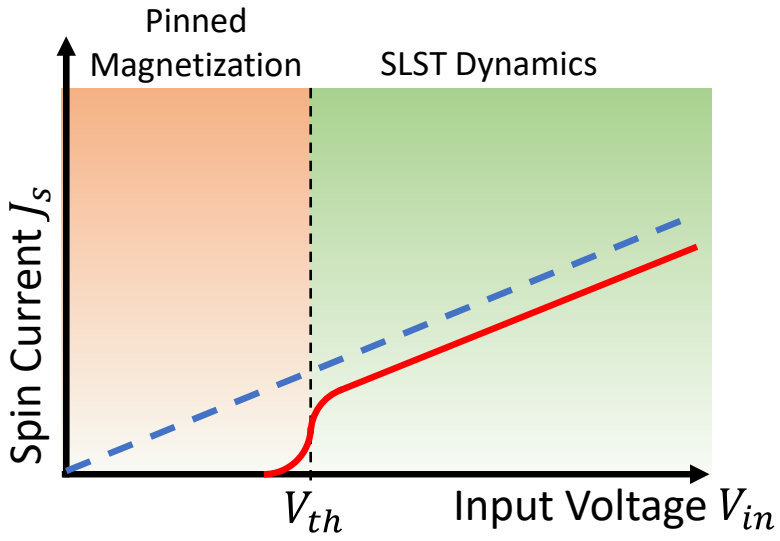


Figure 1.7: Detected spin current J_s as a function of driving voltage V_{in}. In the absence of in-plane anisotropy, the detected spin current will have a linear relation with driving voltage and no threshold, as shown by the dashed line. In-plane anisotropies and Gilbert damping introduce a threshold energy V_{th} that must be overcome to excite dynamics (solid line).

the plane of the film. This can result due to either magnetocrystalline anisotropy, shape anisotropy, or both. The result is a pinning effect on the rotating magnetization vector as there is now an energy threshold the magnetization must overcome to rotate within the plane of the film. Not only will this result in a finite energy threshold required to induce precession but the uniform gradient in easy-plane precession will now be broken up into distinct domain wall-like entities [62]. This threshold and its effects on SLST dynamics can be visualized using Fig. 1.7. Dipolar interactions from the sample edges play a role by destabilizing the easy-plane dynamics, resulting in the superfluid not being able to propagate spin current beyond extremely short distances [67].

1.5.2 Practical Considerations

We have already discussed how Gilbert damping, magnetocrystalline anisotropy, and long-range dipolar interactions can adversely affect SLST. Considering these effects, it is relatively straightforward to minimize their impacts on a material platform. Our ultimate goal in this dissertation is to take steps towards establishing a material platform capable of supporting

SLST. We choose to use metallic ferromagnets as they are more readily compatible with semiconductor device fabrication processes. We will want this material platform to have ideally an ultra-low damping parameter ($\alpha \leq 0.001$) and negligible magnetocrystalline anisotropy, thus requiring polycrystalline materials. Long-range dipolar interactions from the sample edges can be easily compensated using synthetic antiferromagnets, a trilayer structure where two ferromagnet layers have their respective magnetization antiparallel to the other layer [68].

There have been claims of superfluid-like spin transport in other materials systems, namely *anti*ferromagnetic materials. Stepanov *et al.* claim to have observed SLST in a particular state of graphene [69] while Yuan *et al.* claim that the ground state of antiferromagnetic oxide Cr_2O_3 is a spin superfluid-like state [70]. While both of these claims have their merits, they have significant downsides when it comes to practicality. Both of these studies look at dynamics at cryogenic temperatures with their samples placed in high magnetic fields ($\sim 9-18$ T, a result of their antiferromagnetic nature and the need to cant the magnetization out-of-plane). The metallic ferromagnet system we propose to use is theoretically expected to sustain superfluid-like spin transport at any temperature that is well below the magnetic ordering temperature [62, 71] and does not require an external field to generate a non-zero magnetization. These two material systems are also not compatible with Si substrates. While from a fundamental standpoint these are important results, an experimental achievement of SLST dynamics in a metallic ferromagnet system will go a long way towards developing an understanding of spin transport but also bring the field of spintronics closer to widespread device integration.

1.6 Dissertation Outline

The goal of this dissertation is to advance the community's understanding of how to achieve superfluid-like spin transport in metallic ferromagnets. There are a number of unanswered questions in this regard. We aim to address some of those questions here.

A first large hurdle concerns the order of magnitude higher Gilbert damping in metallic ferromagnets compared to insulating ferrimagnets and what effect that might have on SLST dynamics. If low Gilbert damping is a necessity for SLST, understanding how to reduce damping in metallic ferromagnets is essential. If damping can be predictably tuned in metallic ferromagnets, this would not only go a long way towards developing a platform for SLST but also for other low-power spintronics devices, such as spin transfer torque magnetic storage cells.

Micromagnetic simulations provide a powerful tool in predicting and understanding how magnetization dynamics behave in various systems with a wide range of material properties and phenomena. This can be leveraged to simulate SLST with material parameters similar to low damping metallic ferromagnets and provide an early tool on the feasibility of this

phenomenon. Various geometry and device structures can be studied to predict what the optimal values are for e.g. damping, saturation magnetization, excitation currents, etc. Additionally, the result of these simulations can be compared with theoretical works to create a better understanding of the underlying physics.

A sound theoretical understanding of how to excite SLST is well known, but experimentally there remain challenges. SLST requires an out-of-plane spin polarized current exerting a spin transfer torque on an in-plane magnetized strip. The most straightforward and established way to do this is to use current-perpendicular-to-plane nanopillars [28]. However, this requires precise lithographic patterning and can be quite tricky when designing structures on the sub-micron scale. If one can design a more straightforward method of excitation using a current-in-plane geometry to achieve out-of-plane polarized spin currents, then this can ease the burden of designing a device.

The outline of the remaining chapters of this dissertation is structured in the following way: In Ch. 2 we briefly outline the experimental methods for thin film growth and characterization used throughout this work. Ch. 3 discusses the development of an ultra-low damping metallic ferromagnet system to be used as the basis for superfluid-like spin transport. Ch. 4 uses the results of the material platform developed in the previous chapter to focus on micromagnetic simulations that investigates how superfluid-like spin transport emerges from a train of condensing magnetic domain walls. Ch. 5 investigates the presence of unconventional spin torques in a current-in-plane spin valve structure that could be used for the excitation of superfluid-like spin transport and shed light on the nature of spin-orbit torques in magnetically ordered systems. Finally Ch. 6 looks to the future at what steps remain towards an experimental realization of this phenomenon as well as potential wider impacts. Ch. 7 lists other publications I contributed to while working towards my PhD.

Chapter 2

Experimental Methods

This chapter gives a brief introduction to the experimental methods used throughout my PhD. There are a variety of techniques included, ranging from thin film growth to magnetic, electrical, and structural characterization.

2.1 Magnetron Sputtering

All of the thin film samples in our lab, including a majority of the samples discussed in this dissertation, are grown using magnetron sputtering. Sputtering is a form of physical vapor deposition in which a material is stripped from a source (referred to as a "target") via bombardment of a processing gas and then deposited onto a substrate. This is done by Ar ions being accelerated towards the target and continuously bombarding the target to strip material away. The removed material then deposits itself onto a substrate, creating a thin film of material on the substrate.

The system located in our lab is a high-vacuum AJA International sputtering system with a base pressure inside the chamber of $< 5 \times 10^{-8}$ Torr. It consists of a common loadlock and two nearly identical sputtering chambers on either side of the loadlock. The substrate carrier and substrate are loaded into the common loadlock and then transferred to the main sputtering chamber.

Each main chamber has a variety of instruments that are responsible for controlling various aspects of the system. These include controls for sputtering gun power supplies, pressure monitors, turbo valve position, sample heater and rotation stage, DC ion source (RHS chamber only), and turbo speed indicators. Most of these can be controlled remotely from the laptop computer or adjusted locally using the front panel on each instrument. The system can be seen in Fig. 2.1 with the loadlock, main chambers, and instrument panels labeled.

Inside the main chamber, the substrate carrier is loaded onto a paddle holder that rotates at a set rate during the deposition process to ensure a uniform coating. The substrate carrier can accommodate a wafer up to 3 inches in radius, but commonly much smaller pieces are used. The substrate can be raised to an elevated temperature by using a built-in heating element used for high temperature deposition with a maximum temperature of 850 °C.

Below the substrate stage are the sputtering guns arranged in a confocal setting, meaning that they are slightly off-axis and do not point directly at the substrate carrier. Multiple sputtering guns can be found in each chamber and moved between the chambers as necessary. Within the RHS chamber (see Fig. 2.1) is a smaller sputtering gun that is used for deposition of precious metals. This particular gun uses a smaller source target, 1 inch instead of 2 inches, meaning less material is required which is helpful when sputtering expensive materials (e.g. Au, Pt, Pd, etc.). Additionally in the RHS chamber is a DC ion source, located directly below the substrate carrier, used for ion milling.

Below is a general outline for how to perform magnetron sputtering using the AJA system

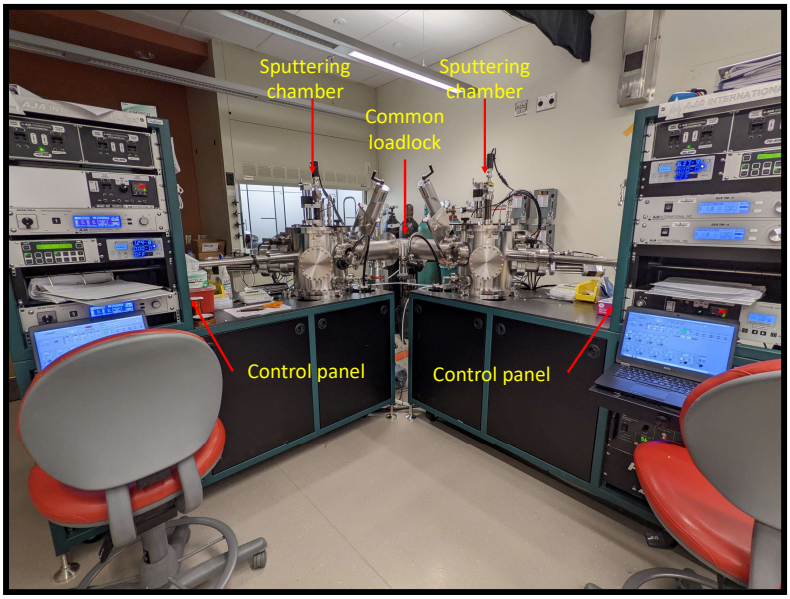


Figure 2.1: Picture of the AJA dual chamber sputtering system. The two chambers are nearly identical, with the exception of the right-hand-side chamber containing a DC ion source for ion milling.

found in our lab:

1. Flow Ar processing gas in the chamber until you achieve the desired pressure, typically 30 mTorr. This is typically done by setting a fixed Ar gas flow rate ($\sim$ 35 sccm) and adjusting the valve position near the turbopump.

2. Set the power on the sputtering gun of interest to the target power (typically 80 W is used) and wait for the resulting plasma to stabilize (indicated by a purple dot on the user interface, also visible as a purple glow inside the sputtering chamber)

3. Once the plasma has stabilized, keep the sputtering power fixed at 80 W and reduce the Ar pressure to the desired level at which the deposition will be done. This is typically around $\sim 3-4$ mTorr. The lower the better as lower sputtering pressure typically helps to ensure smoother film growth; an excessively high sputtering gas pressure can result in a rough film surface, e.g. due to a reduced mean free path (atoms scattering

more frequently before deposited on the substrate) or damage from resputtering of the film surface.

4. Open the shutter on the sputtering gun and allow the material to be deposited on the substrate. The amount of material deposited is estimated from the known deposition rate (calibrated using XRR, discussed in Sec. 2.5.2) and deposition time, giving a thickness of material

5. Once the deposition is complete, close the shutter on the sputtering gun, turn off the sputtering power, stop the Ar gas flow, fully open the valve. The pressure in the chamber should begin to return to high-vacuum levels ($< 10^{-7}$ Torr, as indicated by the pressure gauge on the front panel of the sputtering system)

The above process is then repeated for multiple layers. Additionally, one can supply power to up to three sputtering guns at once to deposit multiple materials at the same time (known as co-sputtering, useful for the deposition of alloys from individual material targets).

2.2 Ferromagnetic Resonance

Ferromagnetic resonance (FMR) is a phenomenon useful for studying magnetization dynamics within a material in which a radio frequency (RF) excitation is applied to a magnetic material [72, 73]. The two different methods of FMR used in this dissertation are discussed in Secs. 2.2.1 and 2.2.2. Detailed discussions on the underlying theory of FMR can be found in Ref. [74] for broadband FMR (BB-FMR) and in Ref. [75] for spin torque FMR (ST-FMR).

2.2.1 Broadband Ferromagnetic Resonance

To excite ferromagnetic resonance, a thin film sample is placed film-side down on the coplanar waveguide (CPW). The CPW is connected on one end to a microwave source (HP Agilent 83650A, maximum frequency 50 GHz) that supplies a RF magnetic field $\vec{H}_{RF}$ to the sample and to a microwave diode and lock-in amplifier on the other end. Perpendicular to $\vec{H}_{RF}$ is a DC magnetic field $\vec{H}$ generated by a GMW electromagnet (maximum field ~ 1.1 T) and a time varying magnetic field (frequency 700 Hz) from a pair of modulation coils that is used as a reference signal for the lock-in amplifier. In this particular setup, the frequency of the RF field is kept constant while the DC magnetic field is swept through a range while the transmitted microwave power P (or the microwave power absorbed by the sample) is monitored via the RF diode. The waveguide allows for a wide frequency range to used instead of being restricted to a much narrower (sometimes single) frequency when using a cavity set-up (hence the name broadband FMR). The rectified signal from the RF diode (modulated by the 700-Hz modulation field) is measured by the lock-in amplifier. Hence,

the "FMR signal" that we measure here is not the microwave power P per se, but rather dP/dH, the derivative of the microwave power with respect to the swept DC magnetic field. An example schematic of this set-up is shown in Fig. 2.2 and the physical set-up shown in Fig. 2.3.

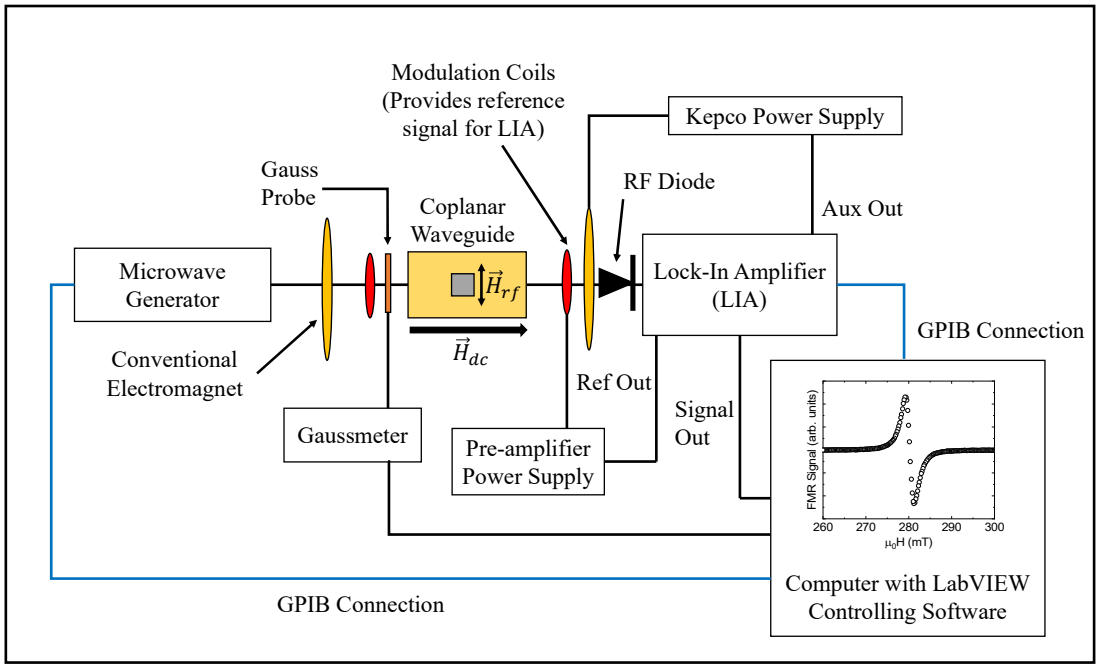


Figure 2.2: Detailed schematic of the various instruments used in broadband ferromagnetic resonance (BB-FMR) setup.

The FMR signal we detect can be fit using a combination of a symmetric and antisymmetric Lorentzian derivative:

$$\frac{dP}{dH} = -A\left(\frac{2(H-H_{res})\Delta H}{((\Delta H^2)+(H-H_{res})^2)^2}\right) + D\left(\frac{(H-H_{res})^2-(\Delta H)^2}{((\Delta H^2)+(H-H_{res})^2)^2}\right). \tag{2.1}$$

Here H is the strength of the applied DC magnetic field, H_{res} is the FMR resonance field, ΔH is the half-width-at-half maximum FMR linewidth and A (D) is the strength of the absorptive (dispersive) term. H_{res}, ΔH, A, and D are all used as free fit parameters for the FMR spectra.

To determine material parameters, one needs to understand how the FMR resonance field H_{res} and FMR linewidth ΔH depend on microwave frequency. The ferromagnetic resonance field condition for polycrystalline samples with the magnetization lying in the plane of the film is given by the Kittel equation [72]:

$$f = \gamma' \mu_0 \sqrt{H_{res}(H_{res}+M_{eff})}, \tag{2.2}$$

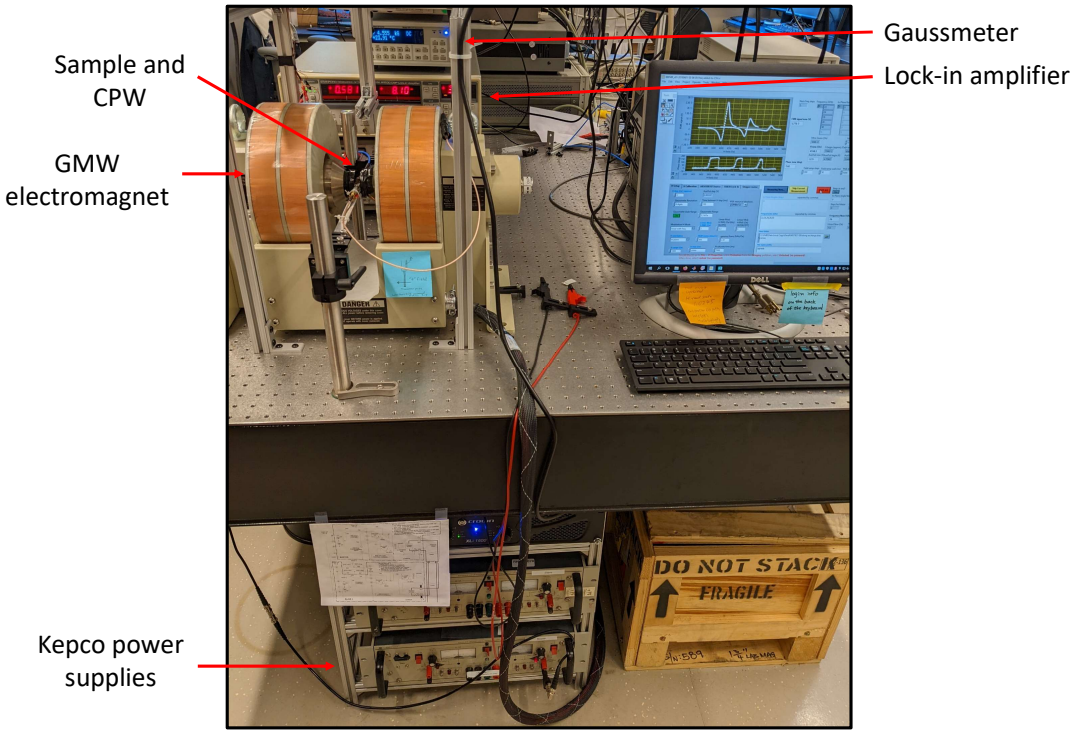


Figure 2.3: BB-FMR setup with various components labelled.

where $\gamma' = \gamma/2\pi$ is the reduced gyromagnetic ratio, μ_0 is the permeability of free space, and M_{eff} is the effective magnetization. Eq. (2.2) changes if the magnetization is perpendicular to the film plane, if magnetocrystalline anisotropy is non-zero, etc. Various examples of these particular cases can be found in Ref. [76]. From Eq. (2.2) we can see that it is beneficial to measure FMR across a wide range of frequencies. This is the advantage that the broadband setup here offers, as compared to microwave cavities.

To determine the magnitude of Gilbert damping in the material, one studies how the FMR linewidth depends on excitation frequency. The typical prescription is to use the linear relation [18]

$$\Delta H = \Delta H_0 + \frac{\alpha}{\gamma' \mu_0} f, \tag{2.3}$$

where γ' is taken as a fixed parameter from Eq 2.2, ΔH_0 is the zero frequency linewidth, and α is the dimensionless Gilbert damping parameter. From this we can see that the FMR linewidth should have a linear dependence on the frequency as long as Gilbert damping is the dominate form of magnetic relaxation. However, this is not always the case as it is possible for extrinsic mechanisms to contribute to the measured damping parameter and/or produce

a nonlinear frequency dependence of the FMR linewidth[18]. One very common example of this is known as two-magnon scattering and manifests in the form of a non-linear dependence on frequency [19, 20, 21, 25, 77]. Two-magnon scattering can be suppressed by performing FMR with the magnetization aligned perpendicular to the film plane [77], allowing for the determination of the intrinsic Gilbert damping parameter.

2.2.2 Spin Torque Ferromagnetic Resonance

Spin torque FMR (ST-FMR) is a variation of the BB-FMR technique introduced in the previous section (see Sec. 2.2.1). Instead of using an external RF magnetic field to excite precession, a RF charge current is applied to a sample. These samples are typically heavy-metal/ferromagnet bilayers [78, 79] but this technique can also be applied to multilayers with multiple magnetic materials [80, 81].

In ST-FMR, the in-plane charge current $I(t) = I_{RF}\cos(\omega t)$ (where $\omega = 2\pi f$ and f is the applied excitation frequency) passes through a material with high spin-orbit coupling, which in turn generates a spin current that is absorbed by a nearby magnetic layer. This absorbed spin current exerts a torque on the magnetization [27] and causes the magnetization to precess. The precessing magnetization induces oscillations in the sample's electrical resistance due to the anisotropic magnetoresistance effect (deviation of the sample's magnetization and charge current direction) [82], thereby changing the samples resistance as a function of time $R(t) = R_{AMR}\cos(\omega t)$. The RF charge current and time varying resistance couple together and result in a rectified voltage of the form

$$V_{mix} = I_{RF}\cos(\omega t)R_{AMR}\cos(\omega t) = V_{DC} + V_{2f}\cos(2\omega t). \tag{2.4}$$

The rectified voltage has two components: a DC component and a RF component at a frequency $2f$, where f is the frequency of the applied RF charge current. The DC component is detected by a lock-in amplifier and measured as a function of the applied magnetic field.

An example of the ST-FMR set-up used is shown in Fig. 2.4. The samples are placed onto a stage in the center of a rotatable electromagnet with maximum field of $\sim$ 1000 Oe. The samples are contacted with a ground-signal-ground probe that is connected to a bias tee. The bias tee is connected to a microwave generator (HP Agilient 83632B) by the capacitor port and to a lock-in amplifier (SR830) and sourcemeter (Keithley 2400 Sourcemeter) via the inductor port. A schematic example of this is shown in Fig. 2.5. Of the two multimeters, one (Keithley 2000, lower in picture) is used to directly measure the strength of the magnetic field via a Hall element attached to the electromagnet; the other multimeter (top) is used to supply a DC charge current and measure sample resistance. The applied magnetic field is controlled by the Aux Out of the lock-in amplifier and is connected to a Kepco power supply. The output of the Kepco is then connected to the electromagnet to generate the magnetic field necessary for FMR. The reference signal output from the lock-in amplifier is

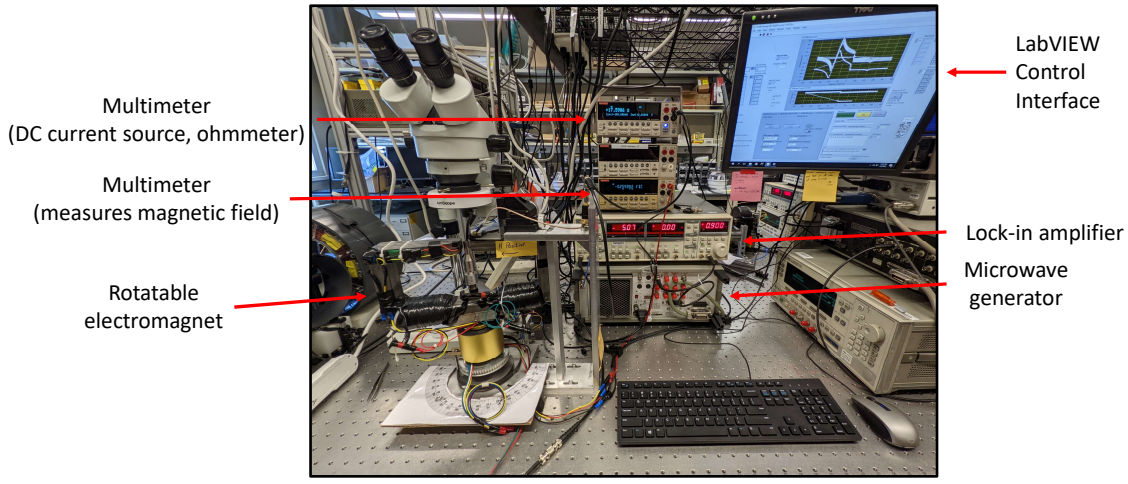


Figure 2.4: The ST-FMR setup used in the lab with various important components labelled. The Kepco power supplies are located below the optical table and are not shown.

connected to the amplitude modulated (AM) input of the RF source and helps to boost the signal-to-noise ratio of the overall measurement [83].

ST-FMR spectra are acquired in a manner similar to that of the BB-FMR setup: a fixed frequency charge current is applied and the DC magnetic field is swept through a predetermined range. The rectified voltage V_{mix} is measured by the lock-in amplifier as a function of applied magnetic field. V_{mix} can be described using a combination of symmetric and antisymmetric Lorentzians

$$V_{mix} = V_S \frac{\Delta H^2}{\Delta H^2 + (H - H_{res})^2} + V_A \frac{\Delta H (H - H_{res})}{\Delta H^2 + (H - H_{res})^2}, \tag{2.5}$$

where S (A) is the amplitude of the symmetric (antisymmetric) component, H is the magnitude of the applied magnetic field, H_{res} is the FMR resonance field and ΔH is the FMR linewidth. Using the rotatable electromagnet, ST-FMR spectra can be acquired at various in-plane angles to understand the nature of any spin torques present within the sample being measured. In general, the angular dependence of the ST-FMR signal can be described by

$$V_{mix} = \frac{dR}{d\phi} \tau(\phi), \tag{2.6}$$

where R is the sample resistance that arises from the anisotropic magnetoresistance (AMR) and/or giant magnetoresistance (GMR) effects, ϕ is the angle between the direction of current

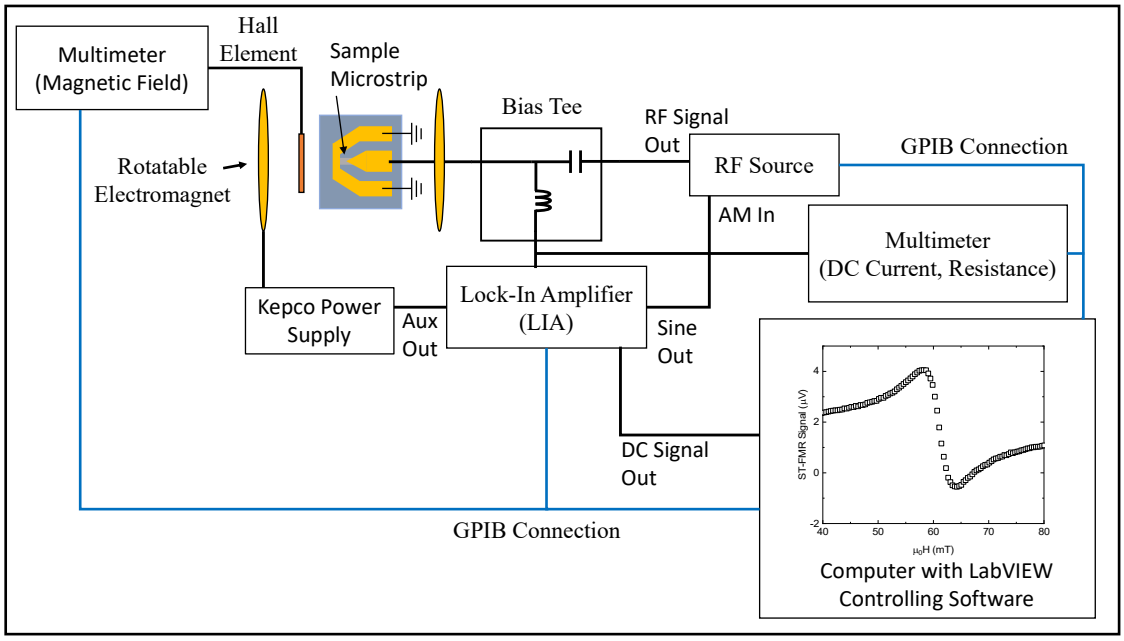


Figure 2.5: Detailed schematic example of the ST-FMR setup. The bias tee is located in the center and connects the sourcemeters, lock-in amplifier, and RF source to the sample via a ground-signal-ground probe.

flow and the applied magnetic field, $dR/d\phi$ is the derivative of sample resistance, and $\tau(\phi)$ are the torques acting on the magnetic layer to induce oscillations.

The advantage of using ST-FMR instead of BB-FMR lies in the fact that this technique can be used to directly probe spin torques that are present within a system. By studying the angular dependence of V_{mix} or the dependence of V_{mix} on a DC bias current, the origin and direction of spin torques can be determined, as well as if they are field-like or damping-like torques. This technique is also useful for estimating the magnitude and sign of the spin Hall angle in heavy metals [78], anomalous Hall effect in ferromagnets [84], torque efficiencies [85], and recently, unconventional spin torques in systems with reduced symmetries [42, 43, 80].

2.3 Vibrating Sample Magnetometry

Vibrating sample magnetometry (VSM) is a technique that can be used to measure the static magnetic properties of a material. This is done in our lab using a Microsense EZ-9 VSM, shown in Fig. 2.6. The system is comprised of a electromagnet (maximum field ~ 2.2 T) and a vibrating rod onto which the sample is placed. The sample is vibrated at a set frequency of

80 Hz. The vibrating magnetic sample generates a time varying magnetic flux that in turn generates a current in a pair of coils via Faraday's law of induction. This induced current is then detected by a lock-in amplifier by using a reference signal at the same frequency as the sample vibration. The voltage detected by the lock-in amplifier is then converted to a magnetization by using a magnetic reference standard (in this case, a disk of Ni with known magnetization and sample mass).

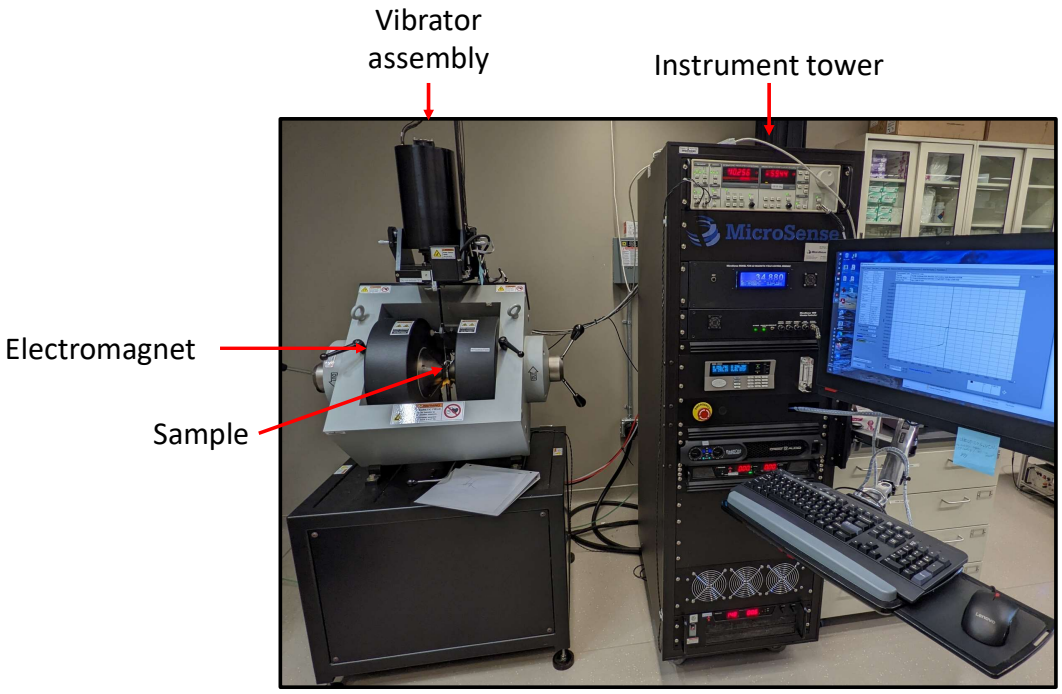


Figure 2.6: Microsense EZ-9 VSM system used for measuring hysteresis loops. The electromagnet and vibrator assembly is shown on the left and the instrument tower with computer monitor is shown on the right.

VSM can be used to measure how a magnetic sample responds to an externally applied magnetic field, typically in the form of a hysteresis loop. This particular instrument can measure hysteresis loops as a function of applied field angle by rotating the sample through a full 360°, with sample holders available that allow for full rotation within the film plane or rotate the magnetization from fully in-plane to fully out-of-plane. Additionally, the measurements can be performed as a function of temperature through a range of 77 K, using liquid nitrogen, up to 1000 K, using the built-in heater and Ar gas.

An example of a room temperature hysteresis loop for 20 nm of Fe is shown in Fig. 2.7.

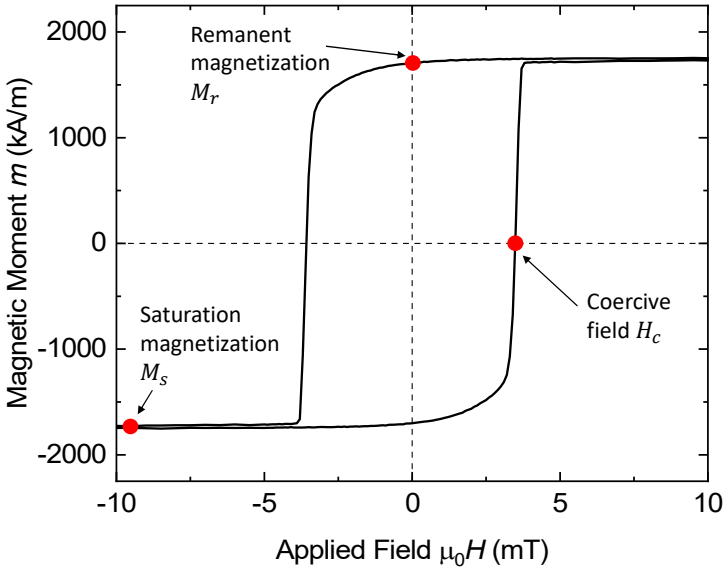


Figure 2.7: Example of a hysteresis loop obtained using the Microsense EZ-9 VSM for 20 nm of Fe at room temperature.

The key quantities of interest, labeled in the figure are: 1) saturation magnetization M_s, the maximum value of magnetization measured for a sample; 2) the remanent magnetization M_r, or the sample magnetization when the applied field has been removed; and 3) the coercive field H_c, the reverse applied field needed to fully demagnetize a sample. The accompanying software for this VSM instrument can automatically determine these quantities by taking an average of the two field sweeps (negative to positive and positive to negative). This software can be prone to error so it is wise to double check the reported values manually. Hysteresis loops can also give insight in any potential magnetic exchange bias [86, 87], magnetic anisotropies [88, 89], and impacts of alloying [90, 91].

2.4 Electrical Transport

This section includes a brief discussion of the DC probe station. This station is used to measure sheet resistance of a sample using the van der Pauw (vdP) configuration and to measure magnetoresistance using the vdP configuration and a pair of Helmholtz coils. A picture of the setup is shown in Fig. 2.8.

The van der Pauw method is commonly used for measuring the Hall effect but can also be used for determining sheet resistance R_S. In this method, four electrical probes are placed on the corners of a square thin film sample. Current is sent along one edge of the sample

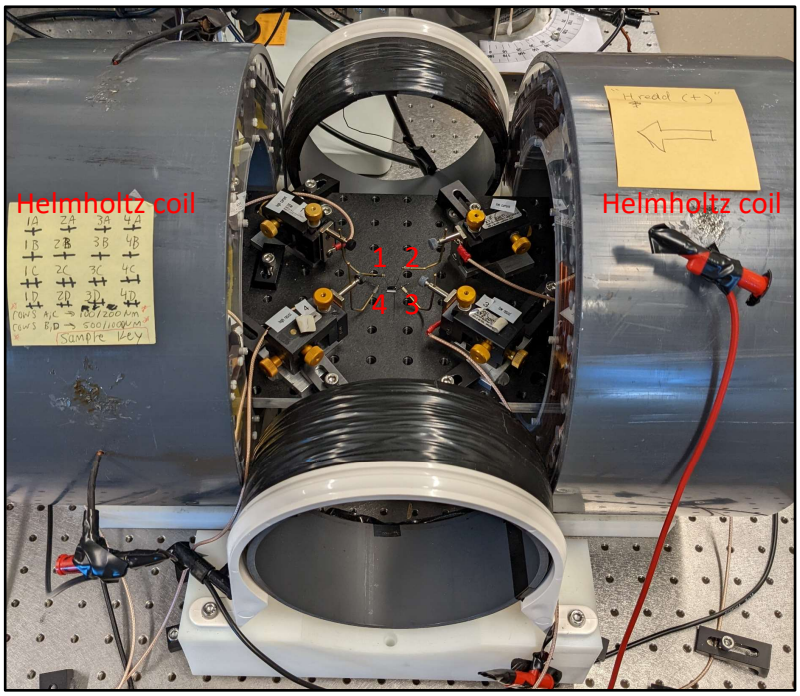


Figure 2.8: DC probe station with the Helmholtz coils used for measuring giant magnetoresistance. The smaller white coils are used for measuring the planar Hall effect.

and the voltage drop is measured along the other parallel edge (e.g. in Fig. 2.8, current would be sent from $1 \rightarrow 4$ and voltage measured $2 \rightarrow 3$). From this, the resistance along that direction can be determined using Ohm's Law

$$R_{23,14} = V_{23}/I_{14}. \tag{2.7}$$

This is then repeated for the other edge to determine $R_{12,43}$. The sheet resistance can then be calculated by numerically solving

$$e^{-\pi R_{12,43}/R_S} + e^{-\pi R_{23,14}/R_S} = 1 \tag{2.8}$$

for R_S.

Additionally, this set-up can be used to measure various forms of magnetoresistance (anisotropic magnetoresistance, giant magnetoresistance, etc.) by means of a pair of Helmholtz coils to

generate a magnetic field. The larger pair of coils can generate a magnetic field up to ~ 100 Oe (~ 10 mT). The smaller Helmholtz coils are primarily used for measuring the planar Hall effect [92], a phenomenon not discussed here.

2.5 X-Ray Techniques

Structural characterization was done by using x-ray diffraction and x-ray reflectivity. X-ray diffraction (XRD) was primarily used for determining the crystal orientation and lattice mismatch, while x-ray reflectivity (XRR) is used for measuring the thickness of single layer thin films. Two different instruments were utilized throughout this dissertation: a standard Bruker D8 with a high signal-to-noise ratio for XRD of polycrystalline films and a high-resolution Pan'alytical XRD for XRD scans of epitaxial films where the higher angular resolution is needed. Both instruments can be used for XRR measurements.

2.5.1 X-Ray Diffraction

X-ray diffraction (XRD) is a technique that can be used to determine crystal structure, presence of specific phases, mosaic spread, epitaxial strain, and many other properties of thin films [93, 94, 95]. The geometry of the measurement setup is shown in Fig. 2.9a. Diffraction peaks occur when the Bragg condition

$$\lambda = 2d\sin(\theta) \tag{2.9}$$

is satisfied. Here λ is the wavelength of x-ray radiation, d is the spacing between lattice planes, and θ is the angle defined in Fig. 2.9a. Most XRD/XRR scans performed were symmetric $2\theta-\omega$ scans, meaning that both angles were scanned at the same rate. Symmetric XRD scans will typically reveal one (sometimes two) diffraction peaks that can be attributed to the substrate and multiple peaks that can be attributed to the deposited film. By studying the 2θ location of these peaks and their relative intensity, it is possible to determine what phases are present and what the orientation is of the grown film.

An example of a symmetric scan for epitaxial $Fe_{90}V_{10}$ grown on a $MgAl_2O_4$ (MAO) substrate is shown in Fig. 2.9b. This scan reveals a film peak at $2\theta \sim 64.3°$ that corresponds to the (002) lattice planes and a much more intense substrate peak at $2\theta \sim 44.8°$ that corresponds to the (004) lattice planes. The fact that only peaks from the (00l) family are observed confirm that epitaxial growth of film.

Rocking curves scans (scanning ω at a fixed 2θ position) were performed to gain insight into the mosaic spread of the film and underlying substrate [88]. This was done by comparing the full-width-at-half-maximum (FWHM) of the rocking curve peaks. The closer the FWHM of the primary film peak is to the FWHM of the substrate peak, the less spread in the

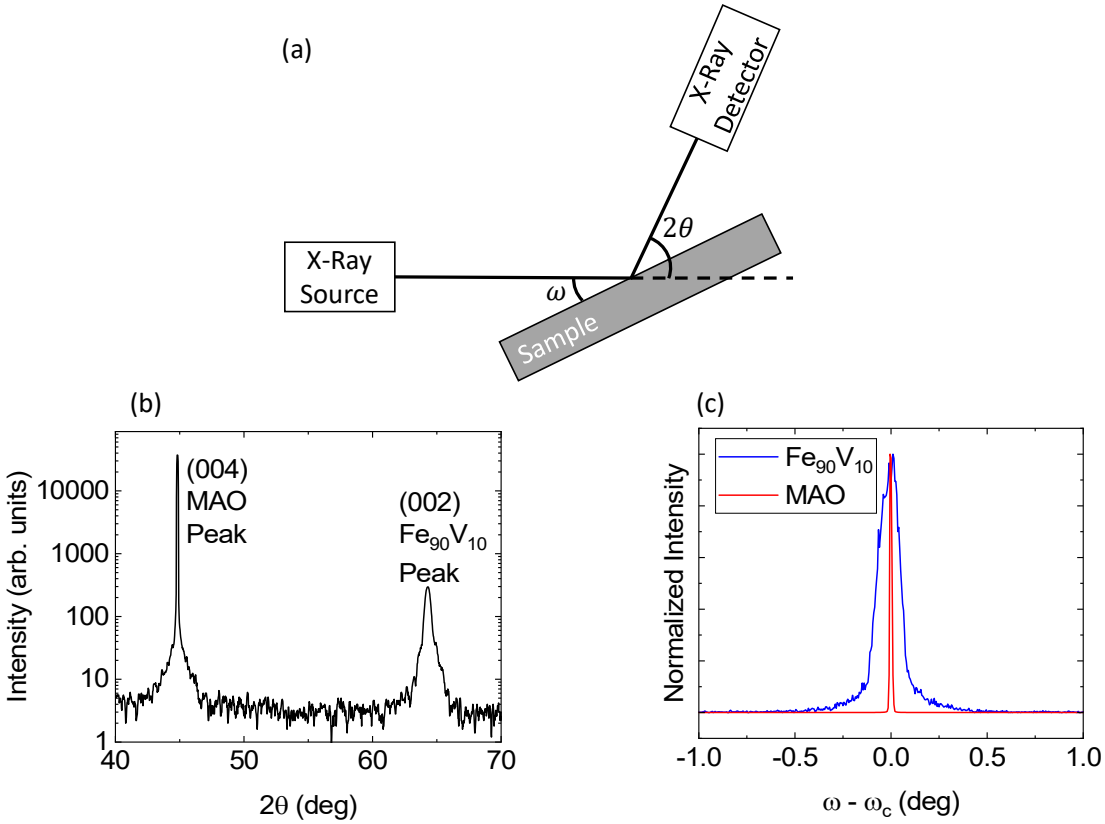


Figure 2.9: (a) XRD geometry showing how the angles ω and θ are defined. (b) Example symmetric $2\theta - \omega$ scan for 25 nm of $Fe_{90}V_{10}$ deposited on a $MgAl_2O_4$ (MAO) substrate. (c) Example rocking curve (ω) scans centered about the peak maximum ω_c for the film peak and substrate peaks.

orientation of the lattice planes of the film. This generally leads to a higher quality epitaxial film. Example rocking curve scans are shown in Fig. 2.9c.

2.5.2 X-Ray Reflectivity

X-ray reflectometry (XRR) is a technique commonly used to study thin film properties in a non-destructive manner [96, 97, 98, 99, 100]. Instead of relying on Bragg diffraction, the incident angle of incoming x-rays is set to a low value, typically $\theta < 5 - 7°$, and the x-rays interact with the various interfaces present within a system. Since some of the x-rays are transmitted and some are reflected at each interface, this results in interference between the different paths. This will result in the measured x-ray intensity fluctuating as the incidence angle changes, commonly referred to as Kiessig fringes. An example of a representative

spectra with Kiessig fringes for a single layer thin film of tungsten (W) deposited on a Si/SiO_2 substrate is shown in Fig. 2.10a.

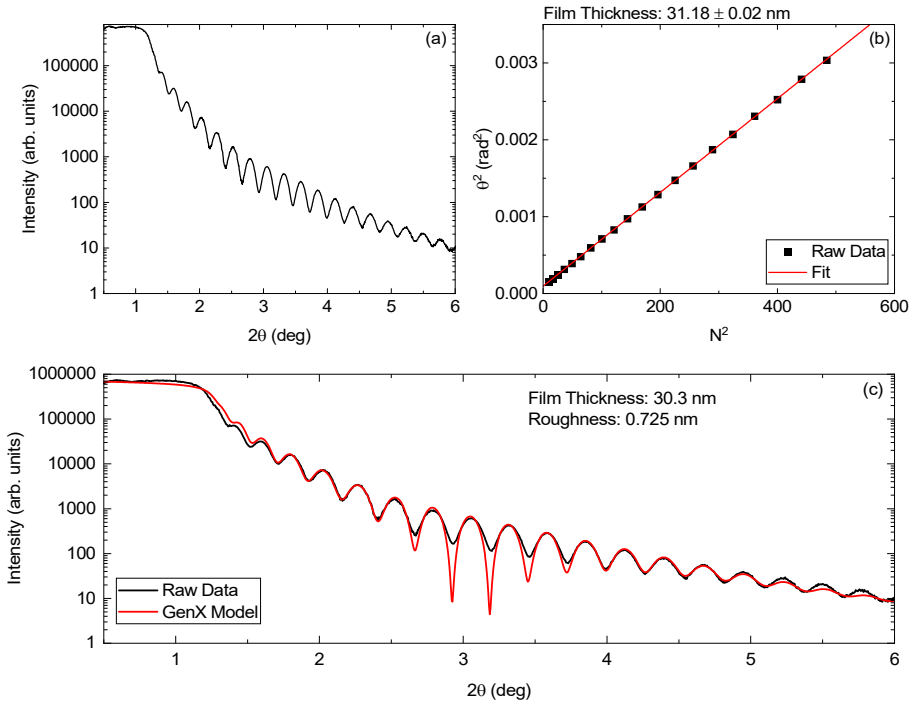


Figure 2.10: (a) Raw XRR signal captured for a single layer film of W deposited on a Si/SiO_2 substrate. (b) Peak position squared (square markers) as a function of peak number squared. The solid line is a fit according to Eq. (2.10) from which the film thickness can be estimated. (c) XRR spectra fit according to a model using the GenX open-source package with extracted film thickness and interfacial roughness.

This technique is commonly used to estimate the density, interfacial roughness, and thickness of individual layers within a thin film. In our lab, we use XRR as a means to accurately measure the thickness of a single layer film and use that known thickness to calibrate the deposition rate of various materials. The film thickness is inversely proportional to the frequency of Kiessig fringes; the thicker a film the more closely spaced the fringes will be, and thus the finer angular resolution required. One can roughly estimate the thickness of a single layer film using

$$\theta_N^2 = \theta_c^2 + \left(\frac{\lambda}{2t}\right)^2 N^2. \tag{2.10}$$

Here θ_N is the angle at which peak N occurs, θ_c is the critical angle at which the incident x-rays begin to penetrate the film (this can be related to the film density, but is typically ignored for our use case), λ is the wavelength of the incident x-rays (typically $\lambda = 0.154$ nm for a Cu Kα source), and t is the film thickness. By performing a linear fit of θ_N^2 vs. N^2, the film thickness can be estimated. This is done in Fig. 2.10b for the spectra in Fig. 2.10a. The interfacial roughness is attributed to how quickly the XRR spectra decays with increasing θ, so the rougher the film interface/surface, the quicker the XRR signal decays.

As more layers are added to a thin film sample, the XRR spectra becomes more complicated [98, 99, 101, 102]. For samples containing more than a single layer film, the above treatment fails to capture either individual or total film thickness. To estimate film thickness, one needs to use software to fit the XRR data to an analytical model. Companies that manufacture XRDs (e.g. Bruker, Panalytical) typically provide modeling software that works specifically with their instruments, but this is not always purchased by the user. In that case, there are alternative open-source packages that can be used. GenX [103] (link) and REFLEX44 [104] (link) are just two of many packages available. As an example, the GenX package was used to fit the XRR spectra shown in Fig. 2.10a. The result of the model along with film thickness and interfacial roughness is shown in Fig. 2.10c.

2.6 Ion Milling

Ion milling can be thought of as the opposite process of sputtering: instead of using energetic ions to deposit material they are used for the removal of material. By bombarding a sample with heavy, fast moving ions, it is possible to slowly remove the material. In our lab this is done using a Kaufmann and Robinson KDC40 ion mill, located at the bottom of one of the sputtering chambers (RHS chamber in Fig. 2.1). A front panel interface (KSC1202) is located at the bottom of the instrument tower and is used to tune various parameters. The main parameters that can be changed include the beam current (number of ions bombarding the target per second), beam voltage (kinetic energy of said ions), and accelerator voltage (tied to the beam voltage, typically 20% of that value). The system by default was set to $I_{beam} = 46$ mA, $V_{beam} = 600$ V, and $V_{accl} = 120$ V, although we have typically used a lower setting as noted below.

This particular ion mill has been used during the photolithography process (see Sec. 2.7) to remove material not covered by photoresist. To use the system, first the chamber must go through a process known as pre-purge, where Ar gas is flown at a fixed rate (typically $3-3.5$ sccm) to reach a pressure of 0.1 mTorr with the chamber valve (the VAT valve located between the main chamber the turbopump) fully open for $5-7$ minutes. Then the sample is milled in short bursts, in the range of $10-15$ s at a time, by first selecting "Enable Discharge," waiting 15 seconds, then "Enable Beam." This can either be done through the front panel on the KSC1202 or via the LabVIEW user interface. The milling is then paused for a longer period of time, approximately 2 minutes, to allow the sample and photoresist to cool. This

is repeated as many times as necessary to remove all of the material of interest. Finally the chamber is run through a post-purge step, with the same Ar flow rate and pressure as the pre-purge, for a total of $7 - 10$ minutes.

Since ion milling is nothing more than throwing energetic ions at a material, there is an inherent transfer of heat to the sample. This can cause problems, particularly with photoresist. If the pause between milling burst is not long enough, it is possible for the photoresist to begin to bake and harden onto the sample, making removal much more difficult. Additionally the heat imparted to the sample could inadvertently alter the properties of the sample. This can be further avoided by reducing the beam current and voltage using a table located in the ion mill manual or increasing the wait time between milling but this will increase the total time required to mill the material. So far, ion mill parameters of $I_{beam} = 23$ mA, $V_{beam} = 400$ V, and $V_{accl} = 80$ V, a duty cycle of 15 s on and 120 s off for a total of mill time of 240 s has shown to be enough to mill approximately 30 nm worth of materials with little to no apparent adverse effect on the photoresist. However, smaller features on the photomask tend to not be well defined or even intact. We have also observed possible indications that the above ion milling parameters may have effectively annealed some samples.

To allow for patterning of smaller features and to suppress undesirable heating of samples, there is still room for improvement in our ion milling process. For instance, it may be beneficial to further reduce the beam voltage and current for a gentler milling process. Another potential remedy, either as an alternative or complement, is to make a custom sample holder that introduces a tilt to the sample plane with respect to the ion beam axis, thereby increasing the efficiency of milling. (Our current setup has the ion beam coming in normal to the sample plane. This may result in poor milling efficiency, where much of the incident ion beam energy simply goes to heating the sample.) When designing a custom sample holder, one will need to keep in mind constraints that come with loading a carrier into the vacuum chamber (e.g. compatibility with the transfer arm). One could also try attaching the substrate to the sample holder in a way that ensures good thermal contact (e.g. by using vacuum grease or some other thermally conductive material). This could help keep the sample at a reasonable temperature as the more massive substrate holder can absorb the heat imparted by the ion beam. All of these are potential fixes that could be investigated in the future.

2.7 Photolithography

Photolithography is the process by which a laterally uniform film is patterned into shapes of various sizes for more specific measurements. For our purposes, this is how we get single and double Hall crosses [35] and ST-FMR devices [105]. Fig. 2.11 shows a step-by-step walkthrough of the photolithography process. Steps (a-d), (f-i), and (k) are done in a clean room environment; step (e) is done in the sputtering chamber, and step (j) is done in a electron beam (e-beam) evaporation chamber. The photolithography for the samples

discussed in Ch. 5 were done courtesy of the students with Prof. Jean J. Heremans' group at Virginia Tech.

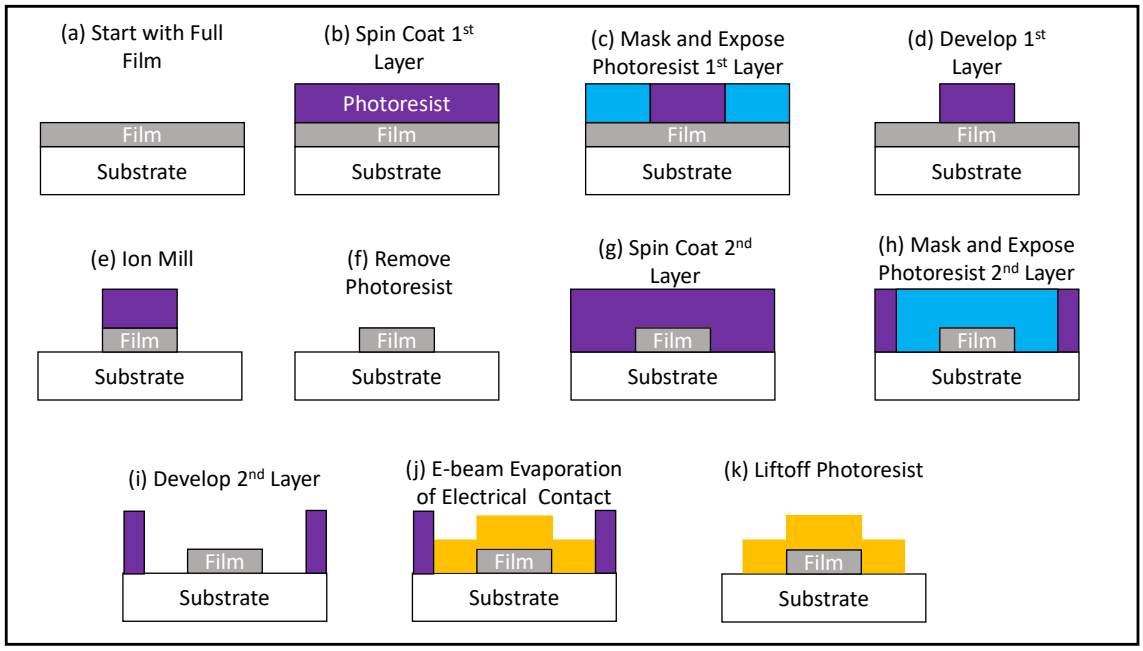


Figure 2.11: Visualization of each step involved in the photolithography process.

We start with a full film deposited on an electrically insulating substrate or on a substrate with an oxide layer. This will help to prevent current passing through the substrate instead of the device when the process is completed (referred to as current shunting). A layer of positive photoresist is then applied to the film and spin coat to ensure an even thickness. A photomask is centered over the film and the film is exposed to UV light for a short period of time (dependent on the photoresist type and thickness, but not more than a few seconds). The UV light changes the properties of the exposed photoresist and hardens it, protecting the film underneath; the unexposed portion is removed during the development step. From here the sample undergoes ion milling (see Sec. 2.6) to remove any unexposed film and then the photoresist is removed using a developer solution.

The next set of steps are similar to the first steps, but negative photoresist is used. The negative photoresist that is not covered by the mask hardens and remains after the developing steps. Additionally, instead of removing material using ion milling, material is deposited, in this case using electron beam (e-beam) evaporation. This deposition of material, here Cr/Au, is used to create the electrical contact pads for measurements.

Chapter 3

Developing a Low Damping Metallic Ferromagnet

The work in this chapter is published as [106]:

David A. Smith, Anish Rai, Youngmin Lim, Timothy Q. Hartnett, Arjun Sapkota, Abhishek Srivastava, Claudia Mewes, Zijian Jiang, Michael Clavel, Mantu K. Hudait, Dwight D. Viehland, Jean J. Heremans, Prasanna V. Balachandran, Tim Mewes, and Satoru Emori, "*Magnetic Damping in Epitaxial Iron Alloyed with Vanadium and Aluminum,*" *Physical Review Applied* **14**, 034042, "Copyright (2020) by American Physical Society."

Parts of this publication were reused in this chapter in largely literal form with alterations to the figures and integration of the supplemental material into the main text of the publication. I contributed to this publication by performing the film growth, x-ray diffraction characterization, and in-plane ferromagnetic resonance measurements. Additionally I performed the data analysis and helped to draft the figures and manuscript. Out-of-plane ferromagnetic resonance measurements were performed by our collaborators in Prof. Tim Mewes' group at the University of Alabama. Density of states calculations were done with the help of Tim Hartnett and Prof. Prasanna Balachandran at the University of Virginia.

3.1 Introduction

The relaxation of magnetization dynamics (e.g., via Gilbert damping) plays important roles in many spintronic applications, including those based on magnetic switching [27, 107], domain wall motion [108, 109], spin wave propagation [11, 110], and superfluid-like spin transport [55, 62]. For devices driven by spin-torque precessional dynamics [26, 27, 37], the critical current density for switching is predicted to scale with the product of the Gilbert damping parameter and the saturation magnetization [107, 111]. Thus, it is desirable to engineer magnetic materials that possess both low damping and low moment for energy-efficient operation. While some electrically insulating magnetic oxides have been considered for certain applications [11, 112, 113], it is essential to engineer low-damping, low-moment *metallic* ferromagnets for robust electrical readout via giant magnetoresistance and tunnel magnetoresistance. Fe is the elemental ferromagnet with the lowest intrinsic Gilbert damping parameter ($\simeq 0.002$) [1, 114], albeit with the highest saturation magnetization ($\simeq 2.0$ T). Recent experiments have reported that Gilbert damping can be further reduced by alloying Fe with Co (also a ferromagnetic element), with $Fe_{75}Co_{25}$ yielding an ultralow intrinsic Gilbert damping parameter of $\simeq 0.001$ [17, 115]. However, $Fe_{75}Co_{25}$ is close to the top of the Slater-Pauling curve, such that its saturation magnetization is greater than that of Fe by approximately 20% [53]. There is thus an unmet need to engineer ferromagnetic alloys that simultaneously exhibit lower damping and lower moment than Fe.

A promising approach towards low-damping, low-moment ferromagnetic metals is to introduce *nonmagnetic* elements into Fe. In addition to diluting the magnetic moment, nonmagnetic elements introduced into Fe could influence the spin-orbit coupling strength ξ, which underlies spin relaxation via orbital and electronic degrees of freedom [2, 15, 116]. Simple

atomic physics suggests that ξ is related to the average atomic number $\langle Z \rangle$ of the alloy so that, conceivably, damping might be lowered by alloying Fe with lighter (lower-Z) elements. Indeed, motivated by the premise of lowering damping through a reduced $\langle Z \rangle$ and presumably ξ, prior experiments have explored Fe thin films alloyed with V [2, 117, 118], Si [119], and Al [120]. However, the experimentally reported damping parameters for these alloys are often a factor of > 2 higher [117, 118, 120] than the theoretically predicted intrinsic Gilbert damping parameter of $\simeq 0.002$ in Fe [3] and do not exhibit a significant dependence on the alloy composition [2, 118, 119]. A possible issue is that the reported damping parameters – obtained from the frequency dependence of ferromagnetic resonance (FMR) linewidth with the film magnetized in-plane – may include contributions from non-Gilbert relaxation induced by inhomogeneity and defects (e.g., two-magnon scattering) [18, 19, 20, 21, 24, 25, 77, 121, 122, 123], which can be affected by the alloying. Therefore, how Gilbert damping in Fe is impacted by alloying with low-Z elements remains an open question.

Here, we investigate the compositional dependence of magnetic relaxation at room temperature in epitaxial thin films of ferromagnetic FeV and FeAl alloys. Both alloys are crystalline bcc solid solutions and hence constitute excellent model systems. We employ two configurations of FMR measurements to gain complementary insights: (1) FMR with samples magnetized in the film plane (similar to the prior experiments) to derive the "effective" Gilbert damping parameter, α_{eff}^{IP}, which is found to include extrinsic magnetic relaxation due to two-magnon scattering, and (2) FMR with samples magnetized perpendicular to the film plane to quantify the intrinsic Gilbert damping parameter, α_{int}, which is free of the two-magnon scattering contribution.

Since Al ($Z = 13$) is a much lighter element than V ($Z = 23$), we might expect lower magnetic relaxation in FeAl than FeV, if the smaller $\langle Z \rangle$ lowers intrinsic Gilbert damping via reduced ξ. Instead, we find a significant decrease in magnetic relaxation by alloying Fe with V – i.e., yielding an intrinsic Gilbert damping parameter of $\simeq 0.001$, on par with the lowest values reported for ferromagnetic metals – whereas damping in FeAl alloys increases with Al content. These experimental results, combined with density functional theory calculations, point to the density of states at the Fermi level $D(E_F)$ as a plausible dominant factor for the lower (higher) Gilbert damping in FeV (FeAl). We thus find that incorporating a low-Z element does not generally lower damping and that, rather, reducing $D(E_F)$ is an effective route for lower damping in Fe alloyed with a nonmagnetic element. Our findings confirm that FeV is an intrinsically ultralow-damping alloy, as theoretically predicted by Mankovsky *et al.* [3], which also possesses a lower saturation magnetization than Fe and FeCo. The combination of low damping and low moment makes FeV a highly promising material for practical metal-based spintronic applications.

3.2 Film Deposition

Epitaxial $Fe_{100-x}V_x$ and $Fe_{100-x}Al_x$ thin films were grown using DC magnetron sputtering on (001)-oriented MgO substrates. Prior to deposition, the substrates were annealed at 600 °C for 2 hours [124]. The base pressure prior to deposition was $< 5 \times 10^{-8}$ Torr, and all films were grown with an Ar pressure of 3 mTorr. Fe and V (Al) 2" targets were DC co-sputtered to deposited $Fe_{100-x}V_x$ ($Fe_{100-x}Al_x$) films at a substrate temperature of 200 °C. By adjusting deposition power, we tuned the deposition rate of each material (calibrated by X-ray reflectivity) to achieve the desired atomic percentage of V (Al). All FeV and FeAl films had a thickness of 25 nm, which is well above the thickness regime where interfacial effects dominate [19, 125]. The FeV (FeAl) films were capped with 3-nm-thick V (Al) deposited at room temperature to protect against oxidation, yielding a film structure of MgO/$Fe_{100-x}V_x$(25nm)/V(3nm) or MgO/$Fe_{100-x}Al_x$(25nm)/Al(3nm).

3.3 Structural Properties

We confirmed the epitaxial bcc structure of our thin films using high resolution X-ray diffraction. 2θ-ω scans show only the (002) peak of the film and the (002) and (004) peaks of the substrate, as shown in Fig 3.1. Rocking curve scans of the film peak show similar full-width-at-half-maximum values of $\simeq 1.3°$ irrespective of composition. The epitaxial relation between bcc Fe and MgO is well known [115, 126]: the bcc film crystal is rotated 45° with respect to the substrate crystal, such that the [100] axis of the film lies parallel to the [110] axis of the substrate. The absence of the (001) film peak indicates that our epitaxial FeV and FeAl films are solid solutions rather than B2-ordered compounds [127].

3.4 Magnetic Relaxation

3.4.1 In-Plane Ferromagnetic Resonance

Many spintronic devices driven by precessional magnetization dynamics are based on in-plane magnetized thin films. The equilibrium magnetization also lies in-plane for soft ferromagnetic thin films dominated by shape anisotropy (i.e., negligible perpendicular magnetic anisotropy), as is the case for our epitaxial FeV and FeAl films. We therefore first discuss FMR results with films magnetized in-plane. The in-plane FMR results further provide a basis for comparison with previous studies [2, 117, 118, 120].

Samples were placed with the film side facing a coplanar waveguide (maximum frequency 50 GHz) and magnetized by an external field H (from a conventional electromagnet, maximum field 1.1 T) along the in-plane [100] and [110] axes of the films. Here, unless otherwise stated,

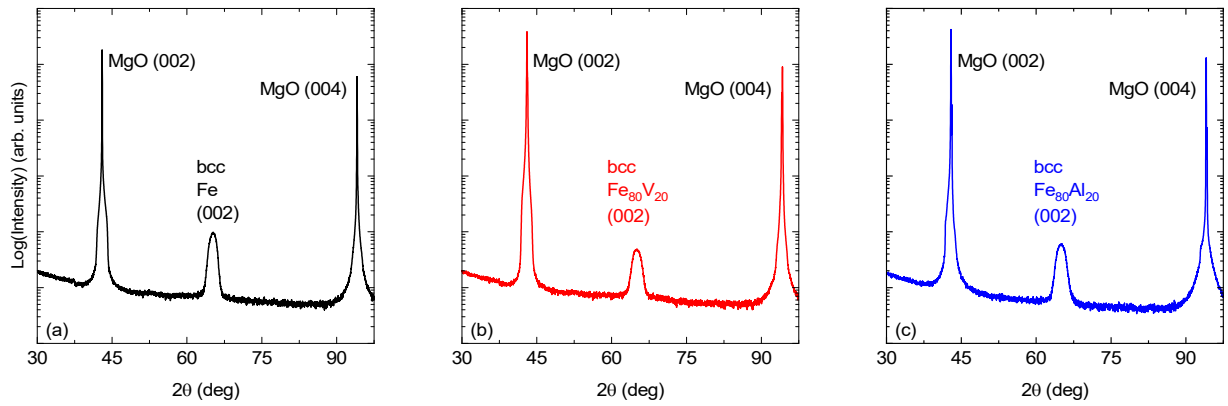


Figure 3.1: 2θ-ω X-ray diffraction scans showing (002) and (004) substrate and (002) film peaks for (a) bcc Fe, (b) $Fe_{80}V_{20}$, and (c) $Fe_{80}Al_{20}$.

we show results for H $\parallel$ [110] of the film. FMR spectra were acquired via field modulation by sweeping H and fixing the microwave excitation frequency.

Exemplary spectra for Fe, $Fe_{80}V_{20}$, and $Fe_{80}Al_{20}$ are shown in Fig. 3.2, where we compare the peak-to-peak linewidths at a microwave excitation frequency of 20 GHz. We see that the linewidth for $Fe_{80}V_{20}$ shows a $\simeq 25\%$ reduction compared to Fe. We further note that the linewidth for the $Fe_{80}V_{20}$ sample here is a factor of $\simeq 2$ narrower than that in previously reported FeV [2]; a possible origin of the narrow linewidth is discussed later in Sec. 3.4.3. In contrast, $Fe_{80}Al_{20}$ shows an enhancement in linewidth over Fe, which is contrary to the expectation of lower magnetic relaxation with a lower average atomic number.

The FMR linewidth is generally governed not only by magnetic relaxation, but also by broadening contributions from magnetic inhomogeneities [77, 128, 129]. To disentangle the magnetic relaxation and inhomogeneous broadening contributions to the linewidth, the typical prescription is to fit the frequency f dependence of linewidth ΔH_{pp}^{IP} with the linear relation

$$\Delta H_{pp}^{IP} = \Delta H_0^{IP} + \frac{h}{g\mu_B\mu_0}\frac{2}{\sqrt{3}}\alpha_{meas}^{IP} f, \tag{3.1}$$

where h is the Planck constant, μ_B is the Bohr magneton, μ_0 is the permeability of free space, and g is the g-factor obtained from the frequency dependence of the resonance field (see Section 3.5) [76]. In Eq. (3.1), the slope is attributed to viscous magnetic damping, captured by the measured damping parameter α_{meas}^{IP}, while the zero-frequency linewidth ΔH_0^{IP} is attributed to inhomogeneous broadening. The fitting with Eq. (3.1) was carried

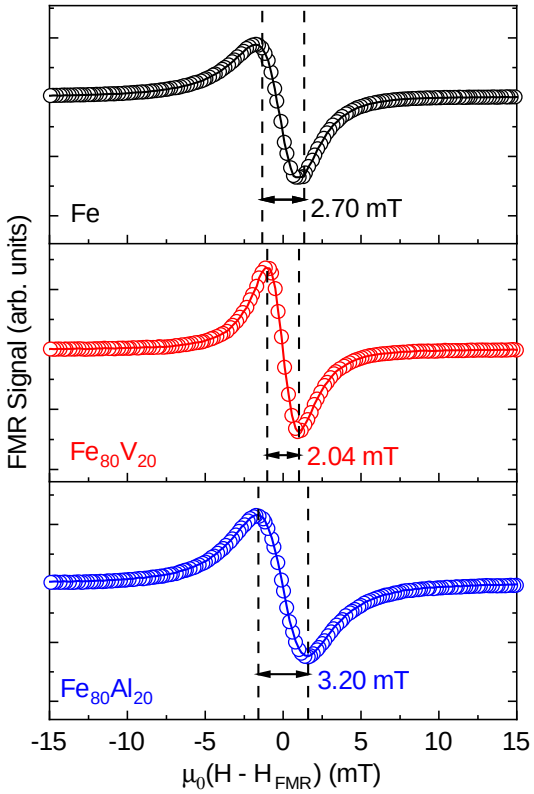


Figure 3.2: FMR spectra at $f = 20$ GHz with the magnetic field H applied in the film plane, fitted using a Lorentzian derivative (solid curve) for Fe, $Fe_{80}V_{20}$, and $Fe_{80}Al_{20}$.

out for $f \geq 10$ GHz, where H was sufficiently large to saturate the films. As is evident from the results in Fig. 3.3, $Fe_{80}V_{20}$ has lower linewidths across all frequencies and a slightly lower slope, i.e., α^{IP}_{meas}. On the other hand, $Fe_{80}Al_{20}$ shows higher linewidths and a higher slope.

The measured viscous damping includes a small contribution from eddy currents, parameterized by α_{eddy} [130], and a contribution due to radiative damping, given by α_{rad} [131]. The contribution from eddy currents to the measured damping parameter is given by

$$\alpha_{eddy} = \frac{1}{12}\frac{g\mu_B}{h}\frac{\mu_0^2 M_s t_F^2}{\rho}, \tag{3.2}$$

where g is the Lande g-factor, μ_B is the Bohr magneton, h is Planck's constant, μ_0 is the permeability of free space, M_s is the saturation magnetization (here equal to the effective magnetization M_{eff}), $t_F = 25$ nm is the film thickness, and ρ is the resistivity. The correction due to radiative damping is given by

$$\alpha_{rad} = \frac{1}{16}\frac{g\mu_B}{\hbar}\frac{\mu_0^2 M_s t_F l}{Z_0 w_{cc}}, \tag{3.3}$$

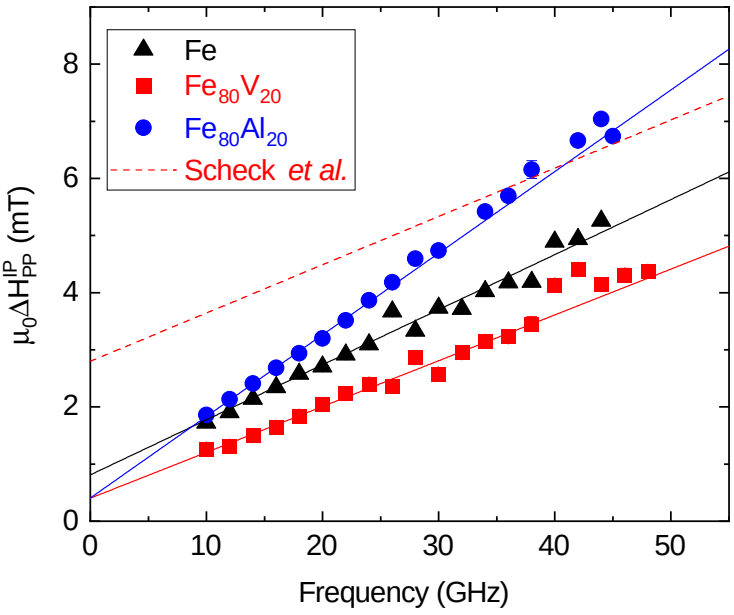


Figure 3.3: FMR linewidths versus microwave frequency for the magnetic field applied within the plane of the film for three distinct alloys. The solid lines are linear fits, described by Eq. (3.1), from which the effective damping parameter and zero frequency linewidth are determined. The dashed line represents the result for $Fe_{73}V_{27}$ from Scheck *et al.* [2]

where $\hbar$ is the reduced Planck's constant, $l \approx 5$ mm is the sample length, $Z_0 = 50\ \Omega$ is the waveguide impedance, and $w_{cc} \approx 280\ \mu$m is the width of the waveguide's central conductor. Together these contributions make up $\simeq 20\%$ of the total α^{IP}_{meas} for pure Fe and decrease in magnitude with increasing V or Al content. We subtract these to obtain the effective in-plane Gilbert damping parameter,

$$\alpha^{IP}_{eff} = \alpha^{IP}_{meas} - \alpha_{eddy} - \alpha_{rad}. \tag{3.4}$$

As shown in Fig. 3.4a, α^{IP}_{eff} remains either invariant or slightly decreases in $Fe_{100-x}V_x$ up to $x = 25$, whereas we observe a monotonic enhancement of α^{IP}_{eff} with Al content in Fig. 3.4b. These results point to lower (higher) damping in FeV (FeAl) and suggest a factor other than the average atomic number governing magnetic relaxation in these alloys. However, such a conclusion assumes that α^{IP}_{eff} is a reliable measure of intrinsic Gilbert damping. In reality, α^{IP}_{eff} may include a contribution from defect-induced two-magnon scattering [18, 19, 20, 21, 24, 77, 121], a well-known non-Gilbert relaxation mechanism in in-plane magnetized epitaxial films [21, 25, 54, 122, 123]. We show in Sec. 3.4.2 that substantial two-magnon scattering is indeed present in our FeV and FeAl alloy thin films.

Although Eq. (3.1) is not necessarily the correct framework for quantifying Gilbert damping in in-plane magnetized thin films, we can gain insight into the quality (homogeneity) of the films from ΔH^{IP}_0. For our samples, $\mu_0 \Delta H^{IP}_0$ is below ≈ 1 mT (see Fig. 3.4c,d), which

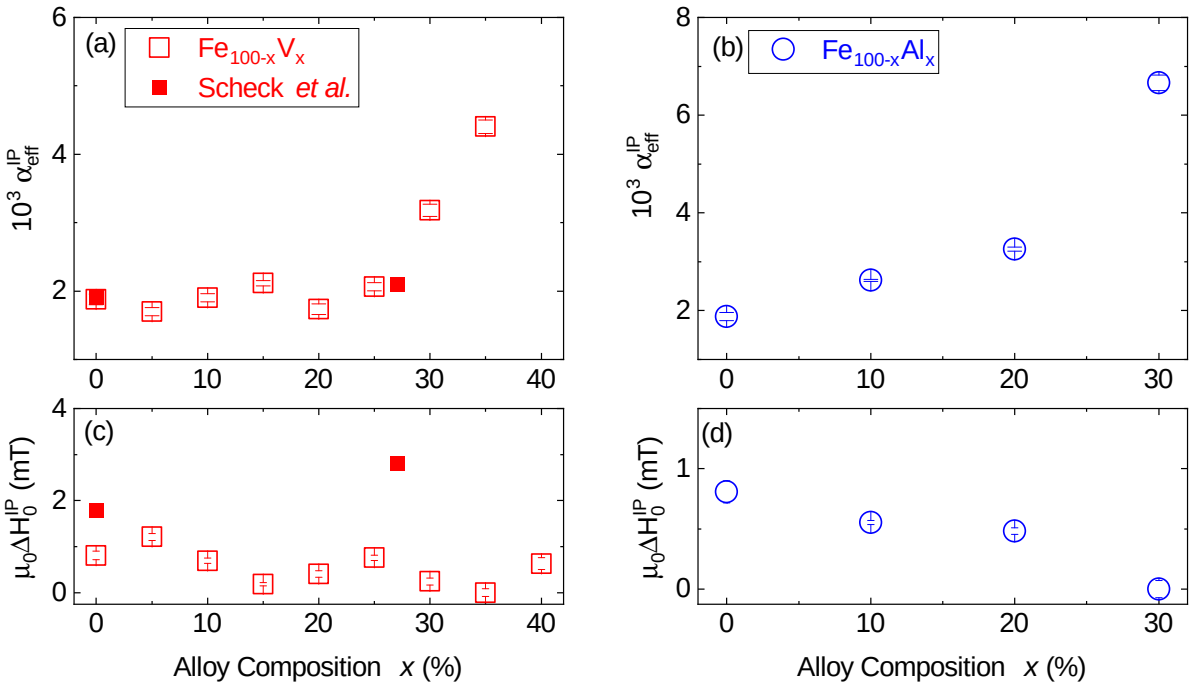


Figure 3.4: The effective damping parameter α_{eff}^{IP} for (a) $Fe_{100-x}V_x$ and (b) $Fe_{100-x}Al_x$ and zero frequency linewidth $\mu_0\Delta H_0^{IP}$ for (c) $Fe_{100-x}V_x$ and (d) $Fe_{100-x}Al_x$, obtained from in-plane FMR. The solid symbols in (a) and (c) represent results reported by Scheck *et al.* [2]

implies higher film quality for our FeV samples than previously reported [2]. For example, $Fe_{73}V_{27}$ in Scheck *et al.* exhibits $\mu_0\Delta H_0^{IP} \simeq 2.8$ mT [2], whereas $Fe_{75}V_{25}$ in our study exhibits $\mu_0\Delta H_0^{IP} \simeq 0.8$ mT. Although α_{eff}^{IP} is comparable between Scheck *et al.* and our study, the small ΔH_0^{IP} leads to overall much narrower linewidths in our FeV films (e.g., as shown in Figs. 3.2 and 3.3). We speculate that the annealing of the MgO substrate prior to film deposition [124], a common practice for molecular beam epitaxy, facilitates high-quality epitaxial film growth and hence small ΔH_0^{IP} even by sputtering.

3.4.2 Out-of-Plane Ferromagnetic Resonance

To quantify intrinsic Gilbert damping, we performed broadband FMR with the film magnetized out-of-plane, which is the configuration that suppresses two-magnon scattering [19, 20, 77, 121]. Samples were placed inside a W-band shorted-waveguide spectrometer (frequency range $70 - 110$ GHz) in a superconducting electromagnet that enabled measurements at fields > 4 T. This high field range is well above the shape anisotropy field of ≤ 2 T for our

films and hence sufficient to completely saturate the film out-of-plane.

The absence of two-magnon scattering in broadband out-of-plane FMR allows us to reliably obtain the measured viscous damping parameter α_{meas}^{OP} by fitting the linear frequency dependence of the linewidth ΔH_{pp}^{OP}, as shown in Fig. 3.5, with

$$\Delta H_{pp}^{OP} = \Delta H_0^{OP} + \frac{h}{g\mu_B\mu_0}\frac{2}{\sqrt{3}}\alpha_{meas}^{OP} f. \tag{3.5}$$

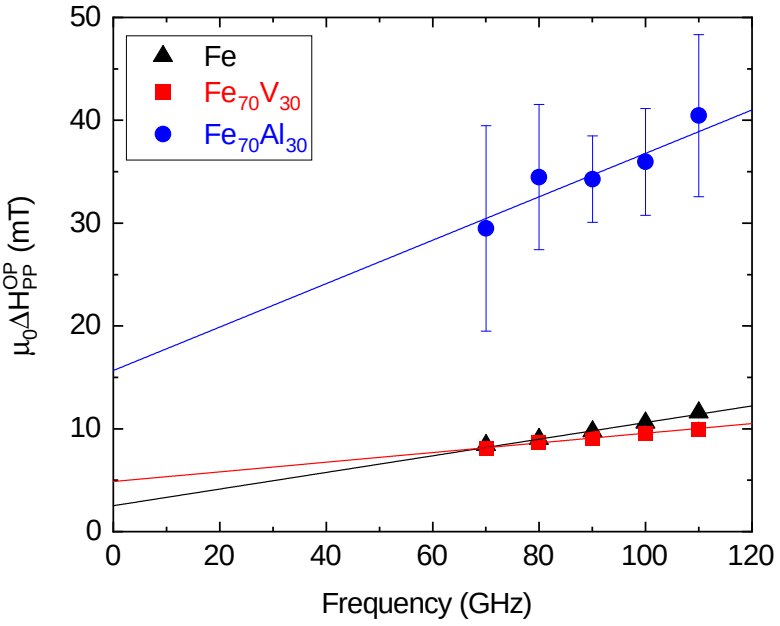


Figure 3.5: FMR linewidths versus applied microwave frequency for the magnetic field applied perpendicular to the plane of the film for three distinct alloys. The line is a linear fit, described by Eq. (3.5), from which the intrinsic Gilbert damping parameter and zero frequency linewidth are determined.

We note that the zero-frequency linewidth for the out-of-plane configuration ΔH_0^{OP} (Fig. 3.6c,d) is systematically greater than that for the in-plane configuration ΔH_0^{IP} (Fig. 3.4c,d). Such a trend of $\Delta H_0^{OP} > \Delta H_0^{IP}$, often seen in epitaxial films [1, 50, 122], may be explained by the stronger contribution of inhomogeneity to the FMR field when the magnetic precessional orbit is circular, as is the case for out-of-plane FMR, compared to the case of the highly elliptical precession in in-plane FMR [128]; however, the detailed mechanisms contributing to the zero-frequency linewidth remain the subject of future work. The larger ΔH_0^{OP} at high V and Al concentrations may be due to broader distributions of anisotropy fields and saturation magnetization, or the presence of a secondary crystal phase that is below the resolution of our X-ray diffraction results.

The absence of two-magnon scattering in out-of-plane FMR allows us to quantify the intrinsic

Gilbert damping parameter,

$$\alpha_{int} = \alpha_{meas}^{OP} - \alpha_{eddy}, \tag{3.6}$$

by again subtracting the eddy current contribution α_{eddy}. Since we utilize a shorted waveguide, the contribution due to radiative damping does not apply.

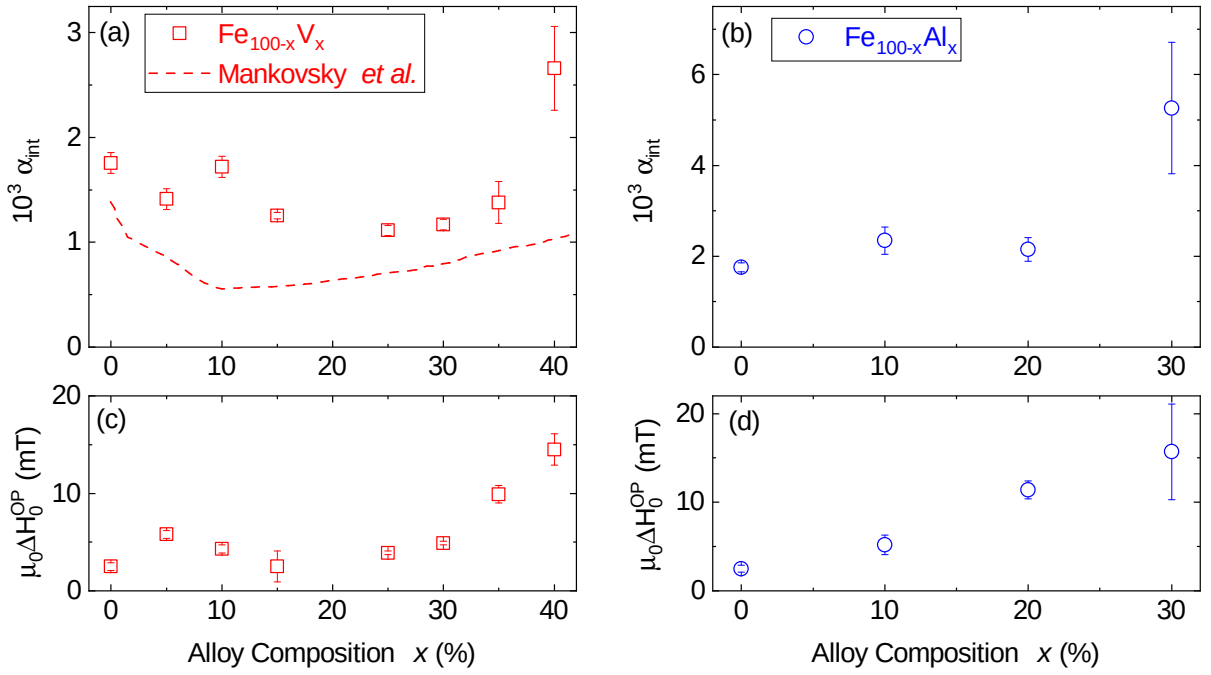


Figure 3.6: The intrinsic Gilbert damping parameter α_{int} for (a) $Fe_{100-x}V_x$ and (b) $Fe_{100-x}Al_x$ and zero frequency linewidth $\mu_0\Delta H_0^{OP}$ for (c) $Fe_{100-x}V_x$ and (d) $Fe_{100-x}Al_x$ obtained from out-of-plane FMR. In (a), the dashed curve shows the predicted intrinsic damping parameter computed by Mankovsky *et al.* [3]

From the compositional dependence of α_{int} as summarized in Fig. 3.6a, a reduction in intrinsic Gilbert damping is evidenced with V alloying. (Note: We were unable to carry out out-of-plane FMR measurements for Fe-V with $x = 20$ [Figs. 3.6a and 3.6c], as the sample had been severely damaged during transit) Our observation is in contrast to the previous experiments on FeV alloys [2, 117, 118] where the reported damping parameters remain > 0.002 and depend weakly on V concentration. In particular, the observed minimum of $\alpha_{int} \simeq 0.001$ at $x \simeq 25 - 30$ is approximately half of the lowest Gilbert damping parameter previously reported for FeV [2] and that of pure Fe [1]. The low α_{int} here is also comparable to the lowest damping parameters reported for ferromagnetic metals, such as $Fe_{75}Co_{25}$ [17, 115] and Heusler compounds [132, 133, 134]. Moreover, the reduced intrinsic damping by alloying Fe

with V is qualitatively consistent with the computational prediction by Mankovsky *et al.* [3], as shown by the curve in Fig. 3.6a. Our experimental finding therefore confirms that FeV is indeed an intrinsically ultralow-damping ferromagnet that possesses a smaller saturation magnetization than Fe.

In contrast to the reduction of α_{int} observed in FeV alloys, FeAl shows an increase in intrinsic damping with increasing Al concentration, as seen in Fig 3.6b. Recalling that Al has an atomic number of $Z = 13$ that is lower than $Z = 23$ for V, this trend clashes with the expectation that lower $\langle Z \rangle$ reduces the intrinsic Gilbert damping through a reduction of the atomic spin-orbit coupling. Thus, we are required to consider an alternative mechanism to explain the higher (lower) damping in FeAl (FeV), which we discuss further in Section 3.6.

3.4.3 Magnetic Relaxation: Practical Considerations

For both FeV and FeAl alloys, α_{int} derived from out-of-plane FMR (Fig. 3.6a,b) is consistently lower than α_{eff}^{IP} derived from in-plane FMR (Fig. 3.4a,b). This discrepancy between α_{int} and α_{eff}^{IP} implies a two-magnon scattering contribution to magnetic relaxation in the in-plane configuration (Fig. 3.4a,b). For many applications, including spin-torque oscillators and magnonic devices, it is crucial to minimize magnetic relaxation in in-plane magnetized thin films. While the in-plane magnetic relaxation ($\alpha_{eff}^{IP} \simeq 0.002$) is already quite low for the FeV alloys shown here, the low intrinsic Gilbert damping ($\alpha_{int} \simeq 0.001$) points to the possibility of even lower relaxation and narrower FMR linewidths by minimizing two-magnon scattering and inhomogeneous linewidth broadening. Such ultralow magnetic relaxation in FeV alloy thin films may be achieved by optimizing structural properties through growth conditions [115] or seed layer engineering [135].

While ultralow intrinsic Gilbert damping values have been confirmed in high-quality epitaxial FeV, it would be desirable for device integration to understand how magnetic relaxation in FeV would be impacted by the presence of grain boundaries, i.e. in polycrystalline thin films. Reports on polycrystalline FeCo [17, 135] suggest intrinsic damping values comparable to those seen in epitaxial FeCo [115]. While beyond the scope of this study, our future work will explore the possibility of low damping in polycrystalline FeV thin films.

3.5 Spectroscopic Parameters

For the determination of material parameters, in-plane FMR measurements were carried out for each sample, from $f = 10$ GHz up to the instrument limit of $f = 50$ GHz along the film [100] and [110] axes at room temperature. The FMR resonance fields versus frequency along the two directions are shown in Fig. 3.7. We note that the applied field necessary to excite FMR dynamics is lower along the [110] direction, indicating the film's easy axis is oriented parallel to that axis. We can extract information about each sample using the

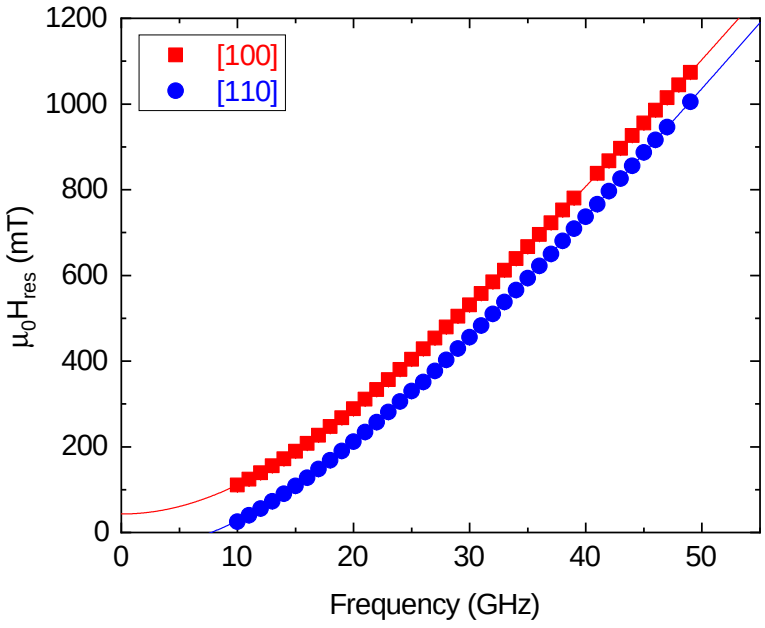


Figure 3.7: FMR resonance field vs frequency for $Fe_{75}V_{25}$ with the magnetic field applied along the film [100] (red circles) and [110] (blue squares) axes. The solid lines are fits according to Eq. (3.7).

Kittel equation [72]

$$f = \frac{g\mu_B\mu_0}{h}\sqrt{(H_{res} + H_k\cos(4\phi))(H_{res} + \frac{1}{4}H_k(3+\cos(4\phi)) + M_{eff})}, \tag{3.7}$$

where g is the Landè g-factor, μ_B is the Bohr magneton, μ_0 is the permeability of free space, h is the Planck constant, H_{res} is the resonance field, H_k is the in-plane cubic anisotropy, M_{eff} is the effective magnetization, and ϕ is the angle between the applied field and the film [110] axis. For each sample, we use g, M_{eff}, and H_k as gloabl fitting parameters for both sets of data in order to constrain the fit. Out-of-plane FMR measurements were carried out from $f = 70$ GHz to $f = 110$ GHz at room temperature. We extracted g and M_{eff} for the out-of-plane configuration using the Kittel equation of the form

$$f = \frac{g\mu_B\mu_0}{h}\left(H_{res} - M_{eff}\right). \tag{3.8}$$

The results presented so far reveal that magnetic relaxation is reduced by alloying Fe with V, whereas it is increased by alloying Fe with Al. On the other hand, FeV and FeAl alloys exhibit similar compositional dependence of the spectroscopic parameters: effective magnetization M_{eff} (here, equivalent to saturation magnetization M_s), magnetocrystalline anisotropy field

H_k, and the g-factor gAs shown in Fig. 3.8a, there is a systematic reduction in M_{eff} with increasing concentration of V and Al. We also note in Fig. 3.8b a gradual reduction in magnitude of the in-plane cubic anisotropy. Both of these trends are expected as magnetic Fe atoms are replaced with nonmagnetic atoms of V and Al. The reduction of M_{eff} by $\simeq 20\%$ in the ultralow-damping $Fe_{100-x}V_x$ alloys with $x = 25 - 30$, compared to pure Fe, is of particular practical interest. The saturation magnetization of these FeV alloys is on par with commonly used soft ferromagnetic alloys (e.g., $Ni_{80}Fe_{20}$ [52], CoFeB [136]), but the damping parameter of FeV is several times lower. Further, while FeV and FeCo in the optimal composition window show similarly low intrinsic damping parameters, FeV provides the advantage of lower moment. With the product $\alpha_{int}M_{eff}$ approximately proportional to the critical current density to excite precessional dynamics by spin torque [107, 111], FeV is expected to be a superior material platform for low-power spintronic devices.

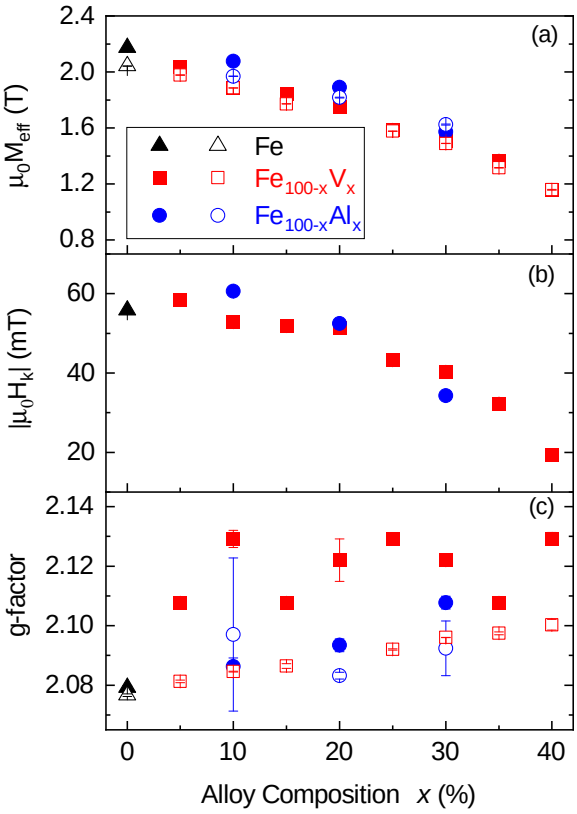


Figure 3.8: (a) Effective magnetization, (b) magnitude of in-plane cubic anisotropy field, and (c) g-factor versus V and Al concentration. The solid (open) markers represent data from in-plane (out-of-plane) measurements.

The g-factor $g = 2(1 + \mu_L/\mu_S)$ is related to the orbital moment μ_L and spin moment μ_S; the deviation from the spin-only value of $g = 2.00$ provides insight into the strength of

spin-orbit coupling ξ [137]. As seen in Fig. 3.8c, g increases by $1-2\%$ with both V and Al alloying, which suggests that ξ increases slightly with the addition of these low-Z elements. This finding verifies that $\langle Z \rangle$ is not necessarily a good predictor of ξ in a solid. Moreover, the higher g for FeV is inconsistent with the scenario for lower damping linked to a reduced spin-orbit coupling. Thus, spin-orbit coupling alone cannot explain the observed behavior of Gilbert damping in Fe alloyed with low-Z elements.

3.6 Discussion

In contrast to what has been suggested by prior experimental studies [2, 117, 118, 119, 120], we have shown that the reduction of average atomic number by alloying with a light element (e.g., Al in this case) does not generally lower the intrinsic Gilbert damping of Fe. A possible source for the qualitatively distinct dependencies of damping on V and Al contents is the density of states at the Fermi level, $D(E_F)$: it has been predicted theoretically that the intrinsic Gilbert damping parameter is reduced with decreasing $D(E_F)$, since $D(E_F)$ governs the availability of states for spin-polarized electrons to scatter into [3, 14, 15, 16, 138]. Such a correlation between lower damping and smaller $D(E_F)$ has been reported by recent experiments on FeCo alloys [52, 115], FeRh alloys [127], CoNi alloys [139], and Heusler compounds [132, 134, 140]. The similarity in the predicted composition dependence of the Gilbert damping parameter for FeCo and FeV [3] suggests that the low damping of FeV may be correlated with reduced $D(E_F)$. However, no prior experiment has corroborated this correlation for FeV or other alloys of Fe and light elements.

We therefore examine whether the lower (higher) damping in FeV (FeAl) compared to Fe can be qualitatively explained by $D(E_F)$. Utilizing the Quantum ESPRESSO [141] package to perform density functional theory calculations [142, 143, 144, 145, 146], we calculated the density of states for Fe, $Fe_{81.25}V_{18.75}$, and $Fe_{81.25}Al_{18.75}$. It should be recalled that although FeV and FeAl films measured experimentally here are single-crystalline, they are solid solutions in which V or Al atoms replace Fe atoms at arbitrary bcc lattice sites. Therefore, for each of the binary alloys, we computed 6 distinct atomic configurations in a $2\times2\times2$ supercell, as shown in Fig 3.9. The spin-split density of states for each unique atomic configuration is indicated by a curve in Fig. 3.10. Here, $D(E_F)$ is the sum of the states for the spin-up and spin-down bands, averaged over results from the 6 distinct atomic configurations.

As summarized in Fig. 3.10 and Table 3.1, FeV has a smaller $D(E_F)$ than Fe, whereas FeAl has a larger $D(E_F)$. These calculation results confirm a smaller (larger) availability of states for spin-polarized electrons to scatter into in FeV (FeAl), qualitatively consistent with the lower (higher) intrinsic Gilbert damping in FeV (FeAl).

We remark that this correlation between damping and $D(E_F)$ is known to hold particularly well in the limit of low electronic scattering rates τ^{-1}, where intraband scattering dominates [15, 16]. Gilmore *et al.* [15] have pointed out that at sufficiently high electronic scattering

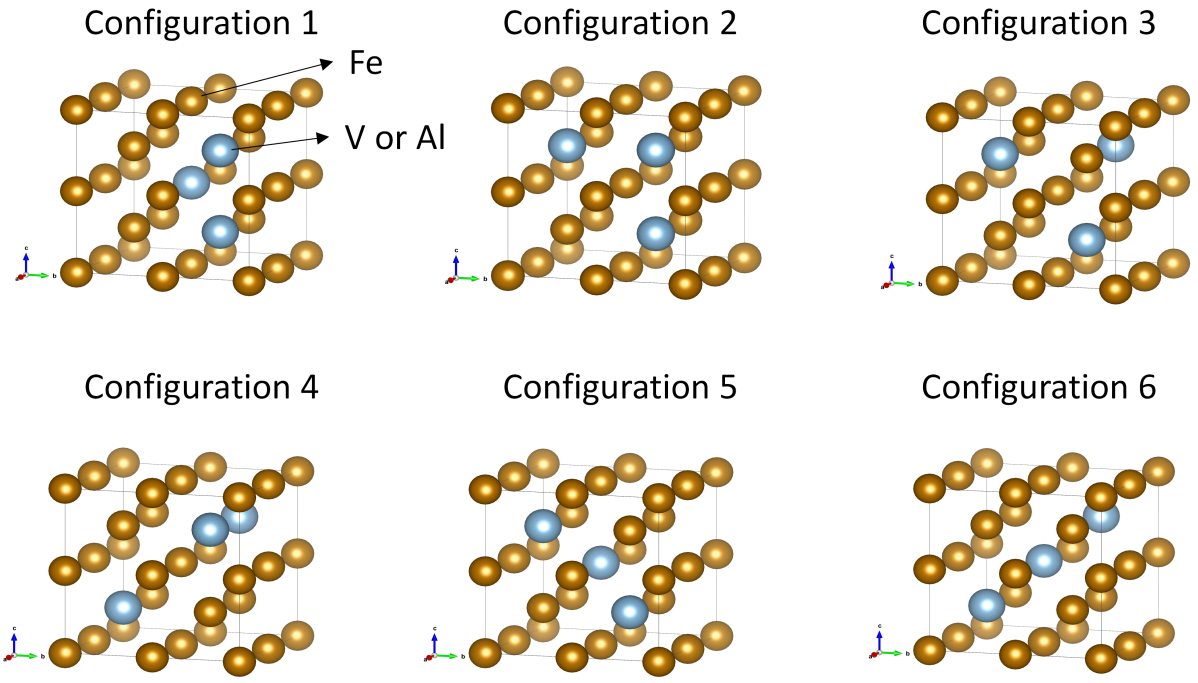


Figure 3.9: The six unique atomic configurations from the supercell program for mimicking the $Fe_{81.25}V_{18.75}$ or $Fe_{81.25}Al_{18.75}$ solid solution.

rates, i.e., when $\hbar\tau^{-1}$ is large enough that interband scattering is substantial, the simple correlation between the strength of Gilbert damping and $D(E_F)$ breaks down. It is unclear whether our FeV and FeAl alloy films at room temperature are in the intraband- or interband-dominated regime. Schoen *et al.* have argued that polycrystalline FeCo alloy films – with higher degree of structural disorder and likely higher electronic scattering rates than our epitaxial films – at room temperature are still well within the intraband-dominated regime [17]. On the other hand, a recent temperature-dependent study on epitaxial Fe suggests coexistence of the intraband and interband contributions at room temperature [1]. A consistent explanation for the observed room-temperature intrinsic damping in our alloy films is that the interband contribution depends weakly on alloy composition; it appears reasonable to conclude that $D(E_F)$, primarily through the intraband contribution, governs the difference in intrinsic Gilbert damping among Fe, FeV, and FeAl.

3.7 Summary

We have experimentally investigated magnetic relaxation in epitaxial thin films of Fe alloyed with low-atomic-number nonmagnetic elements V and Al. We observe a reduction in the intrinsic Gilbert damping parameter to $\alpha_{int} \simeq 0.001$ in FeV films, comparable to the lowest-

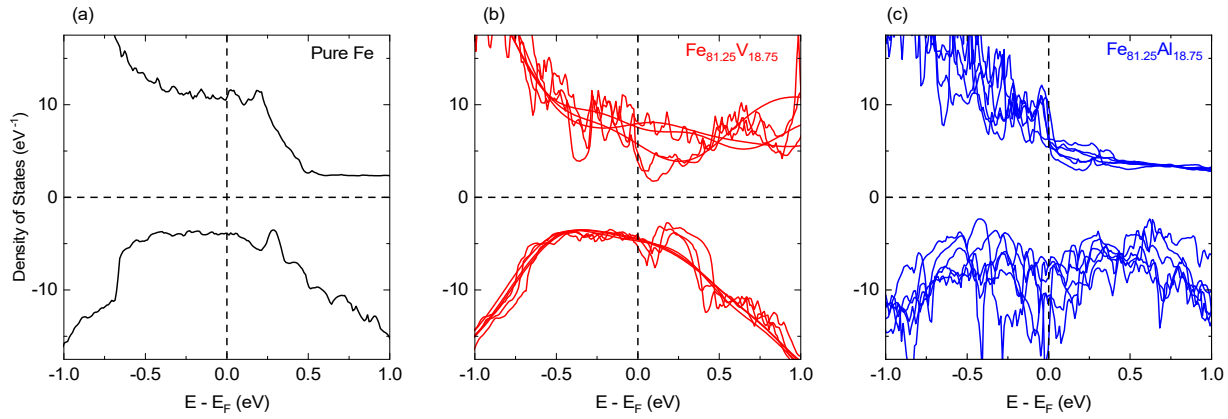


Figure 3.10: Calculated spin-up (positive) and spin-down (negative) density of states for (a) Fe, (b) $Fe_{81.25}V_{18.75}$, and (c) $Fe_{81.25}Al_{18.75}$. Results from the 6 distinct atomic configurations are show in (b,c); the average density of states at E_F for $Fe_{81.25}V_{18.75}$ and $Fe_{81.25}Al_{18.75}$ are shown in Table 1.

damping ferromagnetic metals reported to date. In contrast, an increase in damping is observed with the addition of Al, demonstrating that a smaller average atomic number does not necessarily lower intrinsic damping in an alloy. Furthermore, our results on FeV and FeAl cannot be explained by the change in spin-orbit coupling through alloying. Instead, we conclude that the density of states at the Fermi level plays a larger role in determining the magnitude of damping in Fe alloyed with lighter elements. Our work also confirms FeV alloys as promising ultralow-damping, low-moment metallic materials for practical power-efficient spin-torque devices.

	# Spin-Up States (eV^{-1}) at E_F	# Spin-Down States (eV^{-1}) at E_F
Fe	10.9	3.44
$Fe_{81.25}V_{18.75}$	6.28 ± 1.80	4.61 ± 0.43
$Fe_{81.25}Al_{18.75}$	6.81 ± 1.58	10.20 ± 3.03

Table 3.1: Number of spin-up and spin-down states at E_F. For $Fe_{81.25}V_{18.75}$ and $Fe_{81.25}Al_{18.75}$, the average and standard deviation of values for the 6 distinct atomic configurations (cf. Fig. 3.9) are shown.

Chapter 4

Superfluid-like Spin Transport as a Train of Domain Walls

This work in this chapter is published as [147]:

David A. Smith, So Takei, Bella Brann, Lia Compton, Fernando Ramos-Diaz, Matthew J. Simmers, and Satoru Emori, "*Diffusive and Fluidlike Motion of Homochiral Domain Walls in Easy-Plane Magnetic Strips,*" *Physical Review Applied* **16**, 054002, "Copyright (2021) by American Physical Society."

Parts of this publication were reused for this chapter largely in literal form with modification to the figures and integration of the appendices into the main text of the publication. I contributed to this publication by performing the micromagnetic simulations and data analysis, construction of the figures, and drafting of the manuscript. Details of the Mumax^3 code and data extraction from the output files can be found in App. A. The full details of the analytical model, derived by our collaborator Prof. So Takei at Queens College, can be found in the full supplemental material online.

4.1 Introduction

Transport of spin information via magnetization dynamics is a key area of rapid development within spintronics [148]. To date, much work on micron-scale spin transport has focused on using diffusive spin waves [48, 49]. The magnetization precession cone angle in diffusive spin waves is typically $\ll 10°$, and the associated spin flow decays exponentially with decay length inversely proportional to the Gilbert damping parameter α, as illustrated in Fig. 4.1a. As a result, efficient spin transport at or beyond the micron scale has been difficult to attain, particularly in typical metallic ferromagnets with $\alpha > 10^{-3}$ that are compatible with industrial device fabrication.

An alternative method to achieving long distance spin transport in the form of spin superfluidity [55, 61, 62, 67, 149, 150, 151] has gathered interest in recent years. In spin superfluidity the magnetization undergoes easy-plane precession with a cone angle of $\approx 90°$, driven by a current-induced spin-transfer torque [27, 28, 152]. The resulting precessional dynamics propagates along the ferromagnet in a spiraling manner, as illustrated in Fig. 4.1b, and is protected from unwinding by the strong easy-plane anisotropy preventing phase slips [153]. While true superfluidity (i.e. lossless spin transport) is not possible as a result of ever-present viscous Gilbert damping, this unique form of magnetization dynamics creates a spin flow that decays linearly or algebraically with distance. This easy-plane superfluid-*like* spin transport – also called "dissipative exchange flow" [150] or "exchange-mediated spin transport" [151] – has been proposed as a means of spin information transport even in metallic ferromagnets [58, 59, 149, 150, 154] with moderate damping parameters.

Halperin and Hohenberg originally proposed a model to view easy-plane precessional magnetization dynamics from a hydrodynamic perspective [66], in a manner that is analogous to that of superfluidity. This hydrodynamic perspective has been used to analyze easy-plane spin transport in several studies [58, 59, 60, 150]. However, these studies have focused on

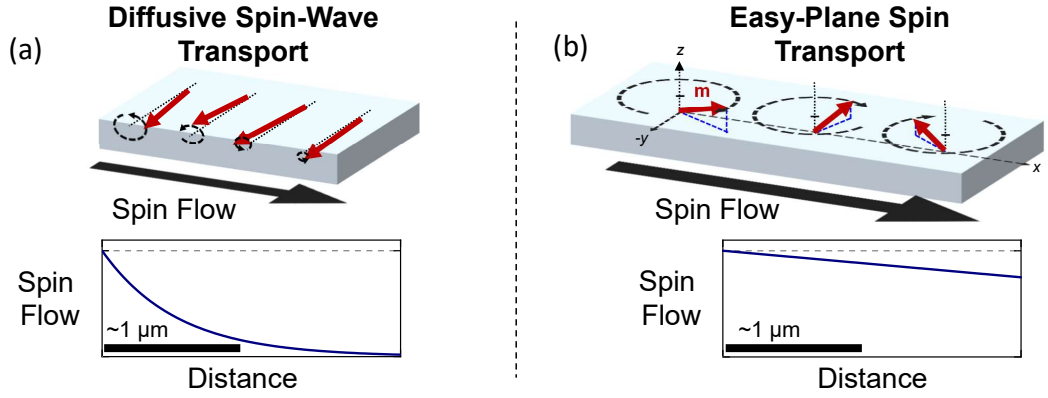


Figure 4.1: (a) Illustration of small angle precession constituting diffusive spin waves and exponential decay of spin flow. (b) Easy-plane precession constituting superfluid-like spin transport and associated linear decay of spin flow.

the regime that requires higher drive current densities, J_c. The requirement of high current densities ($J_c > 1 \times 10^{12}$ A/m^2) poses potential problems in the form of Joule heating as well as electromigration altering material properties. While studies have investigated the effects of in-plane magnetocrystalline anisotropy [150], Gilbert damping [59], and void defects [58, 60], how the easy-plane spin transport behaves at lower drive current densities, closer to the range of experimental feasibility, has yet to be answered.

In this study, we have performed micromagnetic simulations of easy-plane spin transport in synthetic antiferromagnet nanostrips, focusing on the low drive regime. The synthetic antiferromagnet material parameters mimic those of experimentally measured, metallic ferromagnets. Instead of taking the conventional approach from a hydrodynamic perspective, we study the dynamics as a train of interacting, homochiral domain walls (DWs) [155]. We find that at low drive current densities J_c, the DWs can be pinned by a notch defect. We observe the transition from diffusive motion to fluid-like motion as J_c is increased and the DW density increases. The dynamics of the DW train converges to that of the established hydrodynamic behavior when the DW spacing becomes comparable to the DW width at $J_c \simeq 5 \times 10^{11}$ A/m^2. In this fluid-like regime, the train of DWs are unimpeded by the notch defect. Our results suggest that even at moderately low J_c and with deep notch defects, it is feasible to achieve easy-plane spin transport in a metallic ferromagnetic system.

4.2 Simulation Details

We have simulated easy-plane spin transport – i.e., motion of a train of spiraling homochiral transverse Néel DWs – in magnetic nanostrips using Mumax[3], an open-source GPU accelerated micromagnetic simulation package [156]. In single-layer ferromagnetic strips (see Sec. 4.4), the moving transverse DWs are unstable and transform into vortex DWs [109, 157], which effectively constitute phase slips and breakdown of coherent easy-plane spin transport. The result of micromagnetic simulations in single layer strips are discussed in Sec. 4.4. We instead focus here on simulations of synthetic antiferromagnetic strips, which are composed of two ferromagnetic layers coupled in an antiparallel manner [68]. The interlayer-coupled magnetic moments reduce dipolar fields at the strip edges via flux closure and stabilize transverse Néel DWs [158]. Thus, the formation of vortices are suppressed and easy-plane spin transport, carried by spiraling transverse DWs, remains far more stable in synthetic antiferromagnets than in single-layer ferromagnets. The enhanced stability of easy-plane spin transport in synthetic antiferromagnets has been previously reported in a micromagnetic study by Skarsvåg *et al.* [67].

A depiction of our simulation set-up is shown in Fig. 4.2a. The dimensions of an individual ferromagnetic layer are 2000 nm × 100 nm × 2 nm with a cell size of 2.5 nm × 2.5 nm × 2 nm. The two layers are coupled using an RKKY interaction with strength $J_{RKKY} = -1$ mJ/m^2. The initial magnetization states lie completely in plane and are parallel to the long axis of the nanostrip (i.e. $\vec{m}_i \parallel \pm\hat{x}$). To simulate the interaction of easy-plane spin transport with defects, a pair of symmetric, triangular notches with lateral dimensions 60 nm × 30 nm were introduced at the midpoint of the nanostrip ($x = 1000$ nm).

The material parameters of our nanostrips were chosen to match those of experimentally measured, 2 nm thick polycrystalline $Fe_{80}V_{20}$ (see Sec. 4.3 for determination of material parameters): saturation magnetization $M_{sat} = 720$ kA/m, in-plane magnetocrystalline anisotropy $K = 0$ J/m^3, and Gilbert damping parameter $\alpha = 0.006$. The exchange constant was set to $A_{ex} = 20$ pJ/m, in line with typical literature values for Fe [159, 160]. At each end of the nanostrip in a 100 nm × 100 nm region, we introduce an enhancement to the Gilbert damping parameter, $\alpha' = 0.015$, to simulate the effects of spin pumping into and out of the nanostrip [161]. The total Gilbert damping parameter in these end regions is $\alpha_{total} = \alpha + \alpha'$. All simulations were performed at zero temperature.

In order to excite dynamics, an out-of-plane spin polarized charge current density J_c was applied to the injection region, as shown in Fig. 4.2a. The spin polarized charge current imparts an out-of-plane spin-transfer torque [27] $\vec{\tau}_{ST} \sim \vec{m} \times (\vec{s} \times \vec{m})$, where $\vec{s} \parallel \hat{z}$ is the spin polarization, on the magnetization $\vec{m}$. This excitation is similar to that in current-perpendicular-to-plane perpendicularly magnetized spin valves [28, 152]. The spin-transfer torque was set to act directly on the top ferromagnetic layer only. This was done to be consistent with previous studies [162, 163] showing that injected spins orthogonal to $\vec{m}$ in a metallic ferromagnet are absorbed within the first ≈1 nm. The spin polarization of the

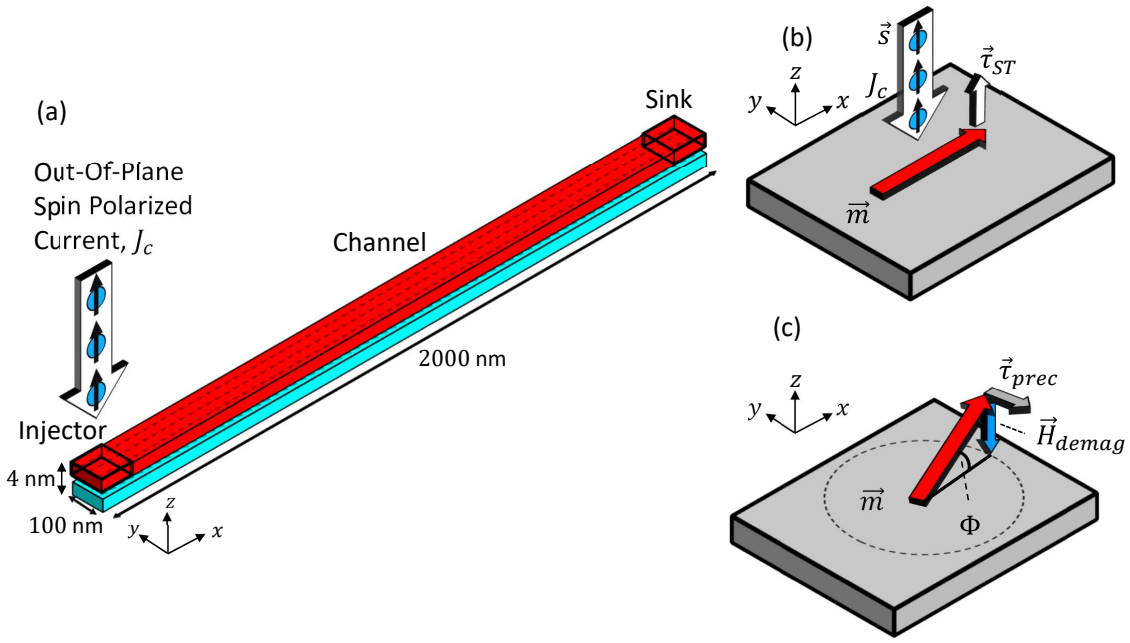


Figure 4.2: (a) Micromagnetic simulation setup of the synthetic antiferromagnet nanostrip. (b) The resulting torque generated by the out-of-plane spin-polarized electric current J_c, lifting the magnetization out of the plane in the injector region. (c) The out-of-plane component of the magnetization creates a demagnetizing field, generating a precessional torque that drives easy-plane precession.

current was set to $P = 0.5$.

The spin-transfer torque creates a finite out-of-plane component of the magnetization, m_z, with an out-of-plane canting angle Φ, shown in Fig. 4.2b. The out-of-plane component m_z generates a demagnetizing field $\vec{H}_{demag}$ and a precessional torque $\vec{\tau}_{prec} \sim -\vec{m} \times \vec{H}_{demag}$, as depicted in Fig. 4.2c. The torque then causes $\vec{m}$ to rotate in a constant direction (e.g. clockwise in the present case) and thus dictates the chirality of the resulting DWs. The easy-plane magnetization dynamics then propagates along the nanostrip, away from the injector, via exchange coupling.

4.3 Experimental Determination of Material Parameters

The material parameter chosen for our micromagnetic simulations were similar to those of experimentally measured polycrystalline $Fe_{80}V_{20}$ thin films. We deposited these films using magnetron sputtering with base pressure $< 5 \times 10^{-8}$ Torr. The films were deposited on Si/SiO_2 substrates at room temperature with an Ar pressure of 3 mTorr. A Ti/Cu seed layer was initially deposited to promote good adhesion to the substrate and a Ti capping layer was deposited to protect against film oxidation. Fe and V were co-sputtered from two separate targets. All material deposition rates were calibrated using x-ray reflectivity. The sample stack structure is subs./Ti(3)/Cu(3)/$Fe_{80}V_{20}$(2)/Ti(3) where the values in the parentheses are layer thicknesses in nm.

To determine the magnetic properties of our films, we utilized broadband ferromagnetic resonance (FMR). The thin film sample was placed face-down on a coplanar waveguide with a maximum frequency of 36 GHz and magnetized by an external field H generated by a conventional electromagnet. The FMR spectra was acquired by fixing the microwave frequency and sweeping the magnetic field through the resonance condition. The resulting spectra is then fit with a Lorentzian derivative, from which the resonance field H_{res} and half-width-at-half-maximum (HWHM) linewidth ΔH are determined for each frequency.

The resonance field as a function of microwave frequency is plotted in Fig. 4.3 and fit using the standard Kittel equation for in-plane magnetized polycrystalline thin films [72]

$$f = \mu_0 \gamma' \sqrt{H_{res}(H_{res} + M_{eff})}, \tag{4.1}$$

where $\gamma' = \gamma/2\pi$ is the reduced gyromagnetic ratio and M_{eff} is the effective magnetization (here equal to the saturation magnetization M_{sat}). From this fit we determine that $\gamma' = 30.5$ GHz/T and $M_{eff} = 720$ kA/m.

The HWHM linewidth, plotted in Fig. 4.4, gives insight into the magnetic relaxation of a film. By using the linear equation [128]

$$\Delta H = \Delta H_0 + \frac{\alpha}{\mu_0 \gamma'} f, \tag{4.2}$$

one can determine the Gilbert damping parameter α and zero frequency linewidth ΔH_0. From the linear fit we deduce $\alpha = 0.006$ in our 2 nm FeV film.

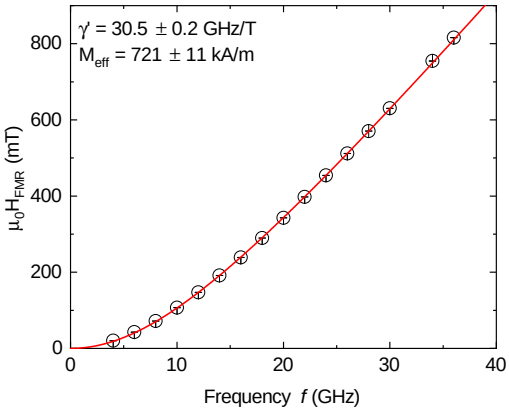


Figure 4.3: FMR resonance field as a function of microwave frequency. The solid line is a fit according to Eq. 4.1.

4.4 Easy-plane Precession Dynamics in Single Layer Systems

We focused on simulating easy-plane spin transport in synthetic antiferromagnets as opposed to single layer nanostrips. In synthetic antiferromagnets, the long-range dipolar fields from one ferromagnetic layer are compensated by an adjacent second layer. This has the effect of stabilizing transverse Néel DWs and suppressing Walker breakdown [158]. Micromagnetic snapshots of phase slips via vortex formation (similar to Walker breakdown) in single layer systems are shown in Fig. 4.5a and Fig. 4.5b for the perfect and notched nanostrips, respectively.

In the perfect nanostrip, a vortex core begins to form at the end of the nanostrip within a DW. The vortex core then propagates against the flow of DWs. In the notched nanostrips, multiple vortex cores begin to form at the edges of the nanostrip, similar to the perfect nanostrip. The vortex fully forms off the tip of the notch defect (see Supplemental Video 10). These vortices stay in the nanostrip until they encounter a vortex with opposite core polarity upon which the pair is annihilated.

The difference between the single layer (Fig. 4.5) and synthetic antiferromagnet systems (Fig. 4.8a,b) is striking. The formation of vortices is absent in synthetic antiferromagnet systems up to high drive current densities $J_c \gtrsim 2 \times 10^{12}$ A/m^2, even in notched nanostrips.

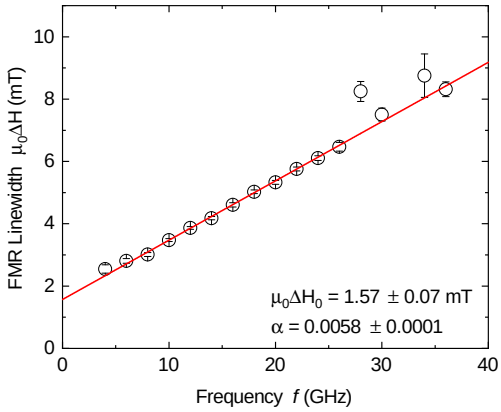


Figure 4.4: FMR linewidth as a function of microwave frequency. The solid line is a fit according to Eq. 4.2.

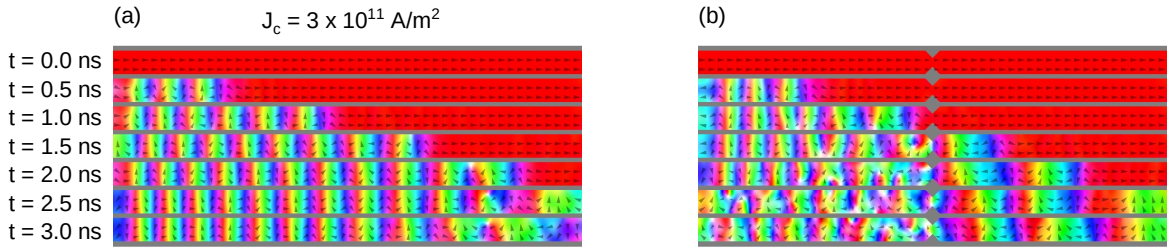


Figure 4.5: Micromagnetic snapshots of vortex formation in single layer (a) perfect and (b) notched nanostrips.

4.5 Results and Discussion

4.5.1 Excitation of Diffusive Spin Waves

To rule out any potential contributions from conventional diffusive spin waves to the superfluid-like spin transport we are interested in, we show that the propagation length of diffusive spin waves is much less than that of the length of the nanostrip in our simulated FeV synthetic antiferromagnet. Small cone angle spin waves are excited by applying the same spin transfer torque discussed in Sec. 4.2 but with $\vec{s} \parallel \hat{y}$. This will exert an in-plane torque on the magnetization in the injector. All other parameters are identical to those discussed in Sec. 4.2.

The deviation of the magnetization from the equilibrium position ($\vec{m} \parallel \pm\hat{x}$) is used as a judge of the spin current carried by the spin waves. We compute the time average value of m_y for each cell along $\hat{x}$. The resulting data, shown in Fig. 4.6, is fit with a standard exponentially

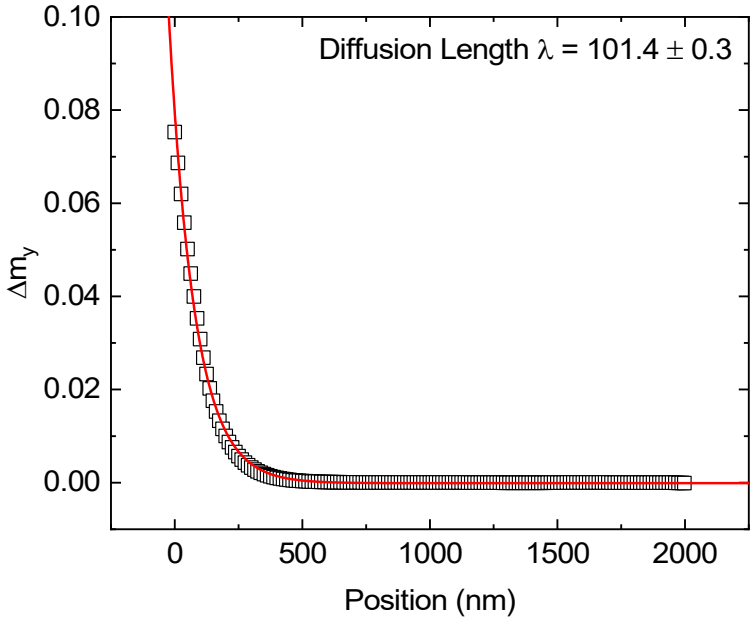


Figure 4.6: In-plane deviation of the magnetization from the $\hat{x}$-axis as a function of x position, related to the spin current carried by diffusive spin waves. The red line is an exponential decay fit from which the characteristic length scale is extracted.

decaying function ($m_y \sim \exp(-x/\lambda)$) where λ is the characteristic length scale of the decay. We obtain a spin diffusion length that is $\sim 5\%$ that of the length of the nanostrip, indicating that the spin waves dephase before they reach the sink region. This result unambiguously shows that the spin current we detect at the end of the nanostrip in later sections is solely carried by superfluid-like spin transport.

4.5.2 Diffusive Motion of an Isolated Domain Wall

In this section, we discuss the behavior of an isolated DW in both the perfect and notched nanostrips. Both simulations were performed identically at a charge current density of $J_c = 2.4 \times 10^{11}$ A/m^2. In order to rotate the magnetization, the energy supplied by the current-induced spin-transfer torque must overcome the energy barrier from the uniaxial shape anisotropy of the nanostrip. This implies a threshold current density required to excite the dynamics, i.e., inject a DW into the channel. Additionally when the drive current density is sufficiently low, only a single DW can be injected into the nanostrip. When the magnetization is rotated by 180°, a 180° DW is created at the boundary of the source. The DW is then injected into the nanostrip and driven by the out-of-plane canting angle Φ.

Perfect Nanostrip - We begin with the dynamics of a single DW injected by the spin polar-

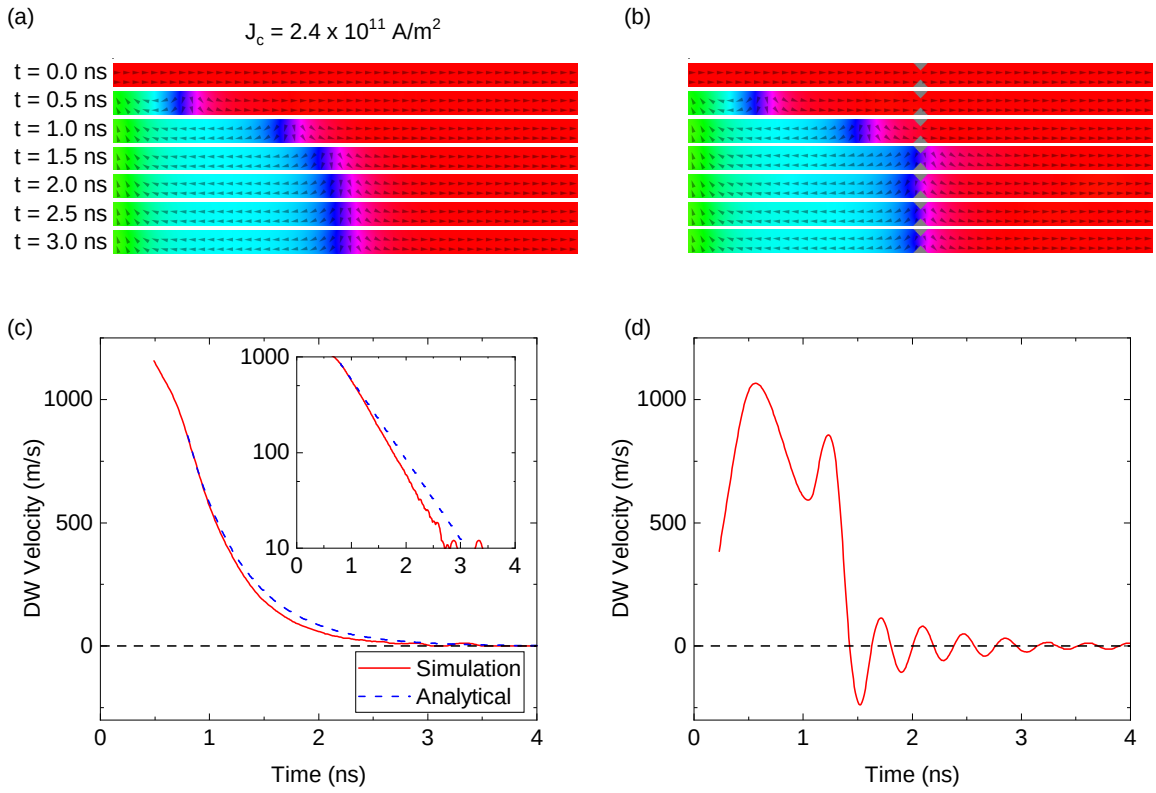


Figure 4.7: Micromagnetic snapshots of an isolated DW, taken every 0.5 ns from the start of the simulation in the (a) perfect and (b) notched nanostrips. The associated DW velocity as a function of simulation time is shown for the (c) perfect and (d) notched nanostrips. The inset in (c) shows the DW velocity on a logarithmic scale.

ized charge current density mechanism mentioned above. The micromagnetic snapshots in Fig. 4.7a show the isolated DW propagating along the nanostrip and coming to rest in the middle of the nanostrip. This is the point at which the total energy of the system with an isolated DW reaches a local minimum; the spin-transfer torque in the injection region is too weak to overcome the magnetostatically favored configuration where the strip is divided into two oppositely magnetized domains of equal size. The velocity of the isolated DW in the micromagnetic simulations, shown in Fig. 4.7c, decays in an exponential, diffusive manner. The simulation data shows an exponential decay time scale of $\tau = 0.45$ ns.

This diffusive motion (exponentially decaying velocity) of the isolated DW agrees with our one-dimensional analytical model in which the DW velocity is given by

$$v(t) = \lambda \gamma_K \Phi_0 e^{-\alpha \gamma_K t}. \tag{4.3}$$

Here $\lambda \approx 90$ nm is the DW width, $\gamma_K = \frac{K_\perp}{s(1+\alpha^2)}$ is a rate governed by the strength of the easy-plane anisotropy, $K_\perp$, and the spin density, s; Φ_0 is the initial out-of-plane canting

angle of the DW. Based on our material parameters our model predicts the velocity decays on a time scale $\tau = (\alpha\gamma_K)^{-1} = 0.52$ ns. The DW velocity predicted by our model, shown by the dashed blue curve in Fig. 4.7c, is in good qualitative agreement with the simulation results.

Notched Nanostrip - In the notched nanostrip, the isolated DW also experiences exponentially decaying motion. However, the motion is further complicated by an additional attractive force acting on the DW from the notch defect. The isolated DW propagates towards the notches and upon reaching the notch defect, the DW undergoes damped harmonic oscillations, as seen in Fig. 4.7d, eventually becoming pinned at the defect in the center of the nanostrip (see Fig. 4.7b). These oscillations of the DW about the center of a notch potential have previously been observed experimentally [164].

We conclude that both the perfect and notched nanostrips exhibit qualitatively similar behavior in the sense that the isolated DW is unable to propagate beyond the center of the nanostrip, either as a result of diffusive motion or DW pinning.

4.5.3 Weakly Interacting Domain Wall Train

Next we consider the motion of a weakly interacting DW train. By increasing the drive charge current density to $J_c = 3.0 \times 10^{11}$ A/m^2, multiple DWs can now be injected into the nanostrips, shown in Figs. 4.8a,b.

Perfect Nanostrip - In the perfect nanostrip the DWs individually continue to undergo exponentially decaying motion that is consistent with the behavior predicted by our model. This is shown by the DW velocity averaged across multiple DWs in the simulation in Fig. 4.8c (inset shows average DW velocity on a logarithmic scale).

As multiple DWs are injected into the nanostrip, they interact in a repulsive manner as a result of the homochirality of the DWs [165, 166]. These inter-DW interactions, similar to Coulomb repulsion, become responsible for the movement of the DW train past the middle of the nanostrip. Beyond the center point of the nanostrip, the repulsive interactions are aided by the DWs being attracted to the end of the nanostrip, where they are then annihilated at the sink.

Notched Nanostrip - In the notched nanostrip we also observe repulsive DW interactions, but the dynamics is now further complicated due to the notch defect. For $J_c = 3.0 \times 10^{11}$ A/m^2, the first injected DW propagates towards and is pinned at the notch defect, similar to that of an isolated DW. Meanwhile, additional DWs continue to be injected into the nanostrip, allowing for a series of DWs to build up behind the notch defect. This build-up eventually pushes the first DW through the pinning site, as seen in the micromagnetic snapshots in Fig. 4.8b.

Once the leading DW has been pushed through the notch defect, it is attracted to the end

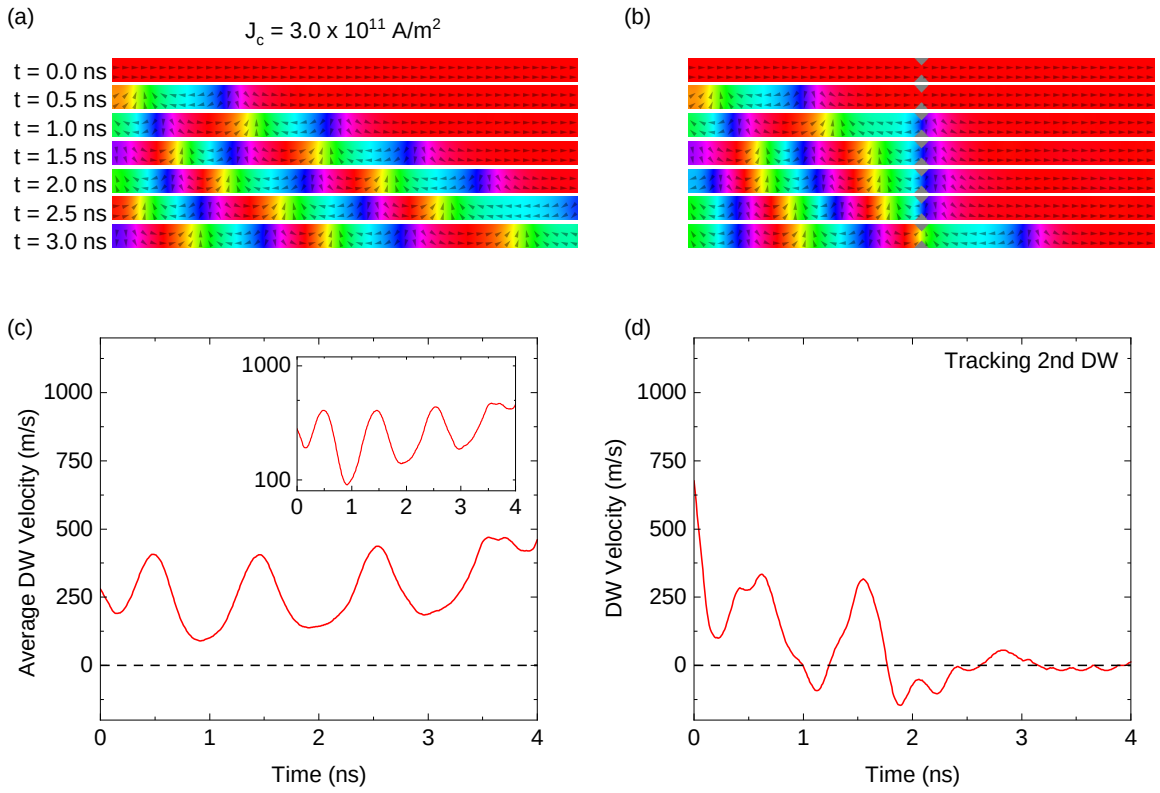


Figure 4.8: Micromagnetic snapshots of a weakly interacting DW train in the (a) perfect nanostrip and (b) notched nanostrip. In the notched nanostrip, note the momentary pinning of the first DW and the subsequent pinning of the DW train. The average DW velocity as a function of simulation time for the (c) perfect nanostrip and (d) the second DW in the train in the notched nanostrip. The inset in (c) shows the average DW velocity on a logarithmic scale.

of the nanostrip and annihilated. The second DW in the train is pushed along via the inter-DW interactions and then pinned at the notch defect. The corresponding DW velocity for this specific DW is shown in Fig. 4.8d. At this point, no additional DWs can be injected into the strip for the remainder of the simulation. The system reaches a steady state where the energy barrier to nucleate DWs is higher than the energy provided by current-induced spin-transfer torque.

We emphasize that the results in Figs. 4.8b,d do not show "fluid-like" dynamics – i.e., the spin transport is not hydrodynamic. Rather than flowing past the constriction as a fluid would, the spin transport is halted at the defect; the spin-transfer torque in the injection region is too weak to nucleate additional DWs and propel the train past the defect. Thus, at low drives, DW pinning provides a natural way to understand the interaction of easy-plane

precessional spin transport with defects.

4.5.4 Moderately Interacting Domain Wall Train

We now increase the charge current density to $J_c = 4.0 \times 10^{11}$ A/m^2 and observe the effect of increased DW density on pinning.

Perfect Nanostrip - The increased current density yields behavior similar to that discussed in Sec. 4.5.3 for the perfect nanostrip. The density of the DW train increases as more DWs can be injected into the nanostrip, see Fig. 4.9a. The average DW velocity, shown in Fig. 4.9b, shows a periodic behavior as the DWs are pushed away from trailing walls and slow down as they approach the next DW in the train. As a result of the increased density of DWs, and thus stronger repulsion between neighboring DWs, the average velocity is higher than in the case where $J_c = 3.0 \times 10^{11}$ A/m^2 (see Sec. 4.5.3 and Figs. 4.8a,c). The continuous motion of the DW train shown in Fig. 4.9a,b is beginning to approach the fluid-like regime.

Notched Nanostrip - At $J_c = 4.0 \times 10^{11}$ A/m^2, the pinning of the DW train disappears as a result of the stronger inter-DW interactions. The DWs are still impeded by the notch defect (Fig. 4.9b), evident by the reduction in average DW velocity in Fig. 4.9d when compared with the perfect nanostrip in Fig. 4.9c. However, they are pushed through before they can be pinned entirely, allowing for the DW train to move continuously throughout the nanostrip.

We observe that as the driving current density is increased, the density of the DWs increases. The increased DW density allows for individual DWs in the train to be less susceptible to pinning as a result of the stronger mutual repulsion between the homochiral DWs. The overall behavior of the magnetization in the nanostrips starts to approach that of fluid-like dynamics. This point is further verified by increasing the current density to higher values, as discussed in the next section.

4.5.5 Strongly Interacting Domain Wall Train

Finally, we examine the regime of a strongly interacting, dense DW train at $J_c = 8.0 \times 10^{11}$ A/m^2. Micromagnetic snapshots are shown in Figs. 4.10a,b, for the two geometries.

Perfect Nanostrip - In the perfect nanostrip, the DW train has condensed to the point that the DW separation distance is comparable to the individual DW width ~ 100 nm. At this point, the overall dynamics of the nanostrip begins to resemble that of superfluid-like spin transport [55, 61, 62, 67, 149, 150, 151] in the sense that the magnetization at a fixed position is precessing uniformly with simulation time. The average DW velocity, shown in Fig. 4.10c, no longer shows signs of the exponential decay of an individual DW. In fact, the DW velocity continues to increase as the DW traverses the strip. As they propagate further, the DW train begins to separate and individual DWs are attracted to the end of the strip where they are

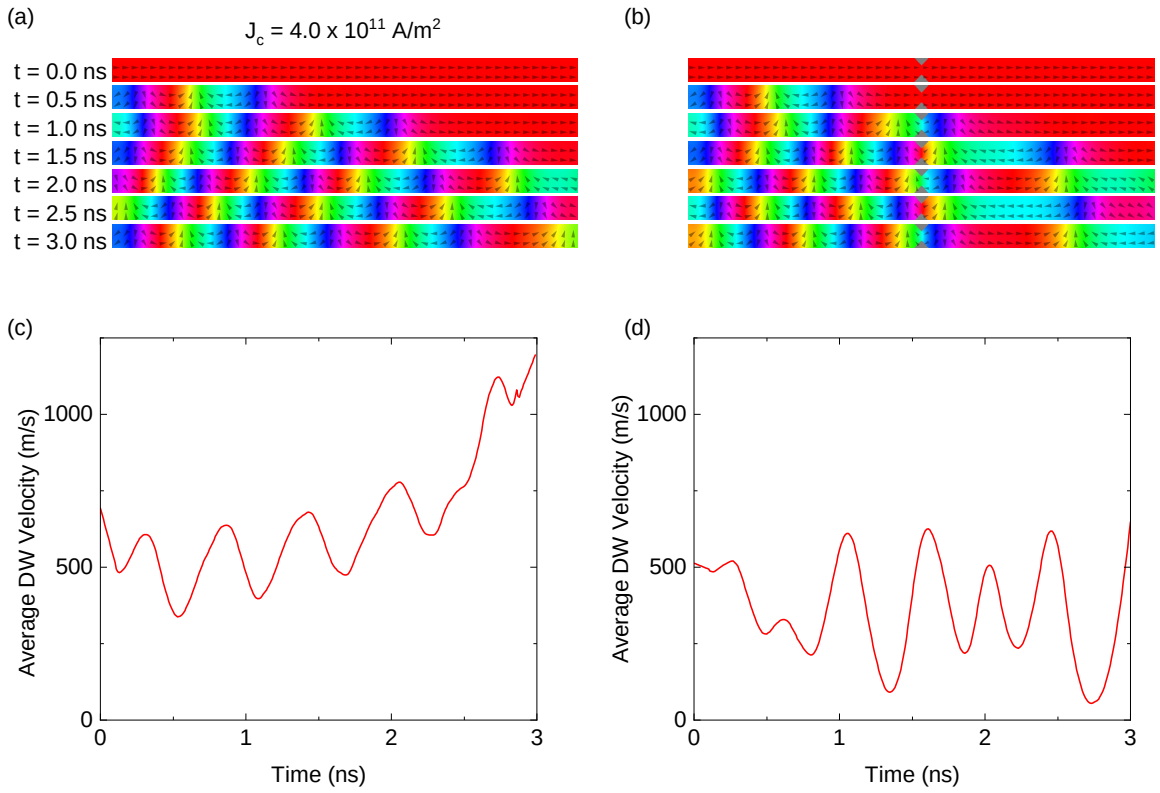


Figure 4.9: Micromagnetic snapshots of a weakly interacting DW train in the (a) perfect nanostrip and (b) notched nanostrip with the DW interactions are strong enough to overcome the pinning potential. The associated average DW velocity is shown for the (c) perfect and (d) notched nanostrips.

eventually annihilated.

Notched Nanostrip - In the notched nanostrip, the inter-DW interactions of the dense train have become strong enough to overcome the pinning potential well. As the DWs impinge on the notch defect, the pinning potential reduces the speed of the DW train momentarily, before the DWs are pushed through and become attracted to the end of the strip and speed up again. The reduction in DW velocity from the notch defect can be seen clearly in Fig. 4.10d. We also note the remarkable similarity in average DW velocity between the perfect and notched nanostrips up to the point of the notch defect.

Convergence to Fluid-like Regime - Our simulation results on the motion of a train of DWs showed pinning behavior present at lower J_c in notched nanostrips. At sufficiently high J_c, the pinning behavior vanishes and the DW perspective begins to converge with the hydrodynamic one. To show further agreement with the established hydrodynamic model, we relate the DW velocity to the conventional superfluid velocity $\nabla\phi$ (where in the hydrodynamic

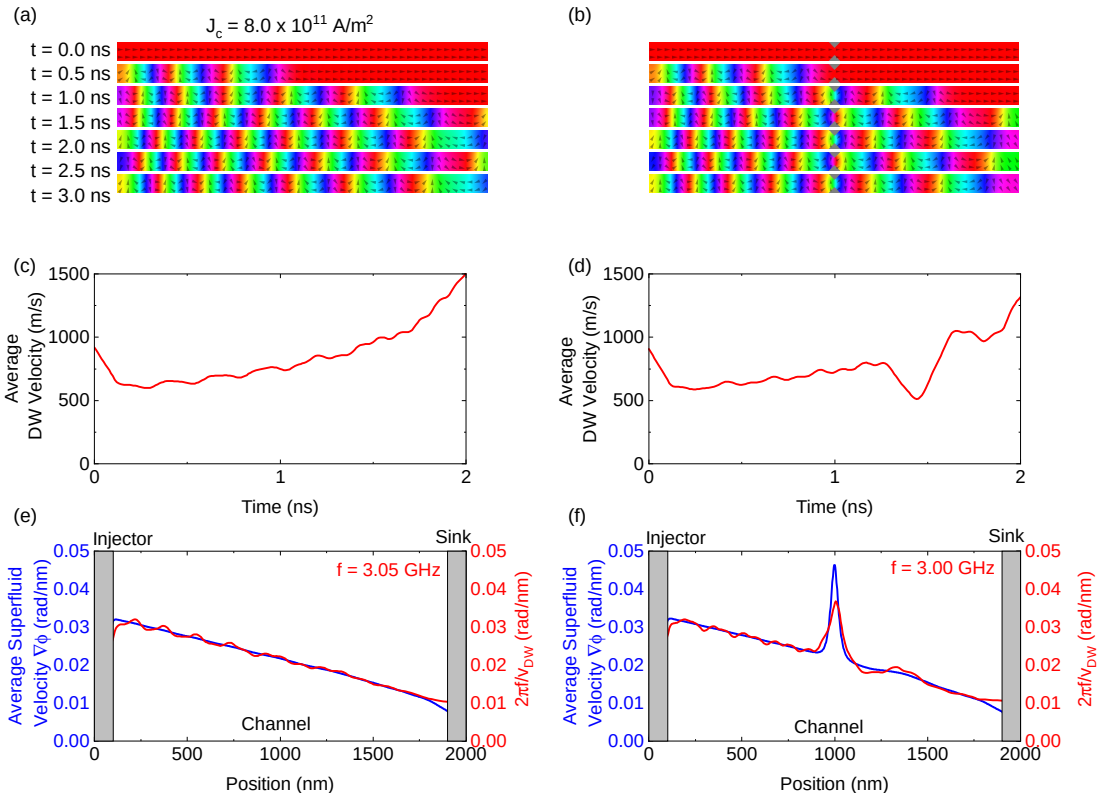


Figure 4.10: (a), (b) Micromagnetic snapshots of the densely packed DW train that resembles superfluid-like spin transport. (c), (d) The average DW velocity as a function of simulation time for the (c) perfect and (d) notched nanostrips. (e), (f) Time-averaged superfluid velocity and equivalent DW velocity, computed via Eq. (4.4), as a function of DW position for the (e) perfect and (f) notched nanostrips.

model the spin current $J_s \propto \nabla\phi$ [55]) through the following relationship:

$$\nabla\phi = \frac{2\pi f}{v_{DW}}. \tag{4.4}$$

Here ϕ is the in-plane angle the magnetization makes with the $\hat{x}$ axis, $\nabla\phi$ is the spatial gradient of ϕ (given in rad/nm), f is the precessional frequency of the magnetization, and v_{DW} is the average DW velocity.

We compute time-averaged $\nabla\phi$ directly (blue line) at each cell after reaching a steady state and compare it with the equivalent quantity using the average DW velocity (red line) in Fig. 4.10e and Fig. 4.10f. We first note the mostly linear decay of $\nabla\phi$ in the channel, indicating that we are indeed simulating easy-plane spin transport in the fluid-like regime at $J_c = 8.0 \times 10^{11}$ A/m^2. In this fluid-like regime, we find an excellent quantitative agreement between the hydrodynamic and DW perspectives for both the perfect and the notched

nanostrips. This agreement confirms that a densely packed DW train behaves as a "fluid" and converges with the hydrodynamic model.

In the notched nanostrips, the rapid increase in $\nabla\phi$ resulting from the constriction created by the notches is recreated well by our DW perspective. This increase in $\nabla\phi$, akin to throttling of a fluid, is also in great quantitative agreement with the DW perspective: The increase in $\nabla\phi$ corresponding with a reduction in DW velocity as the DWs propagate through the notch defect.

4.5.6 Consequences for Practical Applications

We now comment on the impacts our simulation results would have on experimental realizations of easy-plane precessional dynamics. In Fig. 4.11a we compare the time-averaged superfluid velocity $\nabla\phi$ as a function of charge current density J_c. The superfluid velocity shown in Fig. 4.11a was computed at $x = 1500$ nm, beyond the location of the notch defect, for both the perfect and notched nanostrips.

At low values of J_c ($< 5\times10^{11}$ A/m^2), we note a difference in the superfluid velocity between the two geometries. This is a result of pinning by the notch defect, impeding individual DWs within the train. The pinning behavior disappears with increasing J_c and the superfluid velocities in the two geometries become indistinguishable. Thus, at sufficiently high J_c, the notch defect evidently has no effect on the global dynamics of easy-plane precession. Remarkably the pinning vanishes despite the rather large size of the defect; at their deepest point, the pair of notches occupy 60% of the nanostrip's width, much larger than the typical edge roughness that results from lithographic patterning [167]. The robust transport, unaffected by such deep notches, is promising for achieving easy-plane precessional dynamics in lithographically patterned nanostrips.

To determine the equivalent DW velocity using Eq. 4.4, the precessional frequency f of the magnetization is determined using a fast Fourier transform on m_x as a function of time along the length of the nanostrip. We limit our determination of f to the fluid-like regime in which f is uniform throughout the nanostrip. Precessional frequency and equivalent DW velocity as a function of J_c are plotted in Fig. 4.11b and Fig. 4.11c, respectively. The superfluid velocity $\nabla\phi$ and precessional frequency f continuously increase with J_c but the DW velocity saturates at $\approx$ 1500 m/s. This saturation value is much higher than the typical experimentally measured value in in-plane magnetized strips [157, 158, 168], yet well below the maximum magnon group velocity in our system of $\approx$ 8000 m/s (derived from a micromagnetically computed magnon dispersion curve), which has been suggested to be the upper limit on DW velocity [169]. Instead of being limited by the magnon group velocity, the upper bound of the DW speed in our case appears to be closer to the minimum magnon phase velocity ($\approx$ 2000 m/s), which previously has been shown to restrict the speed of a single transverse Néel DW [170].

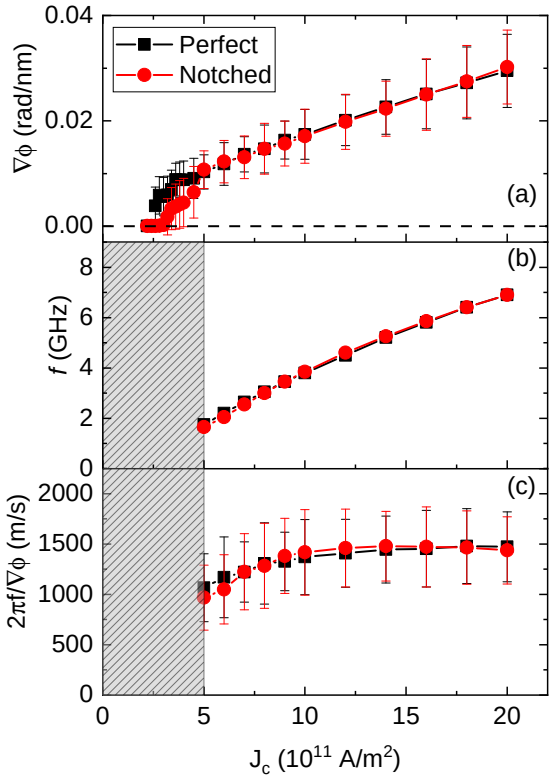


Figure 4.11: (a) Time-averaged superfluid velocity at $x = 1500$ nm as a function of driving current density J_c for the perfect (black squares) and notched (red circles) nanostrips. The error bars indicate the standard deviation. (b) Precessional frequency of the magnetization. (c) Equivalent DW velocity computed using Eq. 4.4 at $x = 1500$ nm

Our material parameters were chosen based on experimentally measured thin films of $Fe_{80}V_{20}$ with $\alpha = 0.006$ (see Sec. 4.3). This choice is in contrast to the typically chosen insulating ferrimagnetic oxide of yttrium iron garnet (YIG) with $\alpha \sim 10^{-5} - 10^{-4}$. However, YIG is notoriously challenging to grow and integrate into practical devices, as it requires fine control of deposition parameters and high processing temperatures. FeV alloys were chosen for their low-loss magnetic properties [106] and compatibility with CMOS-friendly Si substrates when deposited at room temperature [171]. Even though FeV alloys possess a damping parameter an order of magnitude larger than YIG, we were able to simulate fluid-like easy-plane spin transport at moderately achievable current densities (defined as when $\nabla\phi$ is the same for both the perfect and notched nanostrips, via Fig. 4.11a) at $J_c = 5.0 \times 10^{11}$ A/m^2. At lower current densities, $J_c \approx 3 \times 10^{11}$ A/m^2, the DW train could overcome pinning and was able to propagate throughout the entirety of the nanostrip. This would still allow for spin transport along the nanostrip (as a result of the rotating magnetization in the spin sink region) and the possibility of efficient micron-scale transmission of spin-based information.

Our chosen method of excitation simulates a current-perpendicular-to-plane spin valve nanopillar with an out-of-plane polarizer. This is a well-established technique in orthogonal spin-torque oscillators [28]. Thus, the simulated dynamics here in principle can be achieved using experimentally proven physics and device structures. Additionally, recent studies have pointed to the possibility of in-plane magnetized films producing an out-of-plane spin torque [42, 43]. This out-of-plane spin-orbit torque could prove to be a viable method of exciting easy-plane precessional dynamics as it would eliminate the need for complicated fabrication of nanopillar spin valves. However, it is unclear at this time if this torque would be strong enough to drive the easy-plane precession dynamics simulated here.

It is worth pointing out that while our simulations were performed at zero temperature, experimental attempts at achieving easy-plane precessional dynamics will be done at finite temperatures. Finite temperatures allow for the emergence of diffusive thermal magnon transport, which could couple to the easy-plane spin transport and provide another avenue for dissipation that is not captured by the Gilbert damping parameter [56]. In our zero-temperature simulations, there are no thermal magnons that could give rise to the additional non-Gilbert dissipation. While possible dissipation pathways via thermal magnons are beyond the scope of this present work, future studies employing finite-temperature micromagnetic simulations may give insights into such dissipation in easy-plane spin transport.

4.6 Conclusion

We performed micromagnetic simulations on the interaction of homochiral DW transport via easy-plane precession in synthetic antiferromagnet nanostrips with and without a notch defect. We observed the diffusive motion of an isolated DW and subsequent pinning at the notch defect at low J_c. With increasing J_c multiple DWs are injected into the nanostrip, and we observed the crossover to a fluid-like, densely packed DW train. The densely packed DW train in notched nanostrips is robust to edge defects and shows no difference to the perfect nanostrips in the fluid-like regime. Our simulations, with material parameters taken directly from experimentally measured metallic ferromagnets, demonstrate promise for an experimental realization of easy-plane precession at reasonable current densities for efficient micron-scale spin transport.

Chapter 5

Unconventional Spin Torques in Exchange-Biased Spin Valves

This chapter discusses original work on measuring spin torques in current-in-plane spin valve structures. I was responsible for performing the experimental measurements discussed and data analysis. The samples were created by a team at Western Digital and the photolithography was performed by students in Prof. Jean J. Heremans' group at Virginia Tech.

5.1 Introduction

Spin-orbit torques (SOTs) have emerged in recent years as a promising method for all electrical control of magnetization [37]. By passing a charge current through a material with high spin-orbit coupling, a transverse spin current can be generated and pumped into a nearby magnetic layer. This transverse spin current exerts a torque on the magnetization via transfer of spin angular momentum and can be used to drive easy-axis small cone angle precession as well as induce switching of in-plane magnetization [30, 78, 84, 172, 173, 174, 175].

A commonly used method for charge-to-spin conversion is the conventional spin Hall effect [34, 78], an example of which is shown in Fig. 5.1. Here a charge current passes through a heavy metal/ferromagnet (HM/FM) bilayer. The charge current passing through the high spin-orbit coupling HM is converted into a spin current flowing along the direction of broken inversion symmetry (in this case along $\hat{z}$) with the resulting spins polarized along $\hat{y}$. The high symmetry of the HM/FM systems restricts the spin polarization to lie within the plane of the film, making deterministic switching of perpendicular magnetization impossible as there is nothing to break the in-plane symmetry.

Recently theoretical [38, 39, 40, 176] and experimental [43, 105, 177, 178] studies have looked at charge-to-spin conversion in systems with broken in-plane symmetry. This has been done through reduced crystal symmetry [42, 179, 180, 181] or through the presence of magnetic ordering [43, 80, 105, 182]. By flowing a charge current along the direction of broken symmetry, spin currents with a polarization component along the out-of-plane (OOP) direction have been achieved.

While symmetry consideration dictates that such OOP-polarized spin currents are permitted in some material systems with broken in-plane symmetry [38], there can be different microscopic mechanisms that actually produce the OOP-polarized ($\hat{z}$-polarized) spin currents. One possible scenario is that $\hat{y}$-polarized spins from the conventional spin Hall effect or anomalous Hall effect become rotated to develop a finite $\hat{z}$ component. The rotation of the spins has been attributed to an interfacial spin-orbit field (i-SOF) at the ferromagnet/normal metal interface. This OOP component is essential for field-free switching of perpendicularly magnetized storage media. Not only that, but it can also be used to drive easy-plane precession for a new class of spin torque oscillators with increased power outputs [183], like those shown in Fig. 5.1b, as well as superfluid-like spin transport [147].

In this chapter, we discuss the results of spin torque measurements in all in-plane magnetized metallic spin valve structures. We break the in-plane symmetry using a ferromagnetic source

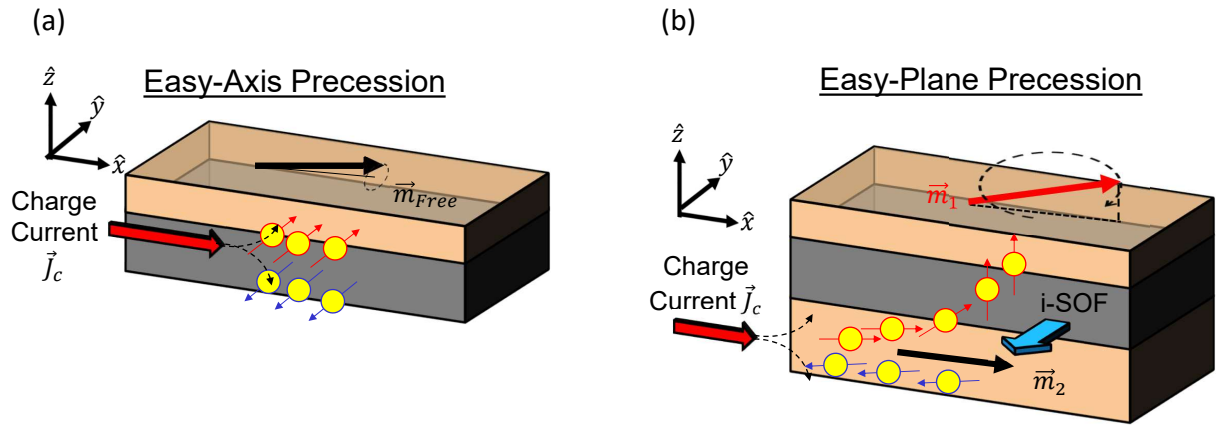


Figure 5.1: (a) Easy-axis precession of the magnetization as a result of the spin Hall effect. (b) Easy-plane precession that could arise from out-of-plane spin polarization.

layer and fix its direction via exchange bias. By studying the angular dependence of spin torque ferromagnetic resonance (FMR) lineshape [83], we are able to directly probe the nature of spin-orbit torques found in this system. We find that, contrary to other studies, the out-of-plane component of spin polarization that exerts a torque on our magnetic free layer is nearly negligible and at most a few percent of the Oersted field torque. This result is supported by DC bias dependent measurements, where signs of a damping-like torque effecting the FMR linewidth is absent but effects due to the Oersted field torque on the FMR resonance field can clearly be seen. These results help to shed light on the origins of this novel spin precession effect and what material systems can benefit from it for device applications.

5.2 Experimental Methods

Spin valves structures were deposited via magnetron sputtering in a collaboration with Western Digital. Samples were deposited on Si/SiO_2 substrates with the stack structure Si/SiO_2(subst.) / Ta(3) / Ru(3) / $Ir_{20}Mn_{80}$(5) / $Co_{75}Fe_{25}$(4) / Cu(4) / $Ni_{80}Fe_{20}$(8) / Ru(3) / Ta(3) / Ru(2) where the layer thickness is indicated in parentheses and given in nanometers. The samples were annealed post-deposition at 300 °C and in an in-plane magnetic field of 5 T before being cooled to room temperature under the same field. An example of the magnetic portion of the stack structure is shown in Fig. 5.2a. The antiferromagnetic IrMn

couples to the ferromagnetic CoFe and creates an exchange bias [86], preferentially fixing the direction of the CoFe magnetization. The CoFe layer serves as the spin source layer. The nonmagnetic Cu spacer, with its long spin diffusion length, decouples the CoFe and NiFe layers. The NiFe serves as the free layer and is the layer that will undergo FMR.

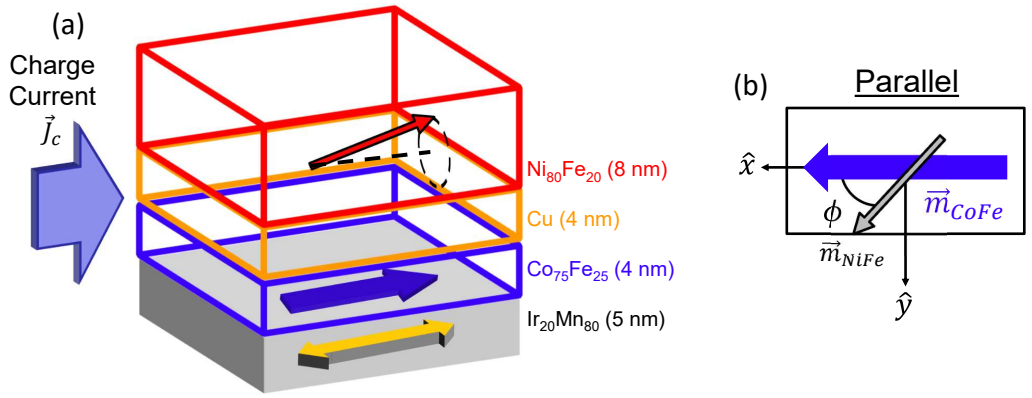


Figure 5.2: (a) Stack structure showing the IrMn/CoFe/Cu/NiFe portion with thickness and relative direction of the antiferromagnetic ordering in IrMn and magnetization in CoFe and NiFe. (b) Orientation of the magnetization fixed layer in CoFe with respect to the NiFe magnetization. The angle between these two magnetization vectors is defined as ϕ. We assume that the NiFe magnetization is perfectly aligned with the external magnetic field when the applied field is greater than the NiFe coercivity and the CoFe layer does not deviated from the exchange bias direction.

Vibrating sample magnetometry (VSM) was utilized to measure angular dependent hysteresis loops and exchange bias within the film plane using a Microsense EZ9 VSM. Samples were patterned into microstrips of dimension 50 μm $\times$ 10 μm with the exchange bias parallel to the device length using conventional photolithography and ion milling for spin torque ferromagnetic resonance (ST-FMR) measurements (lithography was performed by students in the JJH group at Virginia Tech). ST-FMR measurements were performed using a home built system with a rotatable electromagnet at a RF power of $P_{RF} = 6$ dBm and an excitation frequency of $f = 4$ GHz. An example of the ST-FMR schematic can be found in Fig. 2.5. The DC electrical resistance and the anisotropic and giant magnetoresistance (AMR and GMR, respectively) ratios of the microstrip were determined using the same two-point ground-signal-ground probe with the microwave power set to $P_{RF} = -20$ dBm. A DC current source was connected to the inductor leg of the bias tee to perform DC bias measurements. All measurements were performed at room temperature.

5.3 Results

5.3.1 Static Magnetic Properties

We start by discussing the result of VSM measurements to confirm the direction and strength of the magnetic exchange bias. An example hysteresis loop is shown in Fig. 5.3. The reversal of the two magnetic layers (NiFe < 1 mT, shaded red, and CoFe ~ 100 mT, shaded blue) is clearly separated, confirming the two layers are decoupled from each other. The center of the shifted loop is indicative of the magnetic exchange bias and is a result of the IrMn/CoFe interface. Since the coercivity of the NiFe layer is much less than that of the CoFe layer, we are able to freely rotate the magnetization of the NiFe layer within the plane of the film without disturbing the exchange biased CoFe magnetization, as depicted in Fig. 5.2b.

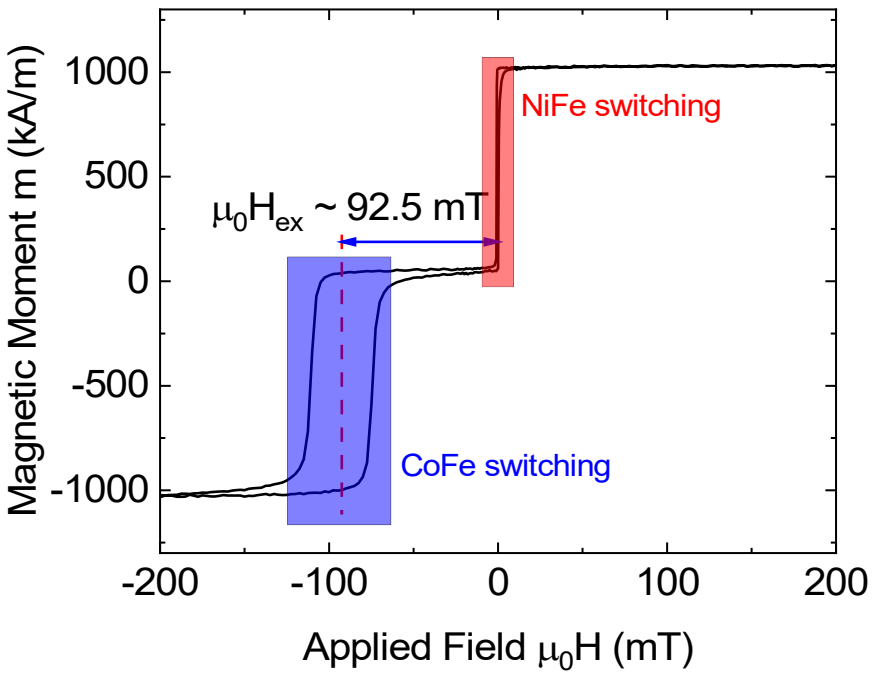


Figure 5.3: Hysteresis loop showing the strength of the exchange bias and individual switching of the two magnetic layers. The magnitude of the exchange bias field is determined by estimating the center of the shifted minor loop. The applied field is parallel with the magnetic exchange bias direction.

5.3.2 Electrical Resistance Measurements

DC resistance measurements were performed to quantify the AMR and GMR ratios, as well as the angular dependence of sample resistance. Using a ground-signal-ground two-point probe, the electrical resistance of the sample was determined with the magnetic field applied parallel and antiparallel to the exchange bias. The GMR ratio, determined by

$$GMR = \frac{R_P - R_{AP}}{R_P}, \tag{5.1}$$

where R_P (R_{AP}) is the resistance of the sample when the two magnetic layers are parallel (antiparallel), was measured to be $\sim 1.3\%$ across all samples.

To understand the angular dependence of the sample resistance, the ST-FMR setup was used to provide a rotatable magnetic field. The microwave power was set to $P_{RF} = -20$ dBm so as to not excite FMR. A DC bias current was applied and the sample resistance measured while the magnetic field was swept from $\mu_0 H = 100$ mT to $\mu_0 H = -100$ mT and back to $\mu_0 H = 100$ mT. A selection of magnetoresistance curves at different field angles are shown in Fig. 5.4a. The sample resistance was extracted at a magnetic field strength of ~ 20 mT, in the range of the FMR resonance field at 4 GHz. The resulting angular dependence of sample resistance is shown in Fig. 5.4b.

The rotation of the NiFe layer with respect to the current direction will result in AMR, where the sample's resistance changes as ϕ changes. Additionally, since our samples contain two magnetic layers, there will be spin-dependent scattering of the in-plane charge current between these two layers, giving rise to GMR. Therefore both the AMR and GMR effects need to be considered when fitting the sample resistance. We can describe the angular dependence of sample resistance using

$$R(\phi) = R_0 + R_{AMR}\cos^2(\phi) + R_{GMR}\cos(\phi - \phi_{GMR}), \tag{5.2}$$

where R_{AMR} is the magnitude of the AMR, R_{GMR} is the magnitude of the GMR effect and ϕ_{GMR} is a phase shift introduced to account for the different directions of exchange bias relative to the current flow direction. For the sample orientation here $\phi_{GMR} = \pi$. Eq. 5.2 is used to fit the angular dependent sample resistance data and is shown by the solid black line in Fig. 5.4b. We find that AMR accounts for a $\sim 0.4\%$ change in the sample resistance (contribution shown by solid blue line) and GMR accounts for $\sim 1.3\%$ (contribution shown by solid red line). An understanding of the angular dependence of sample resistance and magnitude of the AMR and GMR effects is crucial to describing the angular dependence of the ST-FMR signal, as will be discussed in the next section (Sec. 5.3.3).

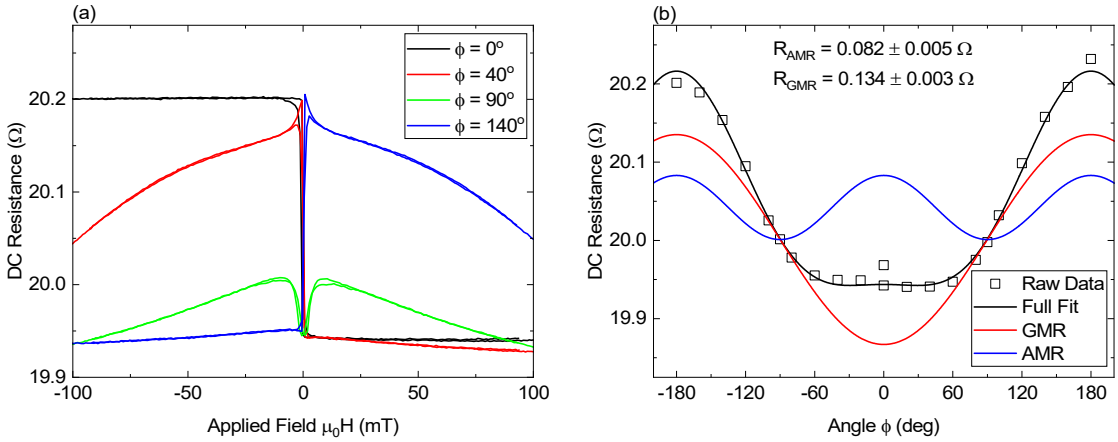


Figure 5.4: (a) Sample resistance as a function of external field for various field angles. (b) DC resistance, extracted from (a) at ~ 20 mT, as a function of applied magnetic field angle. The black line is a fit according to Eq. 5.2 and the red (blue) line shows the GMR (AMR) contribution to the total resistance.

5.3.3 Angular Dependence of ST-FMR Signal

We now move on to discussing angular dependence of the ST-FMR signal. ST-FMR spectra were acquired at various angles of magnetic field with respect to the current direction (i.e. along the direction of the nanostrip). The spectra were fit according to Eq. 2.5 where the resonance field, linewidth, symmetric and antisymmetric Lorentzian amplitudes are extracted for each field angle. An example spectrum is shown in Fig. 5.5 with the corresponding symmetric V_{sym} and antisymmetric V_{asym} components.

The ST-FMR spectral amplitude evolves as the angle between the magnetic field and current direction changes according to

$$V_{mix} \propto \frac{dR}{d\phi}\tau(\phi), \tag{5.3}$$

where $dR/d\phi$ is the derivative of sample resistance with respect to field angle ϕ, and $\tau(\phi)$ describes the spin torques acting on the system. The torques $\tau(\phi)$ can be separated into in-plane $\tau_{\parallel}$ and out-of-plane $\tau_{\perp}$ torques. These torques give rise to the symmetric and antisymmetric components of the ST-FMR signal, respectively. The in-plane torques can be described by

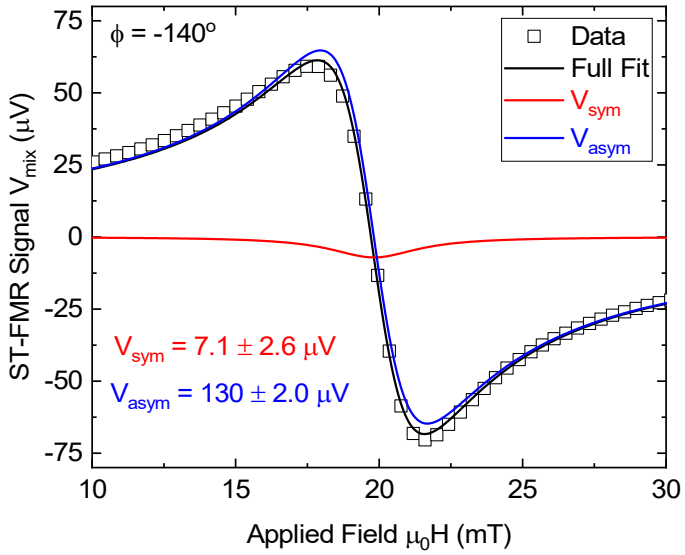


Figure 5.5: ST-FMR signal fit according to Eq. 2.5 and decomposed into the symmetric V_{sym} and antisymmetric V_{asym} Lorentzians.

$$\tau_{\parallel} = \tau_s \cos(\phi), \tag{5.4}$$

where τ_s represents the torque that could arise due to the spin Hall effect [78, 161]. (However, this symmetric Lorentzian signal (Eq. 5.4) could also contain contributions that are unrelated to the actual in-plane torque. These spurious contributions include spin pumping [184, 185] or thermoelectric effects such as the anomalous Nernst effect [186, 187]. We therefore caution against relying on the symmetric Lorentzian signal to quantify the in-plane torque.) The out-of-plane torques can be described by

$$\tau_{\perp} = \tau_{Oe} \cos(\phi) + \tau_z, \tag{5.5}$$

where τ_{Oe} is a measure of the torque due to the Oersted field and τ_z measures the torque caused by out-of-plane spin polarization [42].

Using Eqs. 5.2, 5.4, and 5.5 with Eq. 5.3, we can predict what the angular dependence of the ST-FMR signal should be. For our sample geometry, we expect the symmetric component to be

$$V_{sym} = -R_{AMR}\tau_s \sin(2\phi)\cos(\phi) + R_{GMR}\tau_s \sin(\phi)\cos(\phi), \tag{5.6}$$

and the antisymmetric component

$$V_{asym} = -R_{AMR}\tau_{Oe}\sin(2\phi)\cos(\phi) + R_{GMR}\tau_{Oe}\sin(\phi)\cos(\phi) - R_{AMR}\tau_z\sin(2\phi) + R_{GMR}\tau_z\sin(\phi). \quad (5.7)$$

Since we are interested in measuring an out-of-plane torque, we focus on the angular dependence of the antisymmetric component V_{asym} (Eq. 5.7).

The results in Fig. 5.6a use Eq. 5.7 and the fit results from angular resistance to determine the strength of the out-of-plane torque τ_z relative to τ_{Oe}. What we find is that the out-of-plane component is very small, less than a percent of the Oersted field torque. This is contrast with previous studies that reported substantial out-of-plane anti-damping torques, some strong enough to switch perpendicular magnetization [43]. In fact, we are able to fit the data just as reasonably well if we assume that τ_z is not present (i.e. fix $\tau_z = 0$), further supporting this result.

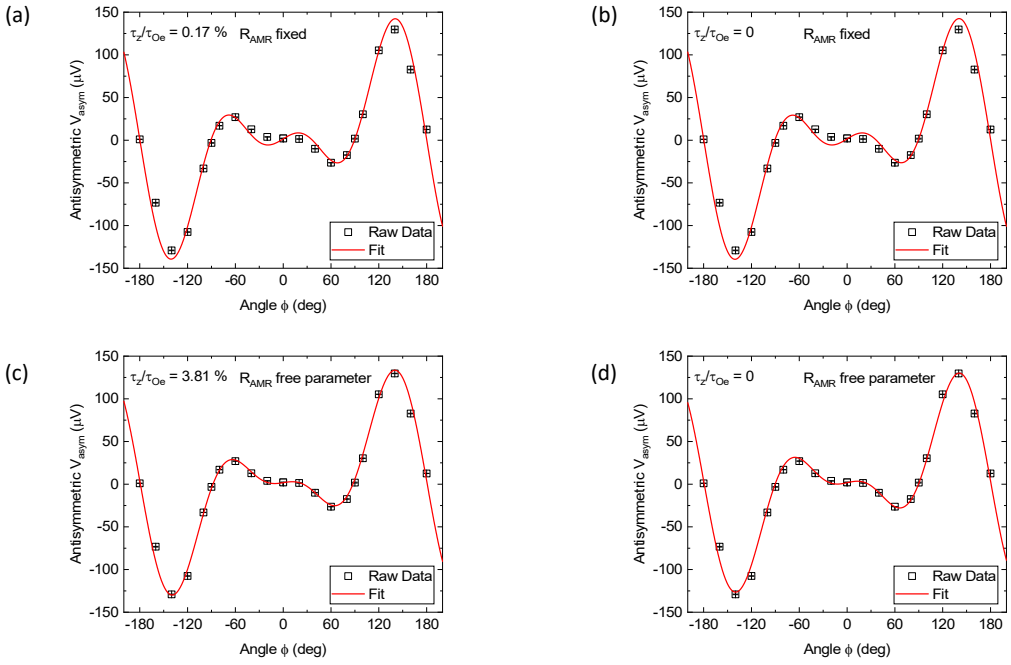


Figure 5.6: Antisymmetric amplitude V_{asym} as a function of applied field angle ϕ. The solid line is a fit to Eq. 5.7. In (a) τ_z is a free parameter and R_{AMR} is fixed to the value determined from Fig. 5.4. In (b) τ_z is fixed to zero and R_{AMR} is fixed to the same value as in (a). In (c) both τ_z and R_{AMR} are allowed to be free parameters. In (d) R_{AMR} is a free parameter and τ_z is fixed to zero. The quality of the fit significantly increases from (a) to (c) and marginally changes between (c) and (d).

We note that our fit line deviates from the measured data at lower angles but matches well at higher angles, suggesting that there is room for improvement in our fit results. By allowing R_{AMR} to be a free parameter alongside τ_z and τ_{Oe} but fixing R_{GMR} (we keep R_{GMR} fixed as the fit value agrees reasonably well with that from angular resistance measurements, and having all four parameters free in Eq. 5.7 would make fitting impossible due to mutual dependencies) we fit our experimental data again. Using this approach, our fit improves significantly and returns a value of R_{AMR} that is $\sim 13\%$ lower than that determined from angular resistance measurements. The magnitude of τ_z/τ_{Oe} increases to $\sim 3.81\%$. However, we are still able to fit the measured data just as well by assuming that $\tau_z = 0$ and R_{AMR} is now a free parameter; the fit value is $\sim 11\%$ lower than that from angular resistance measurements. A summary of the fitting parameters for each scenario is presented in Table 5.1.

Fig. 5.6	τ_z (μV/Ω)	τ_{Oe} (μV/Ω)	R_{AMR} (Ω)	R_{GMR} (Ω)
a	-1.888 ± 37.55	-1103 ± 90	0.082	0.134
b	0	-1103 ± 86	0.082	0.134
c	39.87 ± 14.31	-1048 ± 33	0.0712 ± 0.0012	0.134
d	0	-1062 ± 38	0.0725 ± 0.0012	0.134

Table 5.1: Summary of fit parameters from Eq. 5.7 for the angular dependence of the antisymmetric component V_{asym} for the various scenarios presented in Fig. 5.6. Numbers without uncertainties represent fixed values.

5.3.4 DC Bias Dependence of ST-FMR Signal

We now discuss how the ST-FMR resonance field and linewidth changes when a DC bias current is applied during the measurement. If the torque due to out-of-plane spin polarization does take the form of an damping-like or antidamping-like torque, we should be able to detect its effect on the FMR linewidth. Additionally any shift in the FMR resonance field can be attributed to field-like torques, allowing us to estimate the effective Oersted field torque. To do this, we performed ST-FMR measurements with different DC bias currents at various field angles. The resulting change in the FMR resonance field or linewidth is then fit with a linear function to determine the modulation efficiency ($\mu_0 H_{res}/I_{DC}$ or $\mu_0 \Delta H/I_{DC}$) at each field angle ϕ [105].

The FMR resonance field at $\phi = -100°$ as a function of DC bias current is shown in Fig. 5.7a. By choosing an angle that is nearly parallel with the Oersted field, we can clearly see the shift in $\mu_0 H_{res}$ with a DC bias current. This is to be expected as the Oersted field generated by the DC current take the form of a field-like torque and can either point nearly parallel or antiparallel to the magnetization, thereby increasing or decreasing the effective field. FMR

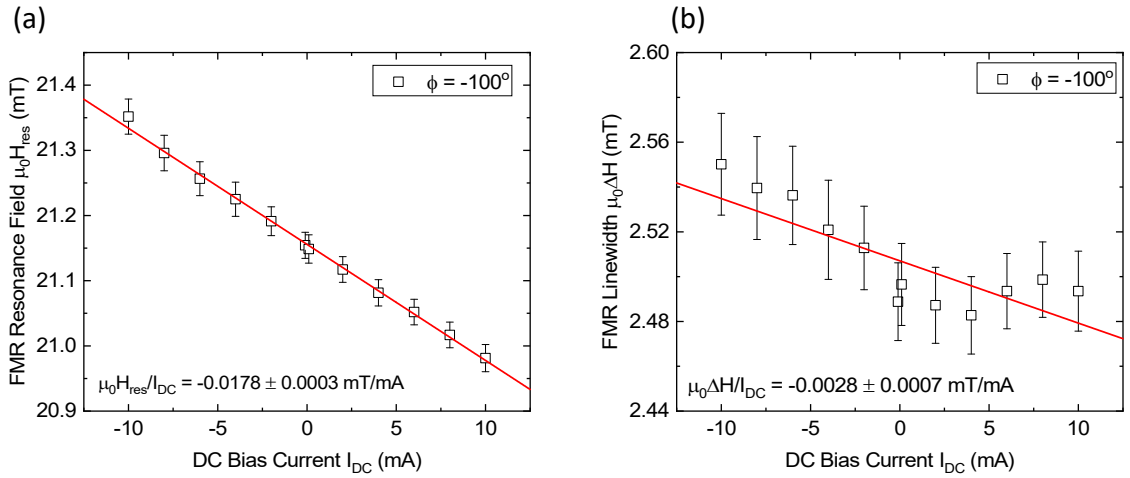


Figure 5.7: (a) FMR resonance field and (b) FMR linewidth as functions of DC bias current at $\phi = -100°$. The solid line is a linear fit from which the slope is extracted for each plot.

linewidth modulation as a function of DC bias current, also at $\phi = -100°$, is shown in Fig. 5.7b. Within our error bars, it is difficult to confirm a linear trend. This suggests that any damping-like torques present are small, in line with our conclusion from angular dependent ST-FMR measurements at zero DC bias.

By performing DC bias measurements throughout the whole angle range, we can monitor how both modulation efficiencies, $\mu_0 H_{res}/I_{DC}$ and $\mu_0 \Delta H/I_{DC}$, change with ϕ. The angular dependence of $\mu_0 H_{res}/I_{DC}$ is shown in Fig. 5.8a. The angular dependence of $\mu_0 H_{res}/I_{DC}$ shows a clear sinusoidal dependence (solid line) that is in agreement with the expect symmetry of the Oersted field torque.

We estimate the effective Oersted field per unit current, calculated from the slope $\mu_0 H_{res}/I_{DC}$ and using the projection of H_{Oe} along $\vec{m}_{NiFe}$, is ~ 0.0175 mT/mA. We can estimate the Oersted field per unit current by approximating our sample as an infinitely large conducting plate

$$\frac{\mu_0 H_{Oe}}{I_{DC}} = \frac{\mu_0 f}{2w}. \tag{5.8}$$

Here $f \approx 70\%$ is the fraction of current I_{DC} flowing through all layers bar NiFe and $w = 10$ μm is the width of the sample. The current fraction for each layer is determined by measuring the sheet resistance of each individual layer and using a parallel resistor model. Using Eq. 5.8 we estimate that $\mu_0 H_{Oe}/I_{DC} \sim 0.0536$ mT/mA, well above the result we estimated using

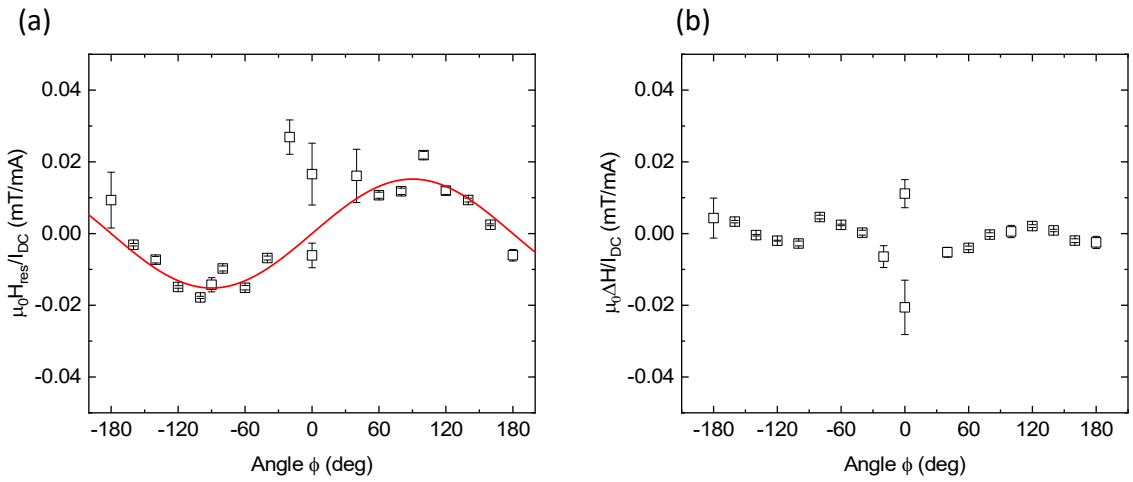


Figure 5.8: (a) Angular dependence of the FMR resonance field modulation efficiency. The solid line is a sinusoidal fit. (b) Modulation efficiency of the FMR linewidth as a function of field angle. The scatter in data points in both (a) and (b) at small field angles is likely a result of the signal amplitude being very small and difficulties in accurately fitting the data.

the resonance field shift. This could be a result of underestimation of the current fraction or not fully considering the total current induced field acting on the magnetization [92]. A more likely explanation is that there is a very thin film of metallic material leftover on the substrate from the ion milling process. This would create a path for the current to shunt through, bypassing our spin valve structure. Further optimization of the ion milling process could help to avoid this issue in the future.

Any trend present in $\mu_0 \Delta H / I_{DC}$ is less obvious, further supporting our claim that the damping-like torques in this system are small. While any change we measure in the FMR linewidth with a DC bias current may be small, we can attempt to put an upper limit on the effective damping-like torque efficiency from the CoFe source layer. We estimate the effective spin Hall angle using [78, 188, 189]

$$|\theta_{DL}| = \frac{2|e|}{\hbar} \frac{(H_{res} + M_{eff}/2)\, \mu_0 M_{sat}(t_{NiFe})(t_{CoFe}) w}{|\sin(\phi)| f_{CoFe}} \left(\frac{\gamma}{2\pi f}\right) \left|\frac{d(\Delta H)}{d(I_{DC})}\right|, \tag{5.9}$$

where $|e|$ is the electron charge, $\hbar$ is the reduced Planck constant, $H_{res} \approx 16.8$ kA/m, $M_{eff} =$

(M_{sat} =) 740 kA/m is the effective (saturation) magnetization of NiFe, and $t_{NiFe} = 8$ nm ($t_{CoFe} = 4$ nm) is the thickness of the NiFe (CoFe) layer, $w = 10$ μm is the device width, $|\gamma'| = \gamma/(2\pi) = 29.7$ GHz/T is the reduced gyromagnetic ratio, $f = 4$ GHz is the excitation frequency, and $f_{CoFe} = 0.24$ is the fractional current flowing through the CoFe source layer. This yields an effective spin Hall angle upper bound of $|\theta_{DL}| = 0.0241 \pm 0.0054$, quite smaller than effective spin Hall angles found in other heavy-metal [98, 190] or ferromagnetic [84, 188] systems. This could explain any lack of apparent sinusoidal behavior in $\mu_0 \Delta H / I_{DC}$ vs. ϕ that we would expect of the spin Hall effect. However, we caution against reading too much into this value because of the possible current shunting issues mentioned above. If this is the cause of a reduced apparent Oersted field, then the effective spin Hall angle could be higher than this estimate and potentially bring the value into line with those of other heavy metal source layers.

5.4 Discussion

The results presented thus far have suggested that the magnitude of the out-of-plane torque due to out-of-plane spin polarization is at most a few percent of the Oersted field torque or entirely absent in our in-plane magnetized spin valve structures. This is in contrast to previous studies that investigated the same effect in spin valve structures [43, 105]. We can speculate as to a few possible reasons why we are not able to measure a substantial out-of-plane spin polarization torque.

The effect studied here relies on spin current generation within the CoFe layer, so if there is not much charge current passing through there, not much spin current will be generated. It is possible that most of the current is being shunted through the low resistivity Cu layer. Using a parallel resistor model, we estimate that $\sim$ 35% of the current flowing through the sample passes through the Cu layer and $\sim$ 24% passes through CoFe. While a parallel resistor model does not come without its drawbacks (e.g. assuming perfect interfaces, not considering nominal versus actual layer thicknesses), this gives a ballpark on the relative current distribution. Decreasing the current shunting through Cu by reducing the Cu thickness could aid to increase the effect of out-of-plane spin polarization on NiFe, but potentially could also introduced adverse effects from dipolar coupling of the two magnetic layers.

Low spin-orbit coupling (e.g., weak spin Hall effect) within CoFe leads to only a small amount of spin accumulation, and hence, small amount of spin current. Indeed our results of linewidth vs DC bias point to a rather small, if any, damping-like torque from $\hat{y}$-polarized spin current expected from the conventional spin Hall effect. If there is only a small amount of $\hat{y}$-polarized spins generated by the CoFe source to begin with, we expect the torque from rotated $\hat{z}$-polarized spins to be small as well. The weak spin-orbit coupling could also lead to the interfacial spin-orbit fields at the CoFe/Cu and/or Cu/NiFe interfaces may be too weak. This could result in the spins not being rotated out-of-plane significantly to the point that their effect on the NiFe layer is below the detection limits of our system. A visualization of

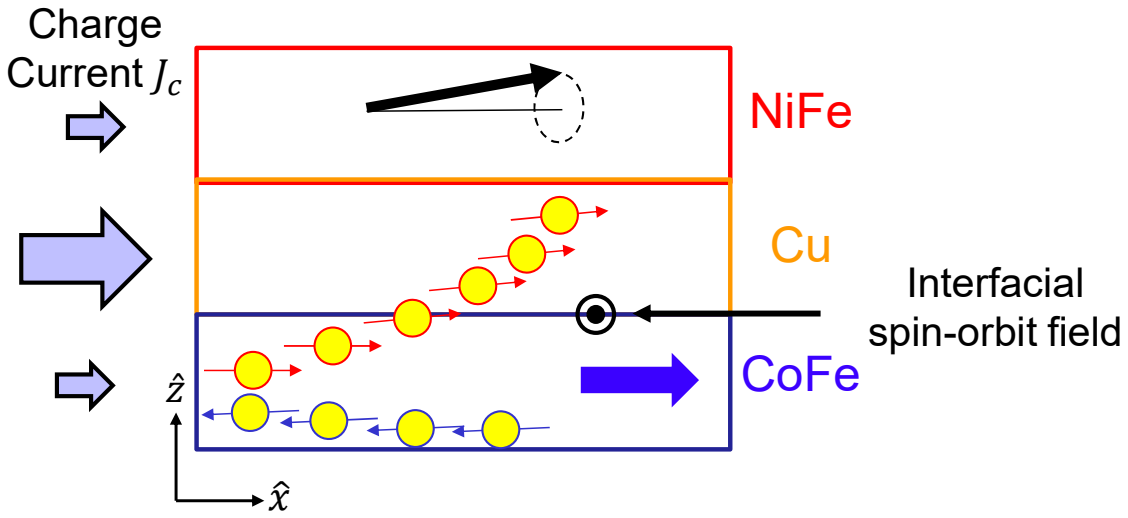


Figure 5.9: Visualization of reduced interfacial spin-orbit field not rotating the spins enough out-of-plane to have a noticeable effect on the precessing NiFe magnetization.

this possibility is shown in Fig. 5.9. Replacing the CoFe source layer with a material that has a higher effective spin Hall angle while retaining broken in-plane symmetry (i.e. magnetic ordering) could be a possible future avenue of investigation.

5.5 Conclusion

We investigated out-of-plane spin polarization in all-in-plane magnetized spin valve structures. By flowing charge current through an in-plane ferromagnetic layer, the magnetic ordering breaks the in-plane symmetry and allows for spin currents with an out-of-plane polarization to exert a torque on a nearby second ferromagnetic layer and drive precession. What we found is that our angular ST-FMR results are well explained without considering this effect and by only considering the torque due to the Oersted field. This is supported by DC bias measurements where no signs of a sizable damping-like torque impacting the FMR linewidth are detected. We conclude that the out-of-plane spin polarization torque, if present, is no more than a few percent of the Oersted field in the CoFe/Cu/NiFe spin valve stack examined here.

We have presented a few reasons as to why this torque might not be present. Future measurements on different devices will be necessary to arrive at a convincing conclusion, particularly if this geometry is to be used for exciting easy-plane precession and superfluid-like spin transport. Future work could include repeating ST-FMR measurements on samples with decreased Cu thickness to promote more current flowing through the CoFe source layer. Additional measurements on samples with alternate source and sink layers (e.g. NiFe fixed and CoFe free layer) could provide evidence of the out-of-plane spin polarization torque since spin transfer efficiency in that system is known to be strong. Another option would be to change the source material to a material with higher spin-orbit coupling while still retaining in-plane magnetization. $L1_0$ ordered FePt with a (110)-orientation has been shown to exhibit two-fold in-plane magnetic anisotropy [191, 192], and Pt is a commonly used material for spin Hall effect measurements [78]. Additionally replacing the IrMn/CoFe bilayer with a single, highly conductive layer could help to simplify the material system.

Chapter 6

Conclusions and Future Outlook

6.1 Closing Remarks

In this dissertation, we introduced the idea of superfluid-like spin transport and how it can be used to provide a means of achieving long-distance spin information transport. This phenomenon has been proposed as an alternative to diffusive spin waves for beyond micron-scale information transport without significant losses. This dissertation has outlined steps that have been taken towards an experimental realization of this phenomenon using metallic ferromagnets that are compatible with industry standard thin film growth methods.

In Ch. 3 we discussed the development of an ultra-low damping, metallic alloy in the form of FeV. We showed that by doping Fe, an already low-damping metallic ferromagnet, with the non-magnetic dopant V, it is possible to lower not only the magnetic moment but also the intrinsic Gilbert damping. Conversely, introducing various amounts of Al, a lower Z number material than V, the intrinsic damping of the resulting alloy increased. This was attributed to a modification in the density of states at the Fermi level, with FeV observing a reduction and FeAl alloys an enhancement. This dependency on the density of states is consistent with conductivity-like damping (although there is also likely significant resistivity-like damping at room temperature) and supports the findings of other studies that have looked at damping in Fe-based alloys and the correlation with the density of states at the Fermi level.

Ch. 4 used these results as a foundation for the material system studied in the micromagnetic simulations. We utilized the material parameters from polycrystalline thin films of FeV as a basis for the simulated material. We demonstrated how one can understand the spiraling magnetization texture presented within superfluid-like spin transport as a train of interacting domain walls. By increasing the driving force of the domain wall, we were able to observe the transition from individual domain wall to that of a fluid-like entity. This transition was most evident in nanostrips with a notch defect introduced, whereby the domain wall train can be pinned when the driving force is small. With increasing driving force it is possible for the domain wall train to overcome the pinning when a critical density was exceeded, and the walls collectively showed fluid-like behaviors. This work contributes to our understanding of superfluid-like spin transport dynamics by using well-established domain wall physics to accurately explain the phenomena.

Finally, in Ch. 5 we proposed an alternative means to exciting superfluid-like spin transport dynamics. Instead of using current-perpendicular-to-plane nanopillars to achieve an out-of-plane spin-transfer-torque, we proposed using unconventional spin torques found in current-in-plane spin valves with broken in-plane symmetry. By flowing a charge current within the plane of the film, collinear with the magnetization direction, one can generate a spin current with the appropriate out-of-plane polarization needed to excite superfluid-like spin transport dynamics (i.e., easy-plane magnetic precession). We showed that in the CoFe/Cu/NiFe spin valve structures studied here, this effect is quite small, if present at all. This is in stark contrast with previous studies that were able to demonstrate switching of perpendicular magnetized layers using the same principle. If this excitation scheme is to be used, one

needs to choose the material system carefully in order to maximize the out-of-plane torque while also minimizing the processing costs of the system (i.e. no exotic materials, no single crystalline materials).

6.2 Future Work

If superfluid-like spin transport is to be used for carrying spin information, there is still a significant amount of work to be done. The next few paragraphs address various avenues of work that could be addressed.

Realistic micromagnetic simulations: Before more experimental work is done that focuses on experimentally realizing superfluid-like spin transport, it would be helpful to know how this phenomenon behaves in a more realistic system. Adding in grain boundaries, defects, imperfections, edge roughness, interfacial roughness of the layers that comprise a synthetic antiferromagnet, and thermal fluctuations would all contribute greatly to the community's understanding of SLST. An example of various micromagnetic simulations with some of these aspects is shown in Fig. 6.1.

Devising a detection scheme: Ch. 5 discusses an alternative method to *exciting* SLST dynamics, but nowhere is the *detection* of this phenomena discussed. It would be good to provide an idea or two and method how people can expand upon it. One potential method would be to measure the change in local resistance across a nanopillar as a result of the magnetization in the strip precessing. By using a reference layer and a spectrum analyzer, one could measure the oscillations in resistance from giant magnetoresistance. This could also be used to potentially measure the frequency of oscillations as a function of driving force as well as determine what the energy threshold is to overcome pinning of superfluid-like spin transport dynamics.

Device geometry: Current-perpendicular-to-plane nanopillars could be used for excitation and detection of superfluid-like spin transport. As an alternative, Ch. 5 introduces the idea of a current-in-plane geometry as a means of excitation. These two possible geometries are shown in Fig. 6.2a and Fig. 6.2b for the current-perpendicular-to-plane and current-in-plane options, respectively. The current-perpendicular-to-plane geometry offers the advantage of well established, albeit tricky and expensive, fabrication processes. The current-in-plane could potentially be easier to fabricate but the strength of the underlying physics used for excitation has yet to be determined.

Other materials: It is possible that the FeV alloys developed in Ch. 3 and used for the simulations in Ch. 4 are not the only materials possible of hosting SLST. While insulating ferrimagnets might have low damping parameters, their incompatibility with Si substrates rules them out. Other low damping metallic ferromagnets, such as $Co_{25}Fe_{75}$, could be investigated as material platforms. Additionally the damping parameters used in Ch. 4 are similar to that of $Ni_{80}Fe_{20}$ and CoFeB (commonly used in magnetic tunnel junctions), so ultralow

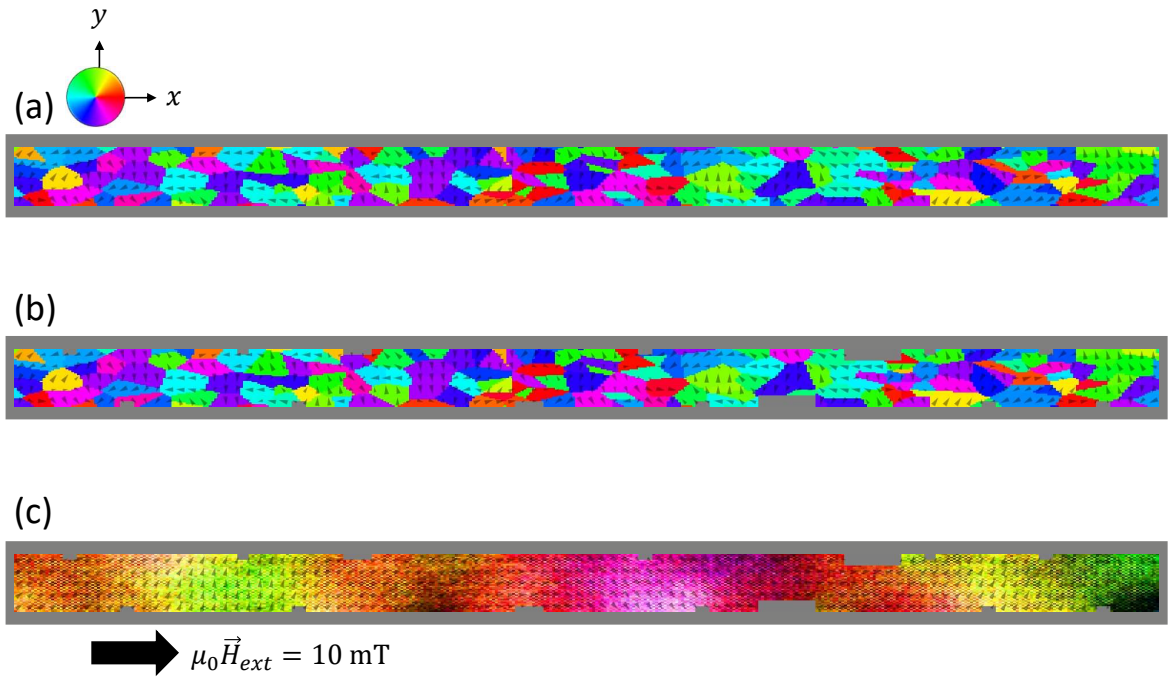


Figure 6.1: (a) Nanostrip with grains of average size 10 nm. The magnetization is uniform within each grain but randomly oriented. (b) Same as (a) but squares of various sizes have been removed from the edges at multiple points to simulate edge roughness. (c) Same as (b) with thermal fluctuations to simulate an equivalent temperature of $T = 300$ K and an externally applied magnetic field of $\mu_0 H_{ext} = 10$ mT along the $\hat{x}$ direction. The snapshot is taken after $t = 1$ ns of simulation time.

damping might not be a requirement. Understanding how robust superfluid-like spin transport is to variations in damping, saturation magnetization, magnetocrystalline anisotropy, etc. will be of great use.

Optimizing deposition and lithographic patterning: This step will likely be a more trial-and-error sort of project rather than a systematic study by tuning certain knobs. Minimizing interfacial diffusion and roughness, optimizing the interlayer exchange coupling between the two layers in the synthetic antiferromagnet, avoiding large edge defects during lithographic patterning, and more will be crucial to a physical realization of SLST. The result of the more realistic micromagnetic simulations will give an idea of how sensitive (or insensitive) SLST is these factors. Only time and more work will tell.

New class of oscillator based on easy-plane precession: While a full realization of superfluid-like spin transport might be some time away, there is a possibility to use easy-plane precession to improve a different avenue of spintronic devices: spin torque oscillators. Oscillators

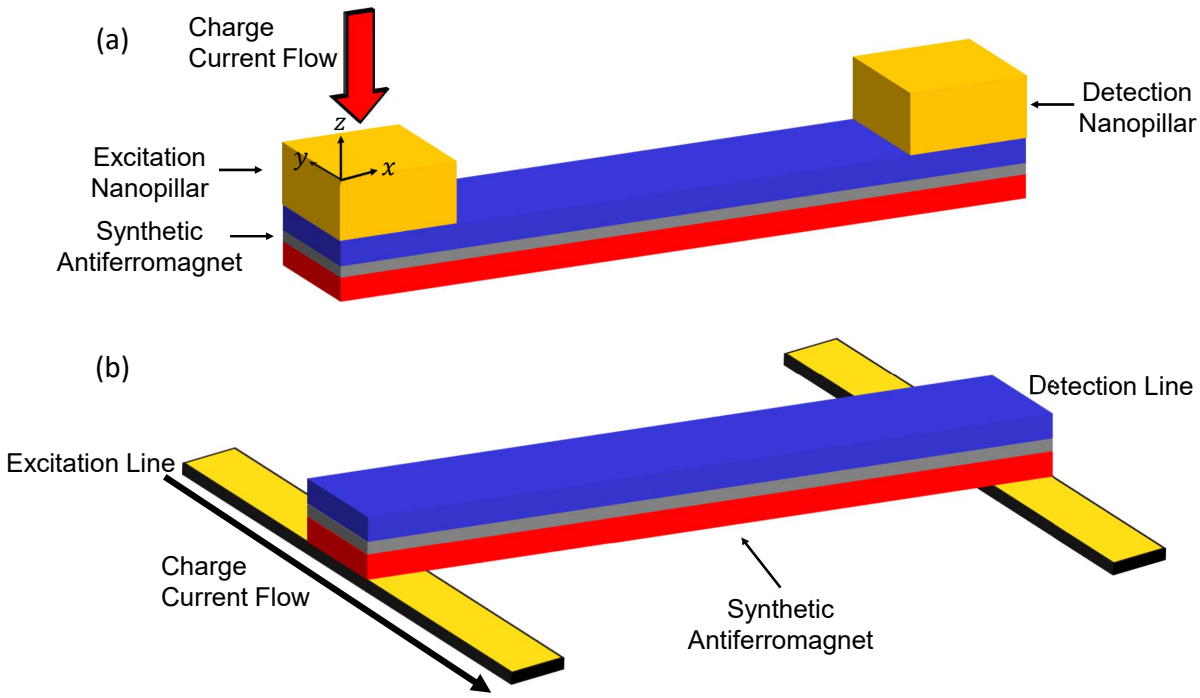


Figure 6.2: Two potential device geometries that could be used for a future experiment to measure superfluid-like spin transport. (a) Current-perpendicular-to-plane geometry with nanopillars. The excitation nanopillar contains a perpendicularly magnetized reference layer used to spin polarize the charge current. (b) Current-in-plane geometry where the excitation line could contain an in-plane magnetized layer that would generate out-of-plane spin polarized spin currents when an in-plane charge current is applied.

have been used as a form of high frequency signal generation but suffer from a number of drawbacks including low power output as a result of small cone angle precession, expensive and precise sub-micron lithography, low stability, and requirement of an external field to bias the magnetization. Easy-plane oscillators (e.g. Fig. 5.1b) could potentially replace these, offering increased power output, easier fabrication, and increased stability.

An experimental achievement of superfluid-like spin transport in metallic ferromagnets at room temperature could have the potential to revolutionize the future of spintronic devices. This phenomenon could offer a means of charge-less transport between two spin-based devices (e.g. spin logic gates) without the need for repeaters or amplifiers to boost the signal-to-noise ratio, thereby simplifying these devices. This could be a means of changing the spintronics landscape in a way that makes the field more industrially friendly and favorable as a means

of integration alongside existing and well-established CMOS devices.

Chapter 7

Additional Publications

This chapter lists additional publications I contributed to during my PhD.

Room-Temperature Intrinsic and Extrinsic Damping in Polycrystalline Fe Thin Films

Citation: Shuang Wu, **David A. Smith**, Prabandha Nakarmi, Anish Rai, Michael Clavel, Mantu K. Hudait, Jing Zhao, F. Marc Michel, Claudia Mewes, Tim Mewes, and Satoru Emori, *Physical Review B* **105**, 174408 (2022)

Abstract [22]: We examine room-temperature magnetic relaxation in polycrystalline Fe films. Out-of-plane ferromagnetic resonance measurements reveal Gilbert damping parameters of ≈ 0.0024 for Fe films with thicknesses of 4–25 nm, regardless of their microstructural properties. This observation runs counter to the intuition that various film defects heavily influence Gilbert damping. The remarkable invariance with film microstructure suggests that room-temperature intrinsic Gilbert damping in the Fe films is mostly fixed by the bcc crystal structure within the bulk of nanoscale grains, with limited impact from grain boundaries and film roughness. By contrast, the in-plane FMR linewidths of the Fe films exhibit distinct nonlinear frequency dependencies, indicating the presence of strong extrinsic damping. To fit our in-plane FMR data, we have used a grain-to-grain two-magnon scattering model with two types of correlation functions aimed at describing the spatial distribution of inhomogeneities in the film. However, neither of the two correlation functions is able to reproduce the experimental data quantitatively with physically reasonable parameters. Our findings advance the fundamental understanding of intrinsic Gilbert damping in structurally disordered films, while demonstrating the need for a deeper examination of how microstructural disorder governs extrinsic damping.

My contribution: In this study, we investigated the magnitude of extrinsic contributions to Gilbert damping in two different series of polycrystalline Fe films. Fe films were grown on Ti/Cu or Ti/Ag seed layers and exhibited differing structural and magnetic properties. Out-of-plane ferromagnetic resonance (FMR) was used to measure intrinsic Gilbert damping and showed relative insensitivity to the film microstructure. In-plane FMR however showed dominate contributions from two-magnon scattering in Ti/Cu, with large non-linear features present in the FMR linewidth vs. frequency plots. We found that a two-magnon scattering model cannot accurately reproduce the measured data with reasonable results. This suggests the need for further refinement of models that focus on extrinsic contributions to magnetic damping. I contributed to this study by growing the thin films and performing in-plane FMR measurements.

Element-Specific Detection of Sub-Nanosecond Spin-Transfer Torque in a Nanomagnet Ensemble

Citation: Satoru Emori, Christoph Klewe, Jan-Michael Schmalhorst, Jan Krieft, Padraic Shafer, Youngmin Lim, **David A. Smith**, Arjun Sapkota, Abhishek Srivastava, Claudia Mewes, Zijian Jiang, Behrouz Khodadadi, Hesham Elmkharram, Jean J. Heremans, Elke Arenholz, Günter Reiss, and Tim Mewes, *Nano Letters* **20**, 7828 (2020)

Abstract [112]: Spin currents can exert spin-transfer torques on magnetic systems even in the limit of vanishingly small net magnetization, as recently shown for antiferromagnets. Here, we experimentally show that a spin-transfer torque is operative in a macroscopic ensemble of weakly interacting, randomly magnetized Co nanomagnets. We employ element- and time-resolved X-ray ferromagnetic resonance (XFMR) spectroscopy to directly detect subnanosecond dynamics of the Co nanomagnets, excited into precession with cone angle $\gtrsim 0.003^\circ$ by an oscillating spin current. XFMR measurements reveal that as the net moment of the ensemble decreases, the strength of the spin-transfer torque increases relative to those of magnetic field torques. Our findings point to spin-transfer torque as an effective way to manipulate the state of nanomagnet ensembles at subnanosecond time scales.

My contribution: In this paper, we investigated how spin current can interact with an ensemble of nanomagnets and exert a torque on the magnetization when the global magnetization vector vanishes. Using a time- and element-resolved x-ray technique, we are able to observe the effect a spin current that originates in NiFe has on isolated Co magnetic moments embedded within a Cu matrix. I contributed to this study by assisting other members of my group with the data acquisition and analysis during our synchrotron beamtime experiments.

Conductivity-like Gilbert Damping due to Intraband Scattering in Epitaxial Iron

Citation: Behrouz Khodadadi, Anish Rai, Arjun Sapkota, Abhishek Srivastava, Bhuwan Nepal, Youngmin Lim, **David A. Smith**, Claudia Mewes, Sujan Budhathoki, Adam J. Hauser, Min Gao, Jie-Fang Li, Dwight D. Viehland, Zijian Jiang, Jean J. Heremans, Prasanna V. Balachandran, Tim Mewes, and Satoru Emori, *Physical Review Letters* **124**, 157201 (2020)

Abstract [1]: Confirming the origin of Gilbert damping by experiment has remained a challenge for many decades, even for simple ferromagnetic metals. Here, we experimentally identify Gilbert damping that increases with decreasing electronic scattering in epitaxial thin films of pure Fe. This observation of conductivitylike damping, which cannot be accounted for by classical eddy-current loss, is in excellent quantitative agreement with theoretical predictions of Gilbert damping due to intraband scattering. Our results resolve the long-standing question about a fundamental damping mechanism and offer hints for engineering

low-loss magnetic metals for cryogenic spintronics and quantum devices.

My contribution: In this study, we investigated the temperature dependence of intrinsic Gilbert damping in two epitaxial Fe systems. By growing Fe thin films on two different substrates, we were able to create two systems with differing degrees of crystallinity. We found that at low temperatures, the more disordered film exhibited lower damping than the cleaner, more ordered film. This study was the first to attribute the behavior of Gilbert damping to a dominate contribution from resistivity-like damping in Fe, the prototypical ferromagnet. I contributed to this study by assisting with the in-plane ferromagnetic resonance measurements and drafting of figures for the publication.

Current-Induced Spin-Orbit Field in Permalloy Interfaced with Ultrathin Ti and Cu

Citation: Ryan W. Greening, **David A. Smith**, Youngmin Lim, Zijian Jiang, Jesse Barber, Steven Dail, Jean J. Heremans, and Satoru Emori, *Applied Physics Letters* **116**, 052402 (2020)

Abstract [92]: How spin-orbit torques emerge from materials with weak spin-orbit coupling (e.g., light metals) is an open question in spintronics. Here, we report on a field-like spin-orbit torque (i.e., in-plane spin-orbit field transverse to the current axis) in SiO_2-sandwiched Permalloy (Py), with the top Py-SiO_2 interface incorporating ultrathin Ti or Cu. In both SiO_2/Py/Ti/SiO_2 and SiO_2/Py/Cu/SiO_2, this spin-orbit field opposes the classical Oersted field. While the magnitude of the spin-orbit field is at least a factor of 3 greater than the Oersted field, we do not observe evidence for a significant damping-like torque in SiO_2/Py/Ti/SiO_2 or SiO_2/Py/Cu/SiO_2. Our findings point to contributions from a Rashba-Edelstein effect or spin-orbit precession at the (Ti, Cu)-inserted interface.

My contribution: In this paper, we investigated the presence of a spin-orbit field in multilayer structures comprised of light metals. We used the planar Hall effect and spin torque ferromagnetic resonance to measure the field-like and damping-like torques present in this system. I contributed to this project by assisting the lead author with thin film growth and data acquisition of the spin torque ferromagnetic resonance.

Spin Decoherence Independent of Antiferromagnetic Order in IrMn

Citation: Behrouz Khodadadi, Youngmin Lim, **David A. Smith**, Ryan W. Greening, Yuankai Zheng, Zhitao Diao, Christian Kaiser, and Satoru Emori, *Physical Review B* **99**, 024435 (2019)

Abstract [87]: We investigate the impact of pinned antiferromagnetic order on the decoherence of spin current in polycrystalline IrMn. In NiFe/Cu/IrMn/CoFe multilayers, we coherently pump an electronic spin current from NiFe into IrMn, whose antiferromagnetic order is globally pinned by static exchange-bias coupling with CoFe. We observe no anisotropic spin decoherence with respect to the orientation of the pinned antiferromagnetic order. We also observe no difference in spin decoherence for samples with and without pinned antiferromagnetic order. Moreover, although there is a pronounced resonance linewidth increase in NiFe that coincides with the switching of IrMn/CoFe, we show that this is not indicative of anisotropic spin decoherence in IrMn. Our results demonstrate that the decoherence of electron-mediated spin current is remarkably insensitive to the magnetization state of the antiferromagnetic IrMn spin sink.

My contribution: In this paper, we investigated how the decoherence of an electron-mediated spin current depends on antiferromagnetic ordering. By exciting ferromagnetic resonance of NiFe, we were able to pump a spin current through a Cu spacer and into a IrMn/CoFe spin sink. We observe the effects that the relative orientation of the antiferromagnetic ordering in IrMn had on the measured damping parameter. We found that the amount of decoherence present in this system was independent of the relative orientation between the spin source magnetization and the antiferromagnetic ordering, as evident by the noted lack of anisotropy in the measured damping parameter. I contributed to this study by assisting with broadband ferromagnetic resonance measurements and drafting of various figures found within the publication.

Bibliography

[1] B. Khodadadi, A. Rai, A. Sapkota, A. Srivastava, B. Nepal, Y. Lim, D. A. Smith, C. Mewes, S. Budhathoki, A. J. Hauser, M. Gao, J.-F. Li, D. D. Viehland, Z. Jiang, J. J. Heremans, P. V. Balachandran, T. Mewes, and S. Emori, Physical Review Letters **124**, 157201 (2020).

[2] C. Scheck, L. Cheng, I. Barsukov, Z. Frait, and W. E. Bailey, Physical Review Letters **98**, 117601 (2007).

[3] S. Mankovsky, D. Ködderitzsch, G. Woltersdorf, and H. Ebert, Physical Review B **87**, 014430 (2013).

[4] I. E. Agency, *Gadgets and Gigawatts : Policies for Energy Efficient Electronics* (OECD Publishing, 2009) p. 424.

[5] J. Chow, R. J. Kopp, and P. R. Portney, Science **302**, 1528 (2003), https://www.science.org/doi/pdf/10.1126/science.1091939 .

[6] A. Hirohata, K. Yamada, Y. Nakatani, L. Prejbeanu, B. Diény, P. Pirro, and B. Hillebrands, Journal of Magnetism and Magnetic Materials , 166711 (2020).

[7] I. Zutic, J. Fabian, and S. Das Sarma, Reviews of Modern Physics **76**, 323 (2004).

[8] S. A. Wolf, D. D. Awschalom, R. A. Buhrman, J. M. Daughton, S. von Molnár, M. L. Roukes, A. Y. Chtchelkanova, and D. M. Treger, Science **294**, 1488 (2001).

[9] A. Fert and F. N. Van Dau, Comptes Rendus Physique **20**, 817 (2019), 1911.13118 .

[10] J. Lu and S. Wolf, in *Handbook of Nanomagnetism* (Pan Stanford, 2015) pp. 13–40.

[11] A. V. Chumak, V. I. Vasyuchka, A. A. Serga, and B. Hillebrands, Nature Physics **11**, 453 (2015).

[12] T. L. Gilbert, IEEE Transactions on Magnetics **40**, 3443 (2004).

[13] V. Kambersky, Czech. J. Phys. B. **26**, 1366 (1976).

[14] K. Gilmore, Y. U. Idzerda, and M. D. Stiles, Physical Review Letters **99**, 027204 (2007).

[15] K. Gilmore, Y. U. Idzerda, and M. D. Stiles, Journal of Applied Physics **103**, 07D303 (2008).

[16] H. Ebert, S. Mankovsky, D. Ködderitzsch, and P. J. Kelly, Physical Review Letters **107**, 066603 (2011).

[17] M. A. Schoen, D. Thonig, M. L. Schneider, T. J. Silva, H. T. Nembach, O. Eriksson, O. Karis, and J. M. Shaw, Nature Physics **12**, 839 (2016).

[18] C. Mewes and T. Mewes, in *Handbook of Nanomagnetism: Application and Tools* (Pan Stanford, Boca Raton, FL, 2015) pp. 71–96.

[19] K. Lenz, H. Wende, W. Kuch, K. Baberschke, K. Nagy, and A. Jánossy, Physical Review B **73**, 144424 (2006).

[20] R. Arias and D. L. Mills, Physical Review B **60**, 7395 (1999).

[21] R. D. McMichael, M. D. Stiles, P. J. Chen, and W. F. Egelhoff, Journal of Applied Physics **83**, 7037 (1998).

[22] S. Wu, D. A. Smith, P. Nakarmi, A. Rai, M. Clavel, M. K. Hudait, J. Zhao, F. M. Michel, C. Mewes, T. Mewes, and S. Emori, (2022), arXiv:2109.03684v2 .

[23] S. S. Kalarickal, P. Krivosik, J. Das, K. S. Kim, and C. E. Patton, Physical Review B **77**, 054427 (2008).

[24] J. Lindner, K. Lenz, E. Kosubek, K. Baberschke, D. Spoddig, R. Meckenstock, J. Pelzl, Z. Frait, and D. L. Mills, Physical Review B **68**, 060102(R) (2003).

[25] K. Zakeri, J. Lindner, I. Barsukov, R. Meckenstock, M. Farle, U. Von Hörsten, H. Wende, W. Keune, J. Rocker, S. S. Kalarickal, K. Lenz, W. Kuch, K. Baberschke, and Z. Frait, Physical Review B **76**, 104416 (2007).

[26] D. C. Ralph and M. D. Stiles, Journal of Magnetism and Magnetic Materials **320**, 1190 (2008).

[27] A. Brataas, A. D. Kent, and H. Ohno, Nature Materials **11**, 372 (2012).

[28] D. Houssameddine, U. Ebels, B. Dela, B. Rodmacq, I. Firastrau, F. Ponthenier, M. Brunet, C. Thirion, J.-p. Michel, L. Prejbeanu-buda, M.-c. Cyrille, O. Redon, and B. Dieny, Nature Materials **6**, 447 (2007).

[29] R. Cheng, D. Xiao, and A. Brataas, Physical Review Letters **116** (2016), 10.1103/PhysRevLett.116.207603.

[30] J. R. Chen, A. Smith, E. A. Montoya, J. G. Lu, and I. N. Krivorotov, Communications Physics **3**, 187 (2020).

[31] C. Tingsu, R. K. Dumas, A. Eklund, P. K. Muduli, A. Houshang, A. A. Awad, P. Durrenfeld, B. G. Malm, A. Rusu, and J. Akerman, Proceedings of the IEEE **104** (2016).

[32] H. Kubota, A. Fukushima, K. Yakushiji, T. Nagahama, S. Yuasa, K. Ando, H. Maehara, Y. Nagamine, K. Tsunekawa, D. D. Djayaprawira, N. Watanabe, and Y. Suzuki, Nature Physics **4**, 37 (2008).

[33] H. Kubota, A. Fukushima, K. Yakushiji, S. Yakata, S. Yuasa, K. Ando, M. Ogane, Y. Ando, and T. Miyazaki, Journal of Applied Physics **105**, 07D117 (2009).

[34] A. Hoffmann, IEEE Transactions on Magnetics **49**, 5172 (2013).

[35] J. Sinova, S. O. Valenzuela, J. Wunderlich, C. H. Back, and T. Jungwirth, Reviews of Modern Physics **87**, 1213 (2015).

[36] J. Ryu, S. Lee, K. J. Lee, and B. G. Park, Advanced Materials **1907148**, 1 (2020).

[37] A. Manchon, J. Železný, I. M. Miron, T. Jungwirth, J. Sinova, A. Thiaville, K. Garello, and P. Gambardella, Reviews of Modern Physics **91**, 035004 (2019).

[38] A. Davidson, V. P. Amin, W. S. Aljuaid, P. M. Haney, and X. Fan, Physics Letters, Section A: General, Atomic and Solid State Physics **384**, 126228 (2020), 1906.11772 .

[39] V. P. Amin, J. Zemen, and M. D. Stiles, Physical Review Letters **121** (2018), 10.1103/PhysRevLett.121.136805.

[40] V. P. Amin, P. M. Haney, and M. D. Stiles, Journal of Applied Physics **128**, 151101 (2020).

[41] Z. Zheng, Y. Zhang, V. Lopez-Dominguez, L. Sánchez-Tejerina, J. Shi, X. Feng, L. Chen, Z. Wang, Z. Zhang, K. Zhang, H. Bin, Y. Xu, Y. Zhang, M. Carpentieri, A. Fert, G. Finocchio, W. Zhao, . . Pedram, K. Amiri, and Y. . Zhang, Nature Communications **12**, 4555 (2021).

[42] D. MacNeill, G. M. Stiehl, M. H. D Guimaraes, R. A. Buhrman, J. Park, and D. C. Ralph, Nature Physics **13**, 300 (2017).

[43] S. H. C. Baek, V. P. Amin, Y. W. Oh, G. Go, S. J. Lee, G. H. Lee, K. J. Kim, M. D. Stiles, B. G. Park, and K. J. Lee, Nature Materials **17**, 509 (2018).

[44] M. Tang, K. Shen, S. Xu, H. Yang, S. Hu, W. Lü, C. Li, M. Li, Z. Yuan, S. J. Pennycook, K. Xia, A. Manchon, S. Zhou, X. Qiu, M. Tang, S. Xu, H. Yang, S. Hu, S. Zhou, X. Qiu, K. Shen, Z. Yuan, K. Xia, W. Lü, C. Li, M. Li, S. J. Pennycook, and A. Manchon, Advanced Materials **32**, 2002607 (2020).

[45] L. Zhu, D. C. Ralph, R. A. Buhrman, L. Zhu, D. C. Ralph, and R. A. Buhrman, Advanced Functional Materials , 2103898 (2021).

[46] F. Xue, C. Rohmann, J. Li, V. Amin, and P. Haney, Physical Review B **102**, 014401 (2020).

[47] L. Flacke, L. Liensberger, M. Althammer, H. Huebl, S. Geprägs, K. Schultheiss, A. Buzdakov, T. Hula, H. Schultheiss, E. R. J. Edwards, H. T. Nembach, J. M. Shaw, R. Gross, and M. Weiler, Applied Physics Letters **115**, 122402 (2019).

[48] R. Lebrun, A. Ross, S. A. Bender, A. Qaiumzadeh, L. Baldrati, J. Cramer, A. Brataas, R. A. Duine, and M. Kläui, Nature **561**, 222 (2018).

[49] B. L. Giles, Z. Yang, J. S. Jamison, and R. C. Myers, Physical Review B **92**, 224415 (2015).

[50] H. Chang, P. Li, W. Zhang, T. Liu, A. Hoffmann, L. Deng, and M. Wu, IEEE Magnetics Letters **5**, 6700104 (2014).

[51] S. Emori, D. Yi, S. Crossley, J. J. Wisser, P. P. Balakrishnan, B. Khodadadi, P. Shafer, C. Klewe, A. T. N'Diaye, B. T. Urwin, K. Mahalingam, B. M. Howe, H. Y. Hwang, E. Arenholz, and Y. Suzuki, Nano Letters **18**, 4273 (2018).

[52] M. A. Schoen, J. Lucassen, H. T. Nembach, B. Koopmans, T. J. Silva, C. H. Back, and J. M. Shaw, Physical Review B **95**, 134411 (2017).

[53] M. A. Schoen, J. Lucassen, H. T. Nembach, T. J. Silva, B. Koopmans, C. H. Back, and J. M. Shaw, Physical Review B **95**, 134410 (2017).

[54] H. K. Lee, I. Barsukov, A. G. Swartz, B. Kim, L. Yang, H. Y. Hwang, and I. N. Krivorotov, AIP Advances **6**, 055212 (2016).

[55] E. B. Sonin, Advances in Physics **59**, 181 (2010).

[56] E. B. Sonin, Physical Review B **99**, 104423 (2019).

[57] E. Iacocca and M. A. Hoefer, Physical Review B **95**, 134409 (2017).

[58] E. Iacocca, T. J. Silva, and M. A. Hoefer, Physical Review Letters **118**, 017203 (2017).

[59] E. Iacocca and M. A. Hoefer, Physical Review B **99**, 184402 (2019).

[60] E. Iacocca, Physical Review B **102**, 224403 (2020).

[61] S. Takei, B. I. Halperin, A. Yacoby, and Y. Tserkovnyak, Physical Review B **90**, 94408 (2014).

[62] Y. Tserkovnyak, Journal of Applied Physics **124**, 190901 (2018).

[63] S. Takei and Y. Tserkovnyak, Physical Review Letters **112**, 227201 (2014).

[64] B. T. Matthias, T. H. Geballe, and V. B. Compton, Rev. Mod. Phys. **35**, 1 (1963).

[65] T. Fujita, Progress of Theoretical Physics **53**, 1219 (1975).

[66] B. I. Halperin and P. C. Hohenberg, Physical Review **188**, 898 (1969).

[67] H. Skarsvåg, C. Holmqvist, and A. Brataas, Physical Review Letters **115**, 237201 (2015).

[68] R. A. Duine, K. J. Lee, S. S. Parkin, and M. D. Stiles, Nature Physics **14**, 217 (2018).

[69] P. Stepanov, S. Che, D. Shcherbakov, J. Yang, R. Chen, K. Thilahar, G. Voigt, M. W. Bockrath, D. Smirnov, K. Watanabe, T. Taniguchi, R. K. Lake, Y. Barlas, A. H. MacDonald, and C. N. Lau, Nature Physics **14**, 907 (2018).

[70] W. Yuan, Q. Zhu, T. Su, Y. Yao, W. Xing, Y. Chen, Y. Ma, X. Lin, J. Shi, R. Shindou, X. C. Xie, and W. Han, Science Advances **4**, eaat1098 (2018).

[71] E. Iacocca and M. A. Hoefer, Physics Letters, Section A: General, Atomic and Solid State Physics **383**, 125858 (2019), 1909.05756 .

[72] C. Kittel, Physical Review **73**, 155 (1948).

[73] B. Heinrich and J. A. C. Bland, in *Ultrathin Magnetic Structures II* (Springer-Verlag Berlin Heidelberg, 1994) Chap. 3, pp. 195–222.

[74] E. Montoya, *Spin Pumping and Spin Transport in Magnetic Heterostructures*, Ph.D. thesis, Simon Fraser Univeristy (2016).

[75] L. Liu, *Manipulation of Magnetic Moment Using the Spin Current From Magnetic and Non-magnetic Materials*, Ph.D. thesis, Cornell University (2012).

[76] M. Farle, Reports on Progress in Physics **61**, 755 (1998).

[77] R. D. McMichael and P. Krivosik, IEEE Transactions on Magnetics **40**, 2 (2004).

[78] L. Liu, T. Moriyama, D. C. Ralph, and R. A. Buhrman, Physical Review Letters **106**, 036601 (2011).

[79] C. He, A. Razavi, J. Wei, H. Xu, G. Yu, K. L. Wong, H. Wu, S. Shen, Q. Chen, Z. Zeng, S. Wang, and K. L. Wang, Applied Physics Letters **117**, 172406 (2020).

[80] A. Bose, D. D. Lam, S. Bhuktare, S. Dutta, H. Singh, Y. Jibiki, M. Goto, S. Miwa, and A. A. Tulapurkar, Physical Review Applied **9**, 064026 (2018).

[81] C. Safranski, J. Z. Sun, J.-W. Xu, and A. D. Kent, Physical Review Letters **124**, 197204 (2020).

[82] T. McGuire and R. Potter, IEEE Transactions on Magnetics **11**, 1018 (1975).

[83] S. Karimeddiny and D. C. Ralph, Physical Review Applied **15**, 064017 (2021).

[84] S. Iihama, T. Taniguich, K. Yakushiji, A. Fukushima, Y. Shiota, S. Tsunegi, R. Hiramatsu, S. Yuasa, Y. Suzuki, and H. Kubota, Nature Electronics **1**, 120 (2018).

[85] J. Wei, C. He, X. Wang, H. Xu, Y. Liu, Y. Guang, C. Wan, J. Feng, G. Yu, and X. Han, Physical Review Applied **13**, 34041 (2020).

[86] J. Nogués and I. K. Schuller, Journal of Magnetism and Magnetic Materials **192**, 203 (1999).

[87] B. Khodadadi, Y. Lim, D. A. Smith, R. W. Greening, Y. Zheng, Z. Diao, C. Kaiser, and S. Emori, Physical Review B **99** (2019), 10.1103/PhysRevB.99.024435.

[88] R. F. C. Farrow, D. Weller, R. F. Marks, M. F. Toney, D. J. Smith, and M. R. Mccartney, Journal of Applied Physics **84**, 934 (1998).

[89] A. Hirohata, H. Kurebayashi, S. Okamura, M. Kikuchi, T. Masaki, T. Nozaki, N. Tezuka, and K. Inomata, Journal of Applied Physics **97**, 103714 (2005).

[90] J. Wang, C. Dong, Y. Wei, X. Lin, B. Athey, Y. Chen, A. Winter, G. M. Stephen, D. Heiman, Y. He, H. Chen, X. Liang, C. Yu, Y. Zhang, E. J. Podlaha-Murphy, M. Zhu, X. Wang, J. Ni, M. McConney, J. Jones, M. Page, K. Mahalingam, and N. X. Sun, Physical Review Applied **12**, 034011 (2019).

[91] I. Kim, J. Kim, K. Kim, and M. Yamaguchi, IEEE Transactions on Magnetics **40**, 2706 (2004).

[92] R. W. Greening, D. A. Smith, Y. Lim, Z. Jiang, J. Barber, S. Dail, J. J. Heremans, and S. Emori, Applied Physics Letters **116**, 052402 (2020).

[93] G. V. Hansson, H. H. Radamsson, and W.-X. Ni, Journal of Materials Science: Materials in Electronics **6**, 292 (1995).

[94] M. Futamoto, M. Nakamura, M. Ohtake, N. Inaba, and T. Shimotsu, AIP Advances **6**, 085302 (2016).

[95] F. T. Vüllers and R. Spolenak, Thin Solid Films **577**, 26 (2015).

[96] E. Chason and T. M. Mayer, Critical Reviews in Solid State and Materials Sciences **22**, 1 (1997), https://doi.org/10.1080/10408439708241258 .

[97] A. Braslau, M. Deutsch, P. S. Pershan, A. H. Weiss, J. Als-Nielsen, and J. Bohr, Physical Review Letters **54**, 114 (1985).

[98] H. L. Wang, C. H. Du, Y. Pu, R. Adur, P. C. Hammel, and F. Y. Yang, Physical Review Letters **112**, 197201 (2014).

[99] I. Stabrawa, A. Kubala-Kukuś, D. Banaś, G. Pepponi, J. Braziewicz, M. Pajek, and M. Teodorczyk, Thin Solid Films **671**, 103 (2019).

[100] A. Gibaud and S. Hazra, Current Science **78**, 1467 (2000).

[101] J. M. Jensen, A. B. Oelkers, R. Toivola, D. C. Johnson, J. W. Elam, and S. M. George, Chemical Materials **14**, 2276 (2002).

[102] S. Singh, M. Swain, and S. Basu, Progress in Materials Science **96**, 1 (2018).

[103] M. Bj'orck and G. Andersson, Journal of Applied Crystallography **40** (2007).

[104] G. Vignaud and A. Gibaud, Journal of Applied Crystallography **52**, 201 (2019).

[105] Y. Hibino, K. Yakushiji, A. Fukushima, H. Kubota, and S. Yuasa, Physical Review B **101**, 174441 (2020).

[106] D. A. Smith, A. Rai, Y. Lim, T. Q. Hartnett, A. Sapkota, A. Srivastava, C. Mewes, Z. Jiang, M. Clavel, M. K. Hudait, D. D. Viehland, J. J. Heremans, P. V. Balachandran, T. Mewes, and S. Emori, Physical Review Applied **14**, 034042 (2020).

[107] J. Z. Sun, Physical Review B **62**, 570 (2000).

[108] T. Weindler, H. G. Bauer, R. Islinger, B. Boehm, J. Y. Chauleau, and C. H. Back, Physical Review Letters **113**, 237204 (2014).

[109] A. Mougin, M. Cormier, J. P. Adam, P. J. Metaxas, and J. Ferré, Europhysics Letters **78**, 57007 (2007).

[110] J. Han, P. Zhang, J. T. Hou, S. A. Siddiqui, and L. Liu, Science **366**, 1121 (2019).

[111] J. C. Slonczewski, Journal of Magnetism and Magnetic Materials **247**, 324 (2002).

[112] S. Emori, C. Klewe, J.-M. Schmalhorst, J. Krieft, P. Shafer, Y. Lim, D. A. Smith, A. Sapkota, A. Srivastava, C. Mewes, Z. Jiang, B. Khodadadi, H. Elmkharram, J. J. Heremans, E. Arenholz, G. Reiss, and T. Mewes, Nano Letters **20**, 7828 (2020).

[113] L. J. Cornelissen, J. Liu, R. A. Duine, J. B. Youssef, and B. J. Van Wees, Nature Physics **11**, 1022 (2015).

[114] M. Oogane, T. Wakitani, S. Yakata, R. Yilgin, Y. Ando, A. Sakuma, and T. Miyazaki, Japanese Journal of Applied Physics **45**, 3889 (2006).

[115] A. J. Lee, J. T. Brangham, Y. Cheng, S. P. White, W. T. Ruane, B. D. Esser, D. W. McComb, P. C. Hammel, and F. Yang, Nature Communications **8**, 234 (2017).

[116] P. He, X. Ma, J. W. Zhang, H. B. Zhao, G. Lüpke, Z. Shi, and S. M. Zhou, Physical Review Letters **110**, 077203 (2013).

[117] J.-M. L. Beaujour, A. D. Kent, D. W. Abraham, and J. Z. Sun, Journal of Applied Physics **103**, 07B519 (2008).

[118] T. Devolder, T. Tahmasebi, S. Eimer, T. Hauet, and S. Andrieu, Applied Physics Letters **103**, 242410 (2013).

[119] I. Barsukov, S. Mankovsky, A. Rubacheva, R. Meckenstock, D. Spoddig, J. Lindner, N. Melnichak, B. Krumme, S. I. Makarov, H. Wende, H. Ebert, and M. Farle, Physical Review B **84**, 180405(R) (2011).

[120] I. Kanada, A. Cruce, T. Mewes, S. Wu, C. Mewes, G. Mankey, and T. Suzuki, AIP Advances **7**, 056105 (2017).

[121] G. Woltersdorf and B. Heinrich, Physical Review B **69**, 184417 (2004).

[122] S. Emori, U. S. Alaan, M. T. Gray, V. Sluka, Y. Chen, A. D. Kent, and Y. Suzuki, Physical Review B **94**, 224423 (2016).

[123] W. K. Peria, T. A. Peterson, A. P. Mcfadden, T. Qu, C. Liu, C. J. Palmstrøm, and P. A. Crowell, Physical Review B **101**, 134430 (2020).

[124] M. Rickart, B. F. Roos, T. Mewes, J. Jorzick, S. O. Demokritov, and B. Hillebrands, Surface Science **495**, 68 (2001).

[125] L. Chen, S. Mankovsky, S. Wimmer, M. A. W. Schoen, H. S. Körner, M. Kronseder, D. Schuh, D. Bougeard, H. Ebert, D. Weiss, and C. H. Back, Nature Physics (2018), 10.1038/s41567-018-0053-8.

[126] C. Scheck, L. Cheng, and W. E. Bailey, Applied Physics Letters **88**, 252510 (2006).

[127] T. Usami, M. Itoh, and T. Taniyama, Applied Physics Letters **115**, 142403 (2019).

[128] B. Heinrich, in *Ultrathin Magnetic Structures III* (Springer-Verlag, Berlin/Heidelberg, 2005) pp. 143–210.

[129] R. D. McMichael, Journal of Applied Physics **103**, 07B114 (2008).

[130] J. M. Lock, British Journal of Applied Physics **17**, 1645 (1966).

[131] M. A. W. Schoen, J. M. Shaw, H. T. Nembach, M. Weiler, and T. J. Silva, Physical Review B **92**, 184417 (2015).

[132] S. Mizukami, D. Watanabe, M. Oogane, Y. Ando, Y. Miura, M. Shirai, and T. Miyazaki, Journal of Applied Physics **105**, 07D306 (2009).

[133] P. Dürrenfeld, F. Gerhard, J. Chico, R. K. Dumas, M. Ranjbar, A. Bergman, L. Bergqvist, A. Delin, C. Gould, L. W. Molenkamp, and J. Akerman, PHYSICAL REVIEW B **92**, 214424 (2015).

[134] C. Guillemard, S. Petit-Watelot, L. Pasquier, D. Pierre, J. Ghanbaja, J.-C. Rojas-Sánchez, A. Bataille, J. Rault, P. Le Fèvre, F. Bertran, and S. Andrieu, Physical Review Applied **11**, 064009 (2019).

[135] E. R. Edwards, H. T. Nembach, and J. M. Shaw, Physical Review Applied **11**, 054036 (2019).

[136] A. Conca, T. Nakano, T. Meyer, Y. Ando, and B. Hillebrands, Journal of Applied Physics **122**, 073902 (2017).

[137] J. M. Shaw, H. T. Nembach, T. J. Silva, and C. T. Boone, Journal of Applied Physics **114**, 243906 (2013).

[138] C. Liu, C. K. Mewes, M. Chshiev, T. Mewes, and W. H. Butler, Applied Physics Letters **95**, 022509 (2009).

[139] S. J. Xu, J. Y. Shi, Y. S. Hou, Z. Zheng, H. B. Zhao, R. Q. Wu, S. M. Zhou, Z. Shi, and W. J. Fan, Physical Review B **100**, 024403 (2019).

[140] M. Oogane, T. Kubota, Y. Kota, S. Mizukami, H. Naganuma, A. Sakuma, and Y. Ando, Applied Physics Letters **96**, 252501 (2010).

[141] P. Giannozzi, S. Baroni, N. Bonini, M. Calandra, R. Car, C. Cavazzoni, D. Ceresoli, G. L. Chiarotti, M. Cococcioni, I. Dabo, A. Dal Corso, S. De Gironcoli, S. Fabris, G. Fratesi, R. Gebauer, U. Gerstmann, C. Gougoussis, A. Kokalj, M. Lazzeri, L. Martin-Samos, N. Marzari, F. Mauri, R. Mazzarello, S. Paolini, A. Pasquarello, L. Paulatto, C. Sbraccia, S. Scandolo, G. Sclauzero, A. P. Seitsonen, A. Smogunov, P. Umari, and R. M. Wentzcovitch, Journal of Physics: Condensed Matter **21**, 395502 (2009).

[142] J. P. Perdew, A. Ruzsinszky, G. I. Csonka, O. A. Vydrov, G. E. Scuseria, L. A. Constantin, X. Zhou, and K. Burke, Physical Review Letters **100**, 136406 (2008).

[143] D. Vanderbilt, Physical Review B **41**, 7892 (1990).

[144] H. J. Monkhorst and J. D. Pack, Physical Review B **13**, 5188 (1976).

[145] A. Dal Corso, Computational Materials Science **95**, 337 (2014).

[146] K. Okhotnikov, T. Charpentier, and S. Cadars, Journal of Cheminformatics **8**, 1 (2016).

[147] D. A. Smith, S. Takei, B. Brann, L. Compton, F. Ramos-Diaz, M. J. Simmers, and S. Emori, Physical Review Applied **16**, 054002 (2021).

[148] D. Sander, S. O. Valenzuela, D. Makarov, C. H. Marrows, E. E. Fullerton, P. Fischer, J. McCord, P. Vavassori, S. Mangin, P. Pirro, B. Hillebrands, A. D. Kent, T. Jungwirth, O. Gutfleisch, C. G. Kim, and A. Berger, Journal of Physics D: Applied Physics **50**, 363001 (2017).

[149] H. Chen, A. D. Kent, A. H. Macdonald, and I. Sodemann, Physical Review B **90**, 220401(R) (2014).

[150] E. Iacocca, T. J. Silva, and M. A. Hoefer, Physical Review B **96**, 134434 (2017).

[151] T. Schneider, D. Hill, A. Kákay, K. Lenz, J. Lindner, J. Fassbender, P. Upadhyaya, Y. Liu, K. Wang, Y. Tserkovnyak, I. N. Krivorotov, and I. Barsukov, Physical Review B **103**, 144412 (2021).

[152] J. C. Slonczewski, Journal of Magnetism and Magnetic Materials **159**, L1 (1996).

[153] K. Kim, S. Takei, and Y. Tserkovnyak, Physical Review B **93**, 020402(R) (2016).

[154] J. König, M. C. Bønsager, and A. H. Macdonald, Physical Review Letters **87**, 187202 (2001).

[155] S. K. Kim and Y. Tserkovnyak, Physical Review Letters **119**, 047202 (2017).

[156] A. Vansteenkiste, J. Leliaert, M. Dvornik, M. Helsen, F. Garcia-Sanchez, and B. Van Waeyenberge, AIP Advances **4**, 107133 (2014).

[157] G. S. D. Beach, C. Nistor, C. Knutson, M. Tsoi, and J. L. Erskine, Nature Materials **4**, 741 (2005).

[158] S. Lepadatu, H. Saarikoski, R. Beacham, M. J. Benitez, T. A. Moore, G. Burnell, S. Sugimoto, D. Yesudas, M. C. Wheeler, J. Miguel, S. S. Dhesi, D. McGrouther, S. McVitie, G. Tatara, and C. H. Marrows, Scientific Reports **7**, 1640 (2017).

[159] F. S. Ma, H. S. Lim, Z. K. Wang, S. N. Piramanayagam, S. C. Ng, and M. H. Kuok, Applied Physics Letters **98**, 153107 (2011).

[160] K. Niitsu, Journal of Physics D: Applied Physics **53**, 39LT01 (2020).

[161] A. J. Berger, E. R. J. Edwards, H. T. Nembach, O. Karis, M. Weiler, and T. J. Silva, Physical Review B **98**, 24402 (2018).

[162] A. Ghosh, S. Auffret, U. Ebels, and W. E. Bailey, Physical Review Letters **109**, 127202 (2012).

[163] Y. Lim, B. Khodadadi, J.-F. Li, D. Viehland, A. Manchon, and S. Emori, Physical Review B **103**, 024443 (2021).

[164] E. Saitoh, H. Miyajima, T. Yamaoka, and G. Tatara, Nature **432**, 203 (2004).

[165] B. Kruger, Journal of Physics: Condensed Matter **24**, 024209 (2012).

[166] Y. Jang, S. R. Bowden, M. Mascaro, J. Unguris, and C. A. Ross, Applied Physics Letters **100**, 062407 (2012).

[167] S. Dutta, S. A. Siddiqui, J. A. Currivan-Incorvia, C. A. Ross, and M. A. Baldo, AIP Advances **5**, 127206 (2015).

[168] S. S. P. Parkin, M. Hayashi, and L. Thomas, Science **320**, 190 (2008).

[169] L. Caretta, S.-H. Oh, T. Fakhrul, D.-K. Lee, B. H. Lee, K. Kim, C. A. Ross, K.-J. Lee, and G. S. D. Beach, Science **370**, 1438 (2020).

[170] M. Yan, C. Andreas, A. Kákay, F. García-Sánchez, and R. Hertel, Applied Physics Letters **99**, 122505 (2011).

[171] M. Arora, E. K. Delczeg-Czirjak, G. Riley, T. J. Silva, H. T. Nembach, O. Eriksson, and J. M. Shaw, Physical Review Applied **15**, 054031 (2021).

[172] C. Safranski, E. A. Montoya, and I. N. Krivorotov, Nature Nanotechnology **14**, 27 (2019).

[173] M. Aoki, E. Shigematsu, M. Matsushima, R. Ohshima, S. Honda, T. Shinjo, M. Shiraishi, and Y. Ando, Physical Review B **102**, 174442 (2020).

[174] S. Q. Zheng, K. K. Meng, Q. B. Liu, J. K. Chen, J. Miao, X. G. Xu, and Y. Jiang, Applied Physics Letters **117**, 242403 (2020).

[175] A. van den Brink, G. Vermijs, A. Solignac, J. Koo, J. T. Kohlhepp, H. J. M. Swagten, and B. Koopmans, Nature Communications **7**, 10854 (2016).

[176] V. P. Amin and M. D. Stiles, Physical Review B **94**, 104419 (2016).

[177] A. M. Humphries, T. Wang, E. R. J. Edwards, S. R. Allen, J. M. Shaw, H. T. Nembach, J. Q. Xiao, T. J. Silva, and X. Fan, Nature Communications **8**, 911 (2017).

[178] T. Wang, S. Lendinez, M. B. Jungfleisch, J. Kolodzey, J. Q. Xiao, and X. Fan, Applied Physics Letters **116**, 012404 (2020).

[179] D. MacNeill, G. M. Stiehl, M. H. D. Guimarães, N. D. Reynolds, R. A. Buhrman, and D. C. Ralph, Physical Review B **96**, 054450 (2017).

[180] G. M. Stiehl, R. Li, V. Gupta, I. E. Baggari, S. Jiang, H. Xie, L. F. Kourkoutis, K. F. Mak, J. Shan, R. A. Buhrman, and D. C. Ralph, Physical Review B **100**, 184402 (2019).

[181] G. M. Stiehl, D. Macneill, N. Sivadas, I. E. Baggari, M. H. D. Guimarã, N. D. Reynolds, L. F. Kourkoutis, C. J. Fennie, R. A. Buhrman, and D. C. Ralph, ACS Nano **13**, 2599 (2019).

[182] J. Zhou, X. Shu, Y. Liu, X. Wang, W. Lin, S. Chen, L. Liu, Q. Xie, T. Hong, P. Yang, B. Yan, X. Han, and J. Chen, Physical Review B **101**, 184403 (2020).

[183] Y. Liu, I. Barsukov, Y. Barlas, I. N. Krivorotov, and R. K. Lake, Applied Physics Letters **116**, 132409 (2020).

[184] H. Zhou, X. Fan, L. Ma, Q. Zhang, L. Cui, S. Zhou, Y. S. Gui, C.-M. Hu, and D. Xue, Physical Review B **94**, 134421 (2016).

[185] O. Mosendz, J. E. Pearson, F. Y. Fradin, G. E. W. Bauer, S. D. Bader, and A. Hoffmann, Physical Review Letters **104**, 046601 (2010).

[186] J.-M. Kim, D.-J. Kim, C.-Y. Cheon, K.-W. Moon, C. Kim, C. Van, J.-R. Jeong, C. Hwang, K.-J. Lee, and B.-G. Park, Nano Letters **20**, 7803 (2020).

[187] C. Sun, S. M. Rafi-Ul-Islam, H. Yang, and M. B. A. Jalil, Physical Review B **102**, 214419 (2020).

[188] T. Nan, S. Emori, C. T. Boone, X. Wang, T. M. Oxholm, J. G. Jones, B. M. Howe, G. J. Brown, and N. X. Sun, Physical Review B **91**, 214416 (2015).

[189] P. Li, L. J. Riddiford, C. Bi, J. J. Wisser, X.-Q. Sun, A. Vailionis, M. J. Veit, A. Altman, X. Li, M. Dc, S. X. Wang, Y. Suzuki, and S. Emori, Physical Review Materials **5**, 064404 (2021).

[190] Q. Hao, W. Chen, and G. Xiao, Applied Physics Letters **106** (2015), 10.1063/1.4919867.

[191] D. E. Laughlin, K. Srinivasan, M. Tanase, and L. Wang, Scripta Materialia **53**, 383 (2005).

[192] T. Seki, S. Iihama, T. Taniguchi, and K. Takanashi, Physical Review B **100**, 144427 (2019).

[193] F. Yang and P. C. Hammel, Journal of Physics D: Applied Physics **51** (2018), 10.7868/s0207352816010200.

[194] M. Donahue, "Oommf user's guide, version 1.0," (1999).

Appendices

Appendix A

Micromagnetics Using Mumax

This appendix outlines how Mumax^3 code, an open-source GPU-accelerated micromagnetics package, was used to simulate superfluid-like spin transport. A walkthrough of the major sections of the program will be shown and advice will be given. This advice is meant to complement the existing resources, which include but are not limited to: the Mumax^3 paper [156], the Mumax^3 API (link) and the Mumax^3 workshop that was hosted by the Online Spintronics Seminar Series (link). Finally, a few lines of Python code will be shown that allows one to extract data stored within Mumax^3 output files and manipulate them to determine various quantities of interest.

A.1 Running Simulations Using Mumax3

Mumax^3 simulations are run using the command prompt/powershell in Windows or the terminal in Linux/Unix-based systems. Scripts are written using one's favorite text editor in Go, a language that is similar to C. These scripts are used as the inputs for the Mumax^3 executable. The simulation results are output to a directory with the same name as the input file unless otherwise specified. If a directory already exists with the same name, the data within that folder will be overwritten when the script is run, so be sure to change the name or location of previous simulations if you want to save them.

A.2 Simulating Superfluid-like Spin Transport

This section contains snippets of the code used to simulate superfluid-like spin transport (SLST) in perfect and notched nanostrips discussed in Ch. 4.

The first step is to define the total simulation space that the mesh will be partitioned into. Mumax^3 does this by breaking up the defined space into cells of uniform size. This can either be done by defining the total number of cells or the individual cell size. Listing 1 uses the former method to create a space that has dimensions of 2000 nm $\times$ 100 nm $\times$ 4 nm and breaks that up into 800 cells long by 40 cells wide by 2 cells thick. Mumax^3 uses SI units and centers all objects at the origin. This results in a cell size that is $2.5 \times 2.5 \times 2$ nm^3. It is crucial that the cell size is less than that of the exchange length ($l_{ex} = \sqrt{2A_{ex}/\mu_0 M_{sat}^2}$) as cells larger than this characteristic length can wash out important features (e.g. domain walls). It is also important to not have the cell size too small as simulation time increases exponentially with increasing cell count.

After defining the simulation space and mesh, that volume needs to be filled with our sample. Listing 2 shows the individual cuboids used to create the top and bottom layers of the synthetic antiferromagnet; the spacer layer was not explicitly modeled in this simulation since its thickness should be much less than that of the ferromagnetic layers and the exchange interaction between these two layers can be modeled using a built-in extension (see Listing 3).

```
// Simulate a spin superfluid (SSF) in a two FM films with AFM coupling
// to create a synthetic antiferromagnet. Due to the small thickness,
// the spacer layer is not explicitly modeled in this simulation. The
// material parameters mimic that of 2 nm thick poly-FeV.

// Author: David A. Smith

// Set up sample dimensions and grid
sizeX := 2000e-9 // Sample 2000 nm long
sizeY := 100e-9 // 100 nm wide
sizeZ := 4e-9 // 4 nm thick (each layer is 2 nm thick)

// Define number of cells
Nx := 800
Ny := 40
Nz := 2
```

Listing 1: Definition of the sample size and number of cells. This indirectly defines the cell size.

The two FM layers are identical in their shape, size, and individual parts that make them up. We define a distinct region in each layer that is used for applying the charge current excitation (the injector region) and move it to the far left side of the simulation space. The channel, where spin information is transported from one end to the other, comprises the largest part of the simulation space. A spin sink region is created at the far right to simulate spin pumping out of the strip. A fourth region, termed the super sink, is introduced to suppress reflections of any incoming spin waves and placed to the right of the sink. These regions are all added together to create the perfect nanostrip.

To create the notched nanostrip, we need to define a pair of triangular notches to remove from the simulation space. This is done by creating a cuboid, rotating it 45° about the $\hat{z}$ axis, translating it up/down such that the edge of the channel bisects the now-diamond shape, and removing that resulting triangle from the channel. This process is shown in Listing 4. Regions are then defined and then the final shape of the notched nanostrips is constructed by subtracting the notches.

Now that the overall simulation space and sample shape is defined, we can begin to define the material parameters of our sample. Here they were defined region by region using the "setregion" command, so as to ensure they can be easily modified in the future, but they can also be defined globally by simply declaring the variable value. The material parameters

```
22
23 // Define geometry for film
24 a := Cuboid(100e-9,100e-9,2e-9).transl(-950e-9,0,1e-9) // Injector
25 b := Cuboid(1800e-9,100e-9,2e-9).transl(0,0,1e-9) // Channel
26 c := Cuboid(80e-9,100e-9,2e-9).transl(940e-9,0,1e-9) // Sink
27 d := Cuboid(20e-9,100e-9,2e-9).transl(990e-9,0,1e-9)
28 // ^ "Super" sink (to suppress back scattering of incoming spin waves)
29
30 e := Cuboid(100e-9,100e-9,2e-9).transl(-950e-9,0,-1e-9) // Injector
31 f := Cuboid(1800e-9,100e-9,2e-9).transl(0,0,-1e-9) // Channel
32 g := Cuboid(80e-9,100e-9,2e-9).transl(940e-9,0,-1e-9) // Sink
33 h := Cuboid(20e-9,100e-9,2e-9).transl(990e-9,0,-1e-9)
34 // ^ "Super" sink
35
```

Listing 2: Define the shape of the individual regions that make up the synthetic antiferromagnet.

defined here are the saturation magnetization M_{sat}, the exchange coupling strength A_{ex}, and the Gilbert damping parameter α. $M_{sat} = 720$ kA/m and $A_{ex} = 20$ pJ/m are uniform throughout the sample, but α changes depending on the region: in the channel $\alpha_{chn} = 0.006$; in the injector/sink $\alpha_{inj} = \alpha_{snk} = \alpha_{chn} + \alpha' = 0.021$ where $\alpha' = 0.015$ is a damping enhancement term meant to simulate the effects of spin pumping into and out of a strip [163, 193]; in the super sink region $\alpha_{ssnk} = 0.1$. The coupling between that two layesr that gives rise to the antiferromagnetic order is defined in Listing 3.

With material parameters defined, we next define the parameters of the charge current excitation. We simulate a current-perpendicular-to-plane geometry, where a charge current passes through a polarizing layer and then interacts with out sample (the polarizing layer is not explicitly defined). Listing 5 shows how the spin transfer torque excitation is set-up. The term "lambda" describes the spacer layer and "epsilonprime" defines the field-like component of the spin transfer torque [111, 152, 156]. The fixed layer is set to provide an out-of-plane spin polarization with charge-to-spin efficiency of 50%, as set by the Pol term.

Finally Listing 6 defines the output quantities of interest and sets the simulation to run for a defined period of time. In this case we are outputting the components of the (spatially averaged) magnetization in the top (region 2) and bottom (region 5) channels and the total energy of the system. These are saved to the output table every 10 ps. A snapshot of the magnetization is saved as a OVF file at the same rate. The simulation is set to run for a total of 20 ns.

```
// Set up RKKY coupling for AFM ordering of the two magnetic layers
// Scale with respective top and bottom layers
RKKY := -1e-3
scale := (RKKY * (sizeZ/Nz)) / (2 * Aex.Average())
ext_ScaleExchange(1,5,scale)
ext_ScaleExchange(2,6,scale)
ext_ScaleExchange(3,7,scale)
ext_ScaleExchange(4,8,scale)
```

Listing 3: Define the parameters of the RKKY coupling used to align the two ferromagnetic layers antiparallel to one another.

```
// Deep notches of 60nm x 30nm
len := Sqrt(1800)*1e-9
k := Cuboid(len,len,4e-9).rotz(45*pi/180).transl(0,50e-9,0)
l := Cuboid(len,len,4e-9).rotz(45*pi/180).transl(0,-50e-9,0)
```

Listing 4: Process for defining the geometry of the notches. This creates a pair of triangular notches that are 60 nm × 30 nm × 4 nm, centered lengthwise and placed at the top and bottom edges of the channel.

A.3 Data Analysis

Mumax^3 saves data to a standard output table and can also output a variety of files. By default these are OVF files, which can then be converted to OMF, PNG, or even numpy compatible files for further post-processing using the provided Mumax^3 converter tool. OVF and OMF files are standard output files of the OOMMF micromagnetics package [194].

It is possible to extract the components of the magnetization from each cell using the OMF output files. The OMF files consist of header lines and then three columns of information after that. Each column contains the value of the magnetization component m_x, m_y, and m_z for a cell. The cells within the simulation are arranged row by row in an order that starts at the $(-x, -y, -z)$ corner of the simulation space and goes to $(+x, -y, -z)$ before incrementing up one row along y (i.e. $(-x, -y + 1, -z) \rightarrow (+x, -y + 1, -z)$). This pattern is done for all cells within the xy plane and then z is incremented, repeating until all cells have been parsed through. This order is visualized for a $4 \times 4 \times 2$ grid in Fig. A.1.

```
// Define spacer layer parameters and current density
lambda = 1
Pol = 0.5
epsilonprime = 0
fixedlayer = vector(0,0,1)
Jc := 1.2e11 // Critical current density: Jcrit ~ 1.10E11 A/m2
J.setregion(1,vector(0,0,Jc)) // Apply to only the top injector
```

Listing 5: Define the parameters of the spin transfer torque used to excite dynamics.

```
// Set up output to save snapshots and run
tableadd(m.region(2))
tableadd(m.region(5))
tableadd(E_total)
autosave(m,10e-12)
tableautosave(10e-12)
run(20e-9)
```

Listing 6: Define the output quantities and run the simulation.

Using this pattern, it is possible to turn the three columns of data stored within a single OMF file into 3-dimensional arrays within Python, as done in Listing 8. Using a nested loop, this Python code extracts the data from the individual OMF files and stores them in arrays for each component of the magnetization. By adding a fourth index to the arrays, it is possible to store the magnetization components for each OMF file, thereby adding a temporal dimension to the arrays. From here, it is possible to compute the spatial or temporal evolution of various quantities, such at the in-plane phase angle, phase gradient, precessional frequency, wavelength, etc.

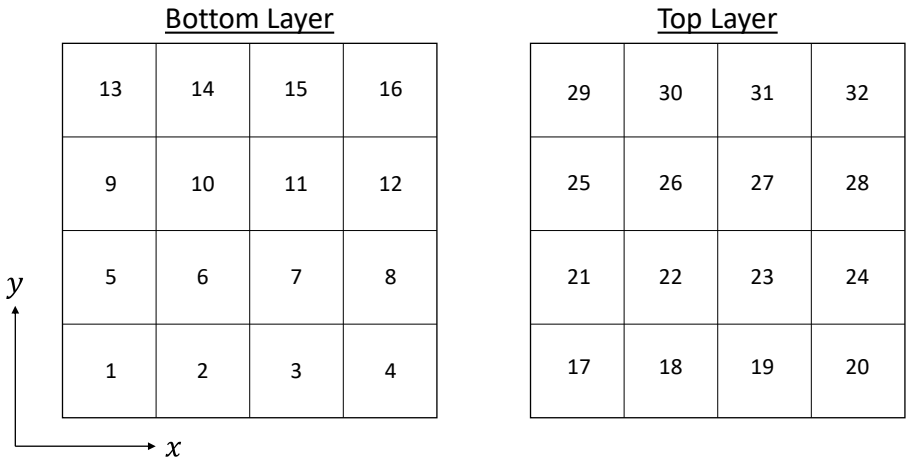


Figure A.1: Visualization of how the data is organized within an OMF file for a $4 \times 4 \times 2$ sample. Each numbered cell will correspond to a row within the OMF file.

```
import numpy as np
import pandas as pd

# Filename to extract data from
filename = 'm000000.omf'

# Define length of arrays to match number of cells
Nx = 800; Ny = 40; Nz = 2

runtime = 20 # Simulation time in nanoseconds
snapshotrate = 10 # Interval of snapshots of m, in picoseconds
numsamples = 1 + (1000*runtime//snapshotrate) # Total number of snapshots

# Empty 3D arrays to hold magnetization components
Mx_array = np.zeroes((Nx,Ny,Nz,numsamples),dtype=float)
My_array = np.zeroes((Nx,Ny,Nz,numsamples),dtype=float)
Mz_array = np.zeroes((Nx,Ny,Nz,numsamples),dtype=float)
```

Listing 7: Variable and array declaration to hold magnetization data extracted from OMF files.

```
# Extract data using the Pandas library
df = pd.read_csv(filename,sep=' ',skiprows=29,skipfooter=2,
                 names=['Mx','My','Mz'],index_col=False,
                 engine='python')
m_array = df.values # Turns above DF into a numpy array
l = 0 # Index for time

# Loop through data and assign to arrays in appropriate order
for k in range(0,Nz):
    for j in range(0,Ny):
        for i in range(0,Nx):
            Mx_array[i,j,k,l] = m_array[i+j*Nx+k*Nx*Ny,0]
            My_array[i,j,k,l] = m_array[i+j*Nx+k*Nx*Ny,1]
            Mz_array[i,j,k,l] = m_array[i+j*Nx+k*Nx*Ny,2]
```

Listing 8: The nested loop within the Python code that extracts data from the OMF files. From here post-processing on the data can be done.